SPACE RESEARCH IN SLOVAKIA

2024 – 2025

SLOVAK ACADEMY OF SCIENCES

COSPAR

SLOVAK NATIONAL COMMITTEE

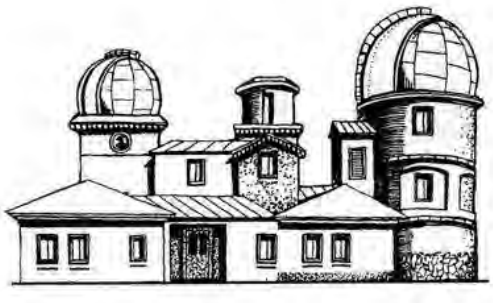

Slovak Central Observatory Hurbanovo

APRIL 2026

Slovak Central Observatory, Hurbanovo, April 2026
Editors: Ivan Dorotovič and Ján Feranec
ISBN: 978-80-89998-49-4

CONTENTS

1. EXPERIMENTS FOR MEASUREMENTS IN SPACE

J. Baláž, I. Strhárský, N. Werner

Experiment SERENA/PICAM on board of ESA-BepiColombo mission

The Institute of Experimental Physics, Slovak Academy of Sciences, contributed to ESA-BepiColombo mission to planet Mercury in the frame of scientific-technical cooperation with Space Technology Ireland (STIL) and Institute for Space Research of Austrian Academy of Sciences (IWF-ÖAW). The Institute contributed to design and construction of the ion mass spectrometer PICAM (*Planetary Ion CAMera*).

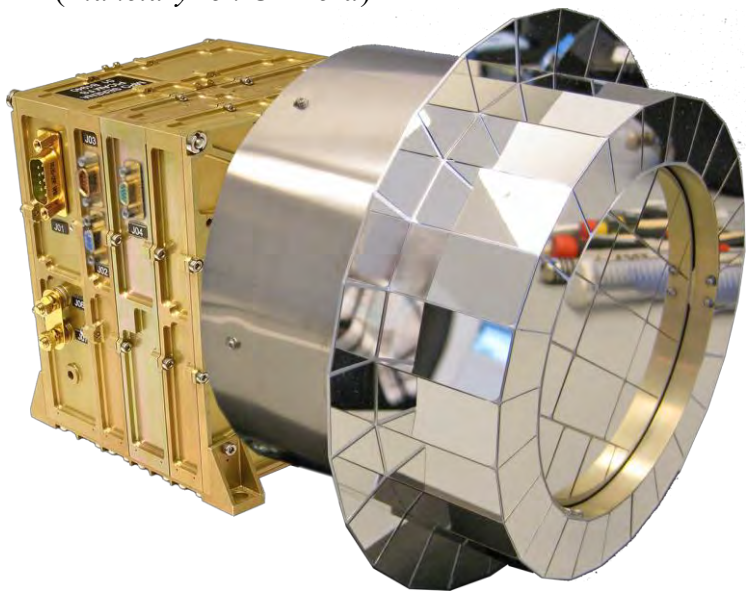

Figure 1.1. *SERENA / PICAM device.*

PICAM is a part of a complex space science suite SERENA (*Search for Exospheric Refilling and Emitted Natural Abundances*) for particle detection at environment of the planet Mercury. Since the launch of the mission on 20th October 2018, BepiColombo spacecraft passed one flyby of Earth, two flybys of Venus and six flybys of Mercury. With the advantage of a clear field of view, PICAM is able to operate effectively during cruise flight as well as during planetary flybys. Contrary to the planned insertion of the spacecraft into orbit in December 2025, the insertion was postponed to November 2026 due to insufficient power of the ion thrusters of the MTM transfer module. The problem with the lack of power was localized in the MTM distribution unit. To date (February 2026), the science suite SERENA operates nominally and contributed to valuable science results from the Mercury environment as well as to the interplanetary and heliospheric physics, e.g. [1], [2], [3].

The detailed descriptions of the SERENA devices and science objectives are provided in [4] and [5].

Experiment PEP/JDC for ESA-JUICE mission

Experiment PEP (*Particle Environment Package*) will provide comprehensive detection and analysis of the plasma and particle environment in the system of planet Jupiter and its

Galilean moons Europa, Callisto and Ganymede. PEP will measure density and flux of positive and negative ions, electrons, exospheric neutral gas, thermal plasma and energetic neutral atoms in the energy range from <0.001 eV to >1 MeV with full angular coverage. The PEP suite includes six sensors (JDC, JEI, JoEE, NIM, JNA and JENI) that were developed at several EU and US institutions led by Swedish Institute of Space Physics (IRF). Based on invitation from IRF, the Institute of Experimental Physics contributed to development and construction of anti-coincidence particle detection module (ACM) for JDC sensor (*Jovian plasma Dynamics and Composition*) of the PEP suite. The purpose of the ACM is to provide improvement of the plasma particles detection efficiency on the background of penetrating electron radiation from the Jovian radiation belts. The ACM module consists from silicon solid state detector (SSD) located in the axis of the JDC sensor and from processing electronic module that provides amplification, charge/voltage conversion, shaping and discrimination of the SSD signal.

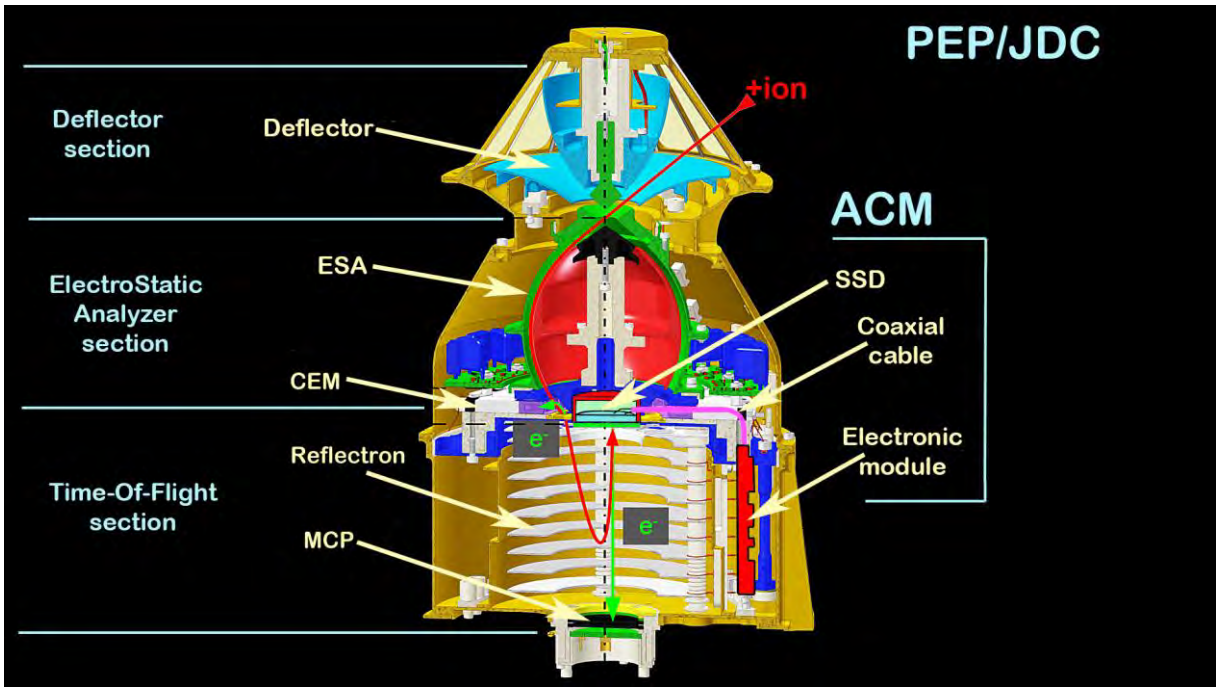

Figure 1.2. *PEP/JDC sensor with position of the ACM module.*

The JUICE mission was successfully launched on 14th April 2023 on board of the Ariane-5 launcher from European spaceport Kourou in French Guiana. During the Moon-Earth flyby in August 2024 the data recorded from the ACM clearly showed transition of the JUICE spacecraft through the Van Allen electron radiation belt. The ACM data were recorded with the constant discrimination threshold of 90 keV and demonstrated very good compliance with the RADEM radiation detector of the JUICE spacecraft. During the next Earth flyby that is scheduled for September 2026, it is foreseen to operate the ACM over all energy thresholds to better characterize its performance in a real space radiation environment.

The arrival to Jupiter and insertion to the orbit is planned for June 2031. The JUICE mission including the PEP science suite description is provided in [6].

The participation of IEP SAS to JUICE mission was supported by ESA-PECS (*Plan for European Cooperating States*) project named: *"Slovak contribution to ESA-JUICE mission: Development of Anti-Coincidence Module ACM for Particle Environment Package PEP"*.

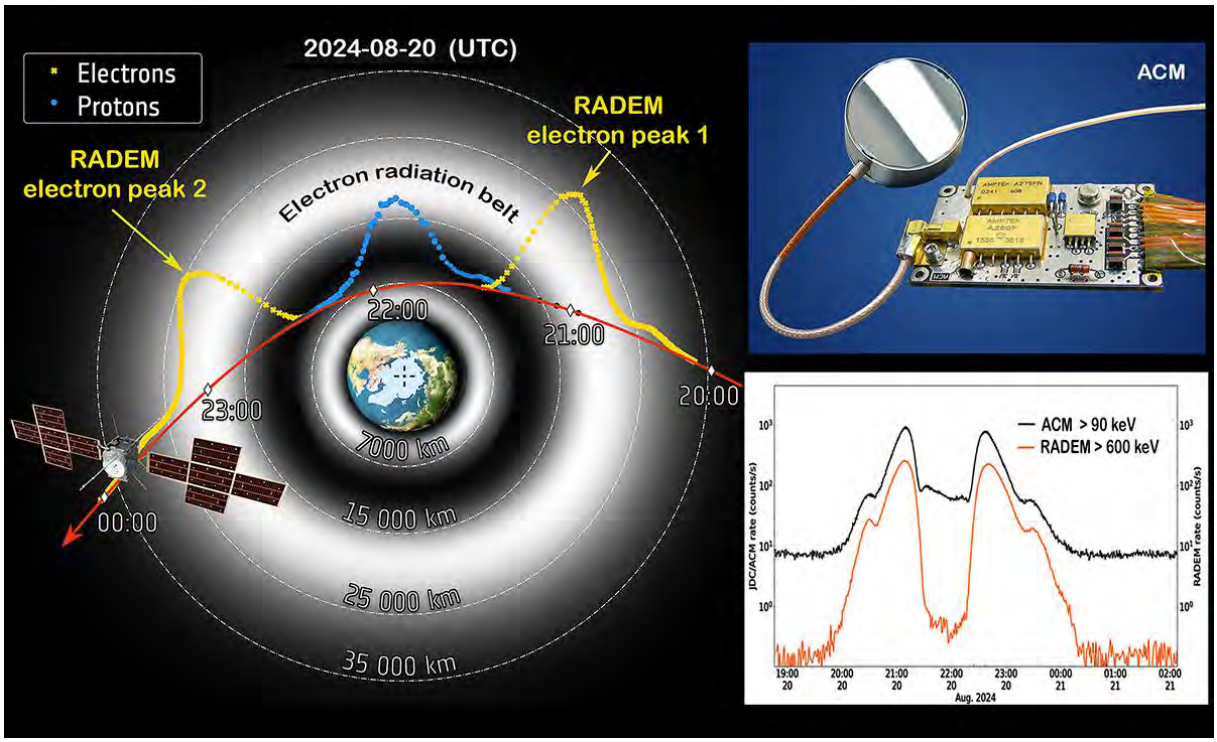

Figure 1.3. *JUICE spacecraft passage through the Van Allen electron radiation belt and data recorded by the ACM and RADEM devices.*

Experiments GRBAlpha nad GRBBeta

GRBAlpha was a 1U CubeSat, which launched in March 2021 to a sun-synchronous orbit at an altitude of 550 km and naturally deorbited in June 2025. The mission was international and included the Hungarian Konkoly Observatory, Czech Masaryk University, Japanese Hiroshima University, and the Technical University in Košice, Slovakia. The main objective of the mission was to perform an in-orbit demonstration of a novel gamma-ray burst detector developed for CubeSats [7]. This instrument, which detected gamma-rays in the range of 30-900 keV, consisted of a 56 cm^2 5 mm thin CsI(Tl) scintillator read-out on one side by a set of 8 SiPM detectors, multi-pixel photon counters by Hamamatsu. The mission allowed the characterisation of the degradation of SiPMs due to particles encountered in polar orbit [8].

The scientific motivation was to detect gamma-ray bursts (GRBs) and other high-energy transient events and serve as a pathfinder for a larger constellation of nanosatellites that could localise these events via triangulation. The satellite and its detector operated until the end of the mission, and over its lifetime, GRBAlpha detected 227 transients confirmed by larger GRB missions [9]. 124 of them are identified as gamma-ray bursts, including "brightest-of-all-times" GRB 221009a, where the smaller size of our detectors allowed us to determine the peak emission of the burst when other monitors were saturated [10].

The follow-up mission, called GRBBeta, was launched in July 2024 on the maiden flight of Ariane 6. The international mission includes the Hungarian Konkoly Observatory, the Czech Masaryk University, the Canadian Dunlap Institute of Astronomy and Astrophysics at the University of Toronto, the Japanese Hiroshima University, and the Technical University in Košice, Slovakia.

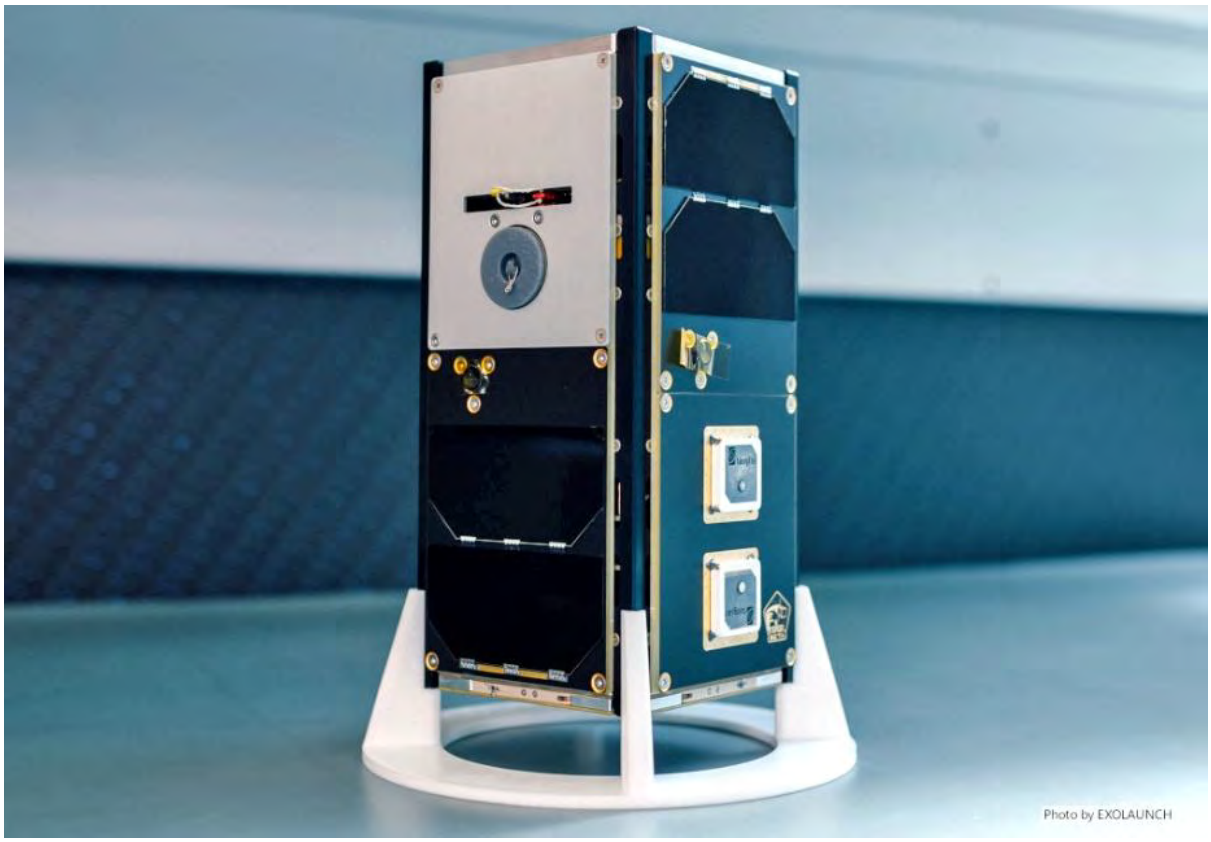

Figure 1.4. *GRBBeta CubeSat.*

Next to the gamma-ray burst detector, which is practically identical to the one on *GRBAlpha*, the mission carries a prototype CMOS-based UV camera to demonstrate technology for future UV space telescope missions. As of February 2026, GRBBeta operates nominally, its GRB detector has detected around 20 transients [9] and the UV camera continues taking images.

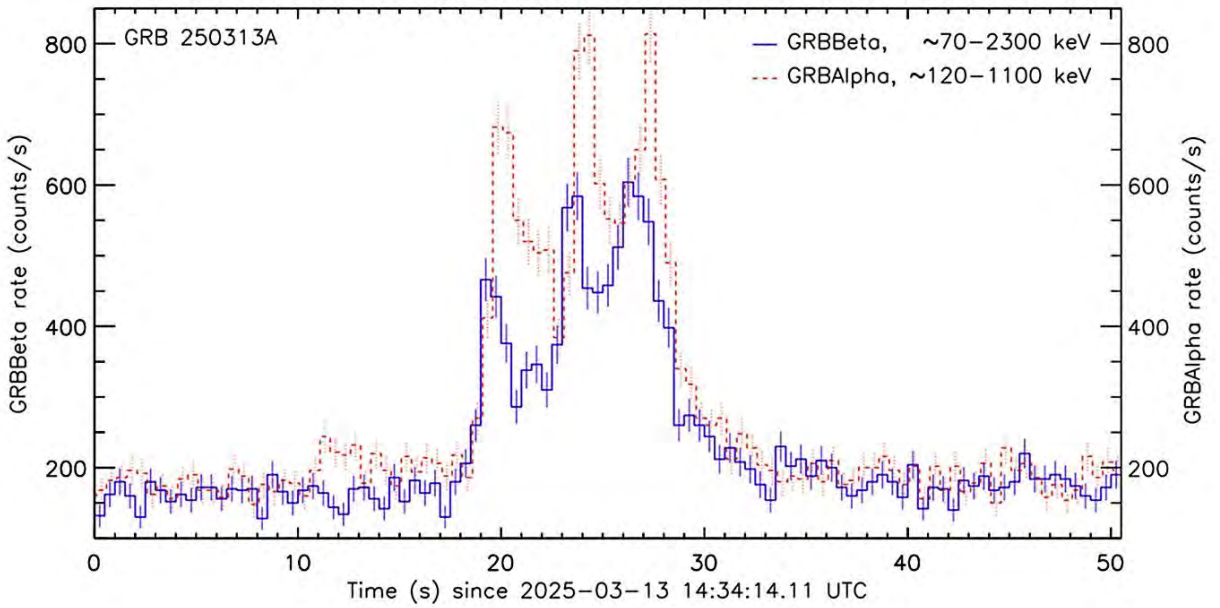

Figure 1.5. *The light curve of the gamma-ray burst GRB 250313A detected by both GRBAlpha and GRBBeta CubeSats ([9]).*

References:

[1] SÁNCHEZ-CANO, B. – HADID, L.Z. – AIZAWA, S. *et al.* BepiColombo cruise science: overview of the mission contribution to heliophysics. *Earth Planets Space* **77**, 114 (2025). https://doi.org/10.1186/s40623-025-02256-z

[2] STUMPO, M. – LAURENZA, M. – BENELLA, S., *et al*. In-depth Analysis of the 2022 March 28 ^{3}He-rich Solar Energetic Particle Event. *The Astrophysical Journal, Volume 987, Number 1 (2025)*. https://doi.org/10.3847/1538-4357/add5f1

[3] ORSINI, S. – MILILLO, A. – LICHTENEGGER, H., *et al*. Inner southern magnetosphere observation of Mercury via SERENA ion sensors in BepiColombo mission. Nature Communications 13, 7390 (2022). https://doi.org/10.1038/s41467-022-34988-x

[4] ORSINI, S. – LIVI, S. A. *et al.* SERENA: A suite of four instruments (ELENA, STROFIO, PICAM and MIPA) on board BepiColombo-MPO for particle detection in the Hermean environment. Planetary and Space Science 58 (2010), pp 166-181, https://doi.org/10.1016/j.pss.2008.09.012

[5] ORSINI, S. – LIVI, S. A. – LICHTENEGGER, H., *et al.* (2021). SERENA: Particle instrument suite for determining the Sun-Mercury interaction from BepiColombo. Space Science Reviews, 217(1), 11. https://doi.org/10.1007/s11214-020-00787-3

[6] The JUICE Science Working Team. JUpiter ICy moons Explorer, Exploring the emergence of habitable worlds around gas giants. https://sci.esa.int/documents/33960/35865/1567260128466-JUICE_Red_Book_i1.0.pdf

[7] PÁL A. – OHNO, M. – MESZÁROS, L. – WERNER, N. – ŘÍPA J. – CSÁK, B. – DAFČÍKOVÁ, M. – FRAIT, M. – FUKAZAWA, Y. – HANÁK, P. – HUDEC, J. – HUSÁRIKOVÁ, N. – KAPUŠ, J. – KASAL, M. – KOLÁŘ, M. – KOLEDA, M. – LÁSZLÓ, R. – LIPOVSKÝ, P. – MIZUNO, T. – MÜNZ, F. – NAKAZAWA, K. – REZENOV, M. – ŠMELKO, M. – TAKAHASHI, H. – TOPINKA, M. – URBANEC, T. – BREUER, J.-P. – BOZÓKI, T. – DÁLYA, G. – ENOTO, T. – FREI, Z. – FRISS, G. – GALGÓCZI, G. – HROCH, F. – ICHINOHE, Y. – KAPÁS, K. – KISS, L. L. – MATAKE, H. – ODAKA, H. – POON, H. – POVALAČ, A. – TAKÁTSY, J. – TORIGOE, K. – UCHIDA, N. – UCHIDA, Y.: 2023, Astronomy & Astrophysics, 677, id.A40: "GRBAlpha: the smallest astrophysical space observatory - Part 1: Detector design, system description and satellite operations"

[8] ŘÍPA J. – DAFČÍKOVÁ, M. – KOSÍK, P. – MÜNZ, F. – OHNO, M. – GALGÓCZI, G. – WERNER, N. – PÁL A. – MESZÁROS, L. – CSÁK, B. – FUKAZAWA, Y. – TAKAHASHI, H. – MIZUNO, T. – NAKAZAWA, K. – ODAKA, H. – ICHINOHE, Y. – KAPUŠ, J. – HUDEC, J. – FRAIT, M. – REZENOV, M. – DÁNIEL, V. – SVOBODA, P. – DUDÁŠ, J. – SABOL, M. – LÁSZLÓ, R. – KOLEDA, M. – DURÍŠKOVÁ, M. – SZAKSZONOVÁ, L. – KOLÁŘ, M. – HUSÁRIKOVÁ, N. – BREUER, J.-P. – HROCH, F. – VÍTEK, T. – VEŘTÁT, I. – URBANEC, T. – POVALAČ, A. – KASAL, M. – HANÁK, P. – ŠMELKO, M. – TOPINKA, M. – CHANG, H.-K. – LIU, T.-Ch. – LIN, Ch.-H. – HU, Ch.-P. – TSAO, Ch.-Ch.: 2026, Nuclear Inst. and Methods in Physics Research, A, Volume 1076, id.170513: "Characterization of more than three years of in-orbit radiation damage of SiPMs on GRBAlpha and VZLUSAT-2 CubeSats"

[9] ŘÍPA J. – DAFČÍKOVÁ, M. – PÁL A. – WERNER, N. – OHNO, M. – MESZÁROS, L. – MÜNZ, F. – CSÁK, B. – GALGÓCZI, G. – HUSÁRIKOVÁ, N. – VÍTEK, T., – KOSÍK, P. – DURÍŠKOVÁ, M. – KOLÁŘ, M. – SZAKSZONOVÁ, L. – PAZDERKA, M. – HROCH, F. – TOPINKA, M. – FUKAZAWA, Y. – TAKAHASHI, H. – MIZUNO, T. – YOKOTA, M. – BREUER, J.-P. – NAKAZAWA, K. – ODAKA, H. – ICHINOHE, Y. – HANÁK, P. – ŠMELKO, M. – VEŘTÁT, I. – URBANEC, T. – POVALAČ, A. – KASAL, M. – KAPUŠ, J. – HUDEC, J. – FRAIT, M. – REZENOV, M. – DÁNIEL, V. – SVOBODA, P. – DUDÁŠ, J. – SABOL, M. – LÁSZLÓ, R. – KOLEDA, M. – CHANG, H.-K. – LIU, T.-Ch. – LIN, Ch.-H. – HU, Ch.-P. – TSAO, Ch.-Ch. – SEN, K. – WU, Ch-E. – TOHUVAVOHU, A. – SIVANANDAM, S., and BARNET, M.: 2026, [arXiv:2601.16609] To appear in Multifrequency Behaviour of High Energy Cosmic Sources - XV (MULTIF2025), 9-14 June, 2025, Mondello, Palermo, Italy, accepted in Proceedings of Science, PoS(MULTIF2025)057: “GRBAlpha, VZLUSAT-2 and GRBBeta – GRB observations with CubeSats”

[10] ŘÍPA J. – TAKAHASHI, H. – FUKAZAWA, Y. – WERNER, N. – MÜNZ, F. – PÁL A. – OHNO, M. – DAFČÍKOVÁ, M. – MESZÁROS, L. – CSÁK, B. – HUSÁRIKOVÁ, N. – KOLÁŘ, M. – GALGÓCZI, G. – BREUER, J.-P. – HROCH, F. – HUDEC, J. – KAPUŠ, J. – FRAIT, M. – REZENOV, M. – LÁSZLÓ, R. – KOLEDA, M. – ŠMELKO, M. – HANÁK, P. – LIPOVSKÝ, P. – URBANEC, T. – KASAL, M. – POVALAČ, A. – UCHIDA, Y. – POON, H. – MATAKE, H. – NAKAZAWA, K. – UCHIDA, N. – BOZÓKI, T. – DÁLYA, G. – ENOTO, T. – FREI, Z. – FRISS, G. – ICHINOHE, Y. – KAPÁS, K. – KISS, L. L. – MIZUNO, T. – ODAKA, H. – TAKATSY, J. – TOPINKA, M. – TORIGOE, K.: 2023, Astronomy & Astrophysics, 677, id.L2: “The peak-flux of GRB 221009A measured with GRBAlpha”

2. SPACE PHYSICS, GEOPHYSICS AND ASTRONOMY

P. Bobík, I. Dorotovič, A. Galád, L. Kornoš, S. Kostárová, J. Kubančák, R. Langer, Š. Mackovjak, P. Matlovič, R. Nagy, M. Revallo, J. Rybák, I. Strhárský, J. Šilha, J. Tóth

The Department of Space Physics at the ***Institute of Experimental Physics, Slovak Academy of Sciences (IEP SAS)*** in Košice (http://space.saske.sk) continues its multi-platform research in space physics through ground-based observations, satellite measurements, and the development of original numerical and data-driven models.

High Altitude Cosmic Rays Observatory of IEP SAS at Lomnický štít (LMKS), as a key member of the NMDB (Neutron Monitor Database) project, provides data with 1-minute resolution for a broad range of users. The continuous dataset [1] with 42 years of measurement was published and is available for the scientific community together with a discussion of the most interesting detected events. In cooperation with the Czech Academy of Sciences (CZ), new results were obtained ([2],[3]) and new instruments (i.e., SND neutron detector) were installed at the observatory to measure the effects of accelerated particles from space in thunderstorm clouds. Thanks to the development and operation of the network SEVAN, the first parallel winter continental gamma-ray glows in Central Europe were observed during a rare winter thunderstorm [4]. The application of NM data for the calculation of heliocentric potential, which is needed for the estimation of radiation doses for aircrew, is performed within the newly started project ESA ESADOS (ESA Support for Aircrew Dosimetry Services). IEP SAS also cooperates with other high-altitude observatories in Europe via the VAO (Virtual Alpine Observatory) consortium.

In the field of cosmic ray modelling, research at IEP SAS is mainly focused on the modulation and distribution of cosmic rays in the heliosphere and on the motion of cosmic rays in Earth's magnetosphere. The SDE method for cosmic rays modulation in the heliosphere statistical error and solution uniqueness was presented by [5]. In [6] the authors evaluated how various machine learning techniques approximate the temporal evolution of the AMS-02 daily proton flux from 2011 to 2019. The study focuses on the feasibility and effectiveness of machine learning approaches compared to the traditional force field model in approximating cosmic ray proton spectra. The machine learning methods are very accurate and significantly improve the force field approximation. The activities have also been devoted to studying the relationship between cosmic rays and cloud formation.

The study of geomagnetic storms prediction by the ML approach started at IEP SAS more than two decades ago. The current computational capabilities, SW frameworks, and actual datasets allow us to provide these predictions in much higher precision. In the study [7], it was developed a unique approach for the prediction of the Dst index 4 and 8 hours ahead by combining L1 point optical coronagraph images and in-situ solar wind parameters. The results are based on the study and data preparation similar to those that will be produced by the ESA Vigil mission ([8]). Such a dataset can also be used for other data-driven models and thus contribute to improving the reliability and timeliness of predictions from the ESA Vigil mission data streams. The study was conducted in collaboration with the Technical University of Košice (SK), Politecnico di Torino (IT), and the European Space Agency. The research on the thermosphere-ionosphere also utilizes the ML approach. It is performed in cooperation with Boston University (US) by using their network of all-sky imagers. The automated approach has been developed to effectively process the acquired data ([9]).

IEP SAS participates in the international KM3Net project - the next-generation neutrino telescope. This year, the collaboration published a significant discovery of the highest-energy neutrino ever observed.

References:

[1] KISVÁRDAI, I. – ŠTEMPEL, F. – RANDUŠKA, L. – MACKOVJAK, Š. – LANGER, R. – STRHÁRSKÝ, I. & Kubančák, J.: 2025, Analysis of 42 years of cosmic ray measurements by the neutron monitor at Lomnický štít observatory, *Earth and Space Science*, 12, e2024EA003656. https://doi.org/10.1029/2024EA003656

[2] KÁKONA, M. – KÁKONA, J. – DVOŘÁK, R. – AMBROŽOVÁ, I. – VELYCHKO, O. – LUŽOVÁ, M. – ŠLEGL, J. – SOMMER, M. – HANOUSEK, V. – LANGER, R. – ŠTEFÁNIK, S., & Ploc, O.: 2025, Measurements with Angular Sensitive Electric Field Mill in Thunderstorms, *Journal of Physics: Conference Series*, 2985, 012014. https://doi.org/10.1088/1742-6596/2985/1/012014

[3] PIERRARD, V. – BOLSÉE, D. – WINANT, A. – AL-QAAOD, A. – KRASNIQI, F. – PÉTERS DE BONHOME, M. – BOTEK, E. – Van LAEKEN, L. – SAPUNDJIEV, D. – VAN MALDEREN, R. – MANGOLD, A. – AMBROŽOVÁ, I. – SOMMER, M. – ŠLEGL, J. – GERONIKOLOU, S. – GEORGAKILAS, A. – DORN, A. – RAPP, B. – ŠOLC, J. – MAREK, L. – OANCEA, C. – DOPPLER, L. – LANGER, R. – WALSH, S. – SABIA, M. – VUOLO, M. – PAPAYANNIS, A. – GRANJA, C.: 2025, BIOSPHERE measurement campaign from January 2024 to March 2024 and in May 2024: Effects of the solar events on the radiation belts, UV radiation and ozone in the atmosphere, *AIMS Geosciences*, 11(1): 117. https://doi.org/10.3934/geosci.2025007

[4] ŠLEGL, J. – SOKOL, Z. – PEŠICE, P. – Langer, R. – STRHÁRSKÝ, I. – POPOVÁ, J. – KÁKONA, M. – AMBROŽOVÁ, I. and PLOC, O.: 2025, First reported detection of a winter continental gamma-ray glow in Europe, Atmos. Chem. Phys., 25, 8443–8454, https://doi.org/10.5194/acp-25-8443-2025

[5] MYKHAILENO, V. – NGUYEN, M. – SOLANIK, M. – GENČI, J. – KOLESNYK, Y. – BOBÍK, P.: 2024, SDE method for cosmic rays modulation in the heliosphere statistical error and solution uniqueness, Computer Physics Communications, 296, 109026, https://doi.org/10.1016/j.cpc.2023.109026

[6] NGUYEN, M. – BOBÍK, P. & GENČI, J.: 2025, Approximation of daily AMS-02 spectra with machine learning methods. *Journal of Geophysical Research: Machine Learning and Computation*, 2, e2025JH000676. https://doi.org/10.1029/2025JH000676

[7] MAJIRSKÝ, A. – MACKOVJAK, Š. – KOSTÁROVÁ, S. – MAGLI. E. – BUTKA, P., and LONGEPE, N.: 2025, Combining Solar Imagery and In Situ Data for Prediction of Geomagnetic Storms, *The Astrophysical Journal*, 995, 50, https://doi.org/10.3847/1538-4357/ae1cc7

[8] MAJIRSKÝ, A. – MACKOVJAK, Š. – KOSTÁROVÁ, S., & AMRICH, S.: 2025a, Extreme space weather events of the past 30 years: Preparation for data from mission Vigil, *Earth and Space Science*, 12, e2024EA003937. https://doi.org/10.1029/2024EA003937

[9] MACKOVJAK, Š. – MARTINIS, C. – WROTEN, J. – BAUMGARDNER, J., & MENDILLO, M.: 2025, Synergy of Traditional Techniques and Convolutional Neural Networks for Classification of Cloudless Conditions by All-Sky Imagers, *Publications of the Astronomical Society of the Pacific*, 137, 045004. https://doi.org/10.1088/1538-3873/adca59

The ***Faculty of Mathematics, Physics and Informatics, Comenius University, Bratislava*** was involved in the following directions of research as listed below.

Meteor observations and analyses by AMOS global meteor network

The AMOS (All-sky Meteor Orbit System) global meteor network continued its systematic monitoring of meteor activity using combined all-sky trajectory stations and AMOS-Spec spectrographs. This instrumentation enables a comprehensive study of small Solar System bodies in terms of their dynamics, physical properties, and emission spectra, with the long-term goal of constraining the compositional distribution of meteoroids from different Solar System source regions. The global network currently consists of 17 all-sky systems and 19 spectrographs deployed across Slovakia, the Canary Islands, Chile, Hawaii, Australia, South Africa, and Arizona, providing one of the widest coordinated datasets for meteor spectroscopy currently available (Fig. 2.1). Hardware and software used within the AMOS network have been developed and constructed at the Faculty of Mathematics, Physics and Informatics of Comenius University in Bratislava [1].

During 2024-2025, we continued to expand the AMOS spectral program through new international collaborations. New spectrographs were installed in cooperation with the Desert Fireball Network in Australia and with the Vatican Observatory at Mount Hopkins Observatory in Arizona, further improving the geographical coverage of the network and the probability of obtaining multi-station meteors with simultaneously measured trajectories and spectra. These observations are being used in an ongoing survey aimed at the spectral classification of meteoroids and at linking their measured atmospheric behaviour with plausible meteoritic analogues.

A major basis for this work is our recently concluded analysis of laboratory meteorite ablation experiments. Numerous studies utilizing various instrumentation methods for studying the emission, ablation and fragmentation for meteoroids were published in a special issue summarized in [2]. The experiments connected controlled plasma wind tunnel experiments with meteor observations and provided the largest reference dataset of laboratory meteor analogues obtained to date. The experiments included a broad range of meteorite types and were designed specifically to improve the interpretation of meteor spectra and the identification of incoming planetary material. The results were notably used to characterize the diagnostic spectral properties of ablated meteorite samples and showed that ordinary chondrites, carbonaceous chondrites, achondrites, stony-irons, and irons can be distinguished using relative line intensities and other spectral indicators measured under meteor-like conditions [3]. These results now serve as an important reference for the interpretation of AMOS meteor spectra and for improved compositional diagnostics of meteoroids observed in the atmosphere.

In our most recent work [4], we identified the first achondritic meteoroids in AMOS meteor data, including candidate aubrite- and eucrite-like impactors, based on their spectra, dynamics, and physical properties (Fig. 2.2). This study demonstrates that meteor spectroscopy can directly reveal rare differentiated bodies among present-day meteoroid populations and opens a new pathway for tracing the real distribution of planetary materials entering the Earth's atmosphere.

We have demonstrated the capability of the updated All-Sky Meteor Orbit System (AMOS and AMOS-Spec) to provide photometric calibration of the unique Alberta fireball [5] and in comparison to other meteor systems like FRIPON, GMN, Desert Fireball Network in paper [6], where meteor trajectory and heliocentric orbits from the same source of data were compared in very good agreement. In 2022 AMOS systems were deployed in Arizona desert and onboard of dedicated jet plane to cover Tau Hercluids meteor shower activity on May 31 due to comet 73P/Schwassmann-Wachmann 3 break-up in 1995. Special meteor cluster of Tau Herculids was

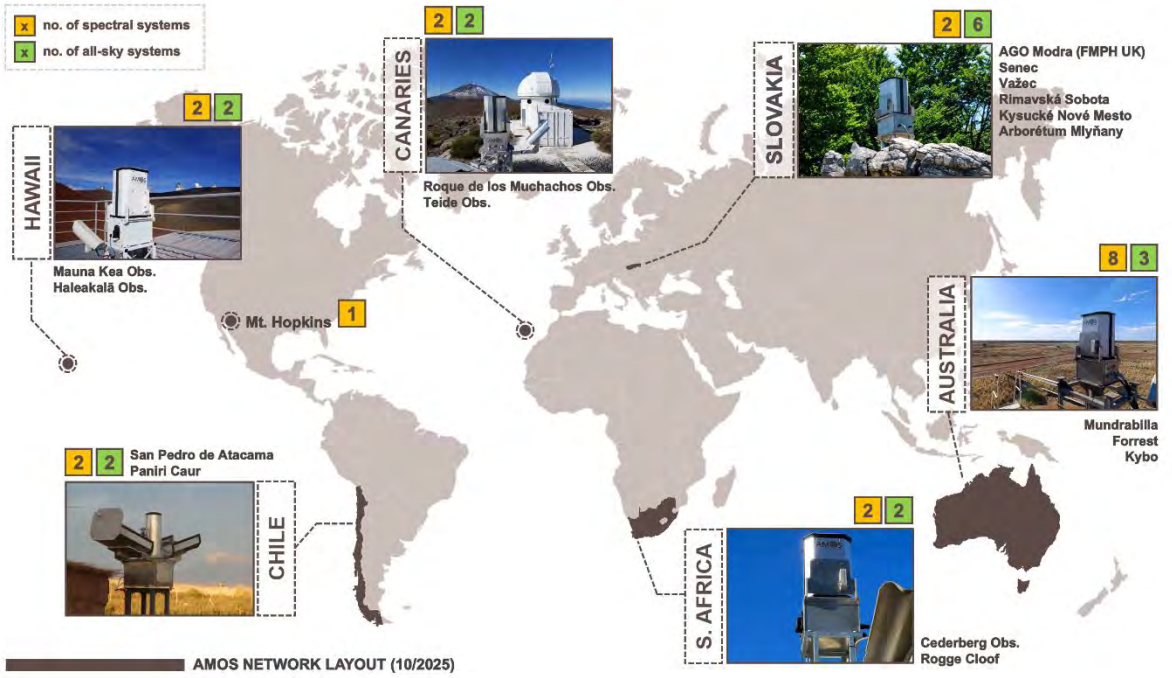

***Figure 2.1**. AMOS global meteor network operated by Comenius University in Bratislava with 17 all-sky AMOS systems and 19 AMOS-Spec systems. Red crosses are active location of AMOS stations covering all-sky for meteor trajectory and spectroscopic observations.*

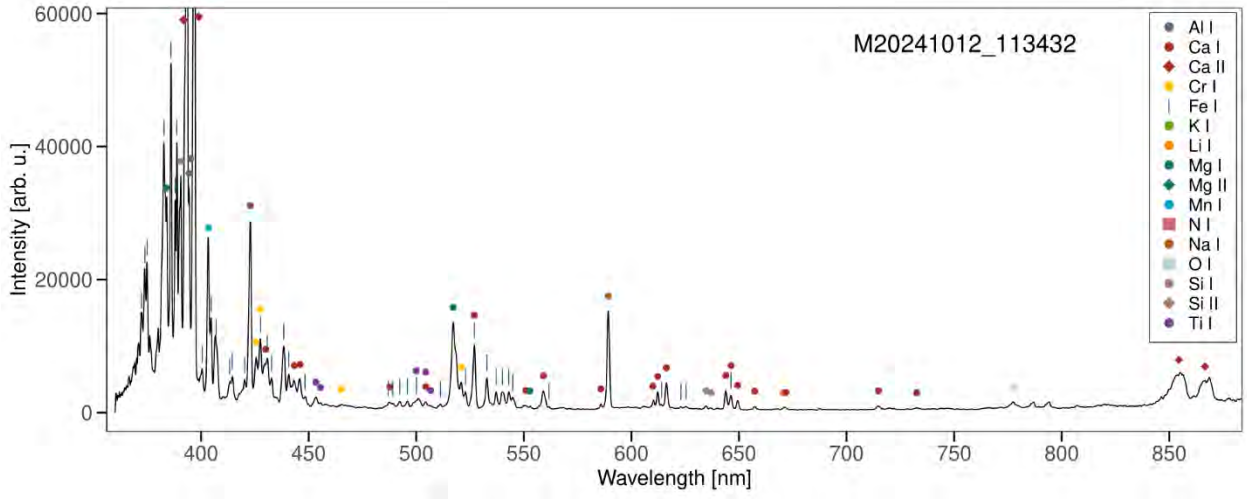

***Figure 2.2**. Emission spectrum of an eucrite meteoroid captured by the AMOS station in Manuakea, Hawaii. The composition was identified using spectral analysis. The surviving meteorite fell into the Pacific Ocean.*

recorded from the plane at the altitude of 40 000 ft and later analyzed as one of the most numerous clusters of 52 members fragmented from original meteoroid just few days before atmospheric entry by thermal stress [7].

Automated Detection and Dynamical Evolution of Disc Galaxies

The department of astronomy and astrophysics at FMPI CU is actively engaged in investigating the structure of the Milky Way galaxy and other galaxies as well. In collaboration with domestic and international institutes (e.g. University College London, UK, Technical University in Košice), we have made significant advances in both observational techniques and theoretical understanding of galactic dynamics.

In collaboration with the Mullard Space Science Laboratory at University College London and the Technical University in Košice, we have developed an innovative **deep learning algorithm designed to automatically identify and extract edge-on and highly inclined galaxies** from astronomical images [8]. This work represents a significant advancement in processing the vast amounts of data from modern astronomical surveys.

Using a sample of 16,000 edge-on spiral galaxies from the Galaxy Zoo database and the Sloan Digital Sky Survey (SDSS), we trained the YOLOv5 algorithm for detection purposes and the SCSS-Net neural network for segmentation. Our algorithm achieved impressive performance metrics with precision of 0.80 and recall of 0.94, demonstrating its reliability in identifying edge-on galaxies.

The algorithm was successfully applied to the full SDSS DR17 sample, detecting approximately 12,000 high-confidence edge-on galaxies (confidence ≥ 0.7). This automated detection and segmentation capability is particularly valuable for future large-scale surveys such as Euclid, the Roman Space Telescope, and the Large Synoptic Survey Telescope (LSST), where the volume of data will necessitate machine learning approaches. The extracted galaxy cutouts and compiled catalogue provide a valuable resource for future studies of galactic structure, particularly for investigating warped disks in edge-on galaxies.

We have conducted a comprehensive theoretical study comparing **stellar radial migration (churning) in Milky Way-like galaxies under two different gravitational frameworks**: the classical Newtonian approach with dark matter and Modified Newtonian Dynamics (MOND) [9]. This work provides important insights into how different gravitational theories predict distinct dynamical evolution of galactic disks. Through numerical simulations integrating 2×10^6 stellar orbits over 6 Gyr in a static rotating galactic potential, we investigated the effects of non-axisymmetric structures - specifically the galactic bar and spiral arms - on stellar migration. We explored various configurations of spiral arm parameters, including different spiral pattern speeds (Ω_{sp} = 19, 25, and 31 km s^{-1} kpc^{-1}) and amplitudes (A_{sp} = 850, 1000, and 1200 km^2 s^{-2} kpc^{-1}).

Our results reveal striking differences between the two gravitational regimes, see Fig. 2.3. Radial migration is significantly more pronounced in MOND compared to the dark matter approach. Specifically, we observe up to five times as many stars with a maximum change in the guiding radius exceeding 1.5 kpc during the 2 – 6 Gyr time interval in the MOND regime compared to the dark matter configuration. This enhancement occurs because non-axisymmetric galactic components represent a larger fraction of the total gravitational influence in MOND, leading to stronger resonance effects.

Analysis of the frequency phase space revealed that the most prominent resonances driving radial migration are the co-rotation resonance with the spiral arms (m = p = 1), the outer Lindblad resonance with both the galactic bar and spiral arms, and the co-rotation resonance

(m = 2, p = 1) with the superposition of the galactic bar and spiral arms. These resonances create distinct patterns of stellar redistribution across the galactic disk.

We also found that increasing the amplitude of the spiral structure amplifies radial migration effects in both regimes, while increasing the spiral pattern speed reduces the relative difference between dark matter and MOND predictions. The co-rotation resonance with spiral arms proved especially important in enhancing migration effects, significantly impacting the spatial distribution of stellar components and the structural evolution of the galaxy.

These findings have important implications for understanding the dynamical history of the Milky Way and for constraining gravitational theories through observations of stellar kinematics and chemical abundances in our Galaxy. The distinct predictions for radial migration in the two frameworks provide potential observational tests that could help distinguish between dark matter and alternative gravity theories.

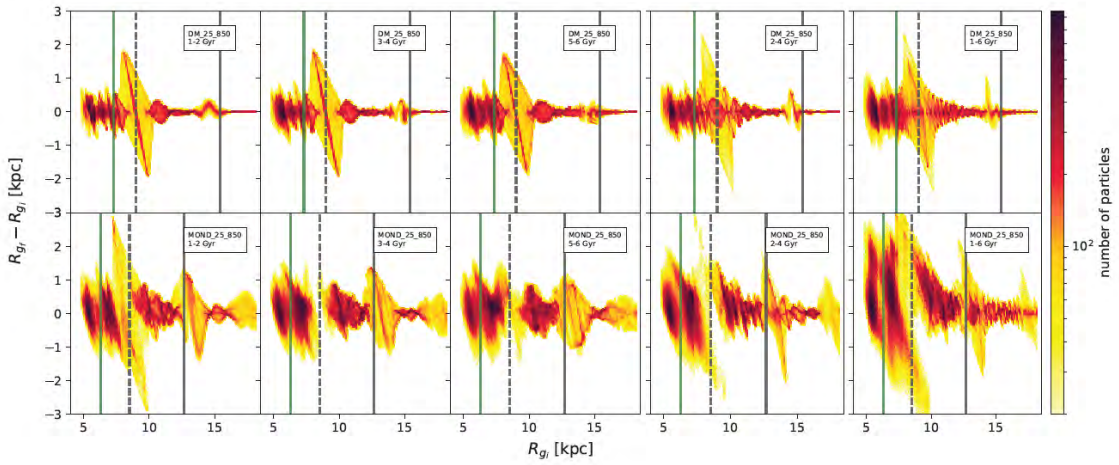

Figure 2.3. *Distribution of changes in the guiding radius, Rgf − Rgi , (radial migration) as a function of Rgi (initial guiding radius) for different time intervals during the 6 Gyr integration. Vertical lines represent the theoretical values of resonances: green lines for resonances produced by the galactic bar and grey lines for resonances caused by the spiral arms. In both cases, the solid lines represent OLRs and the dashed line the m = p = 1 co-rotation resonance.*

Space debris photometry and spectroscopy research

The Faculty of Mathematics, Physics and Informatics of Comenius University in Bratislava, Slovakia (FMPI) operates its own 0.7-m Newtonian telescope (AGO70) dedicated to the space surveillance tracking and research, with an emphasis on space debris [8]. The observation planning focuses on objects on geosynchronous (GEO) and eccentric (GTO and Molniya) orbits. Light curve acquisition programme conducted over the years 2017-2022 led to buildup of an extensive space debris catalogue containing almost 2’000 photometric measurements of 759 individual objects. The light curve catalogue of space debris is freely available to the scientific community (www.sdlcd.space-debris.sk) and can be used for further scientific applications such as support of active debris removal missions, rotation axis determination, BVRI photometry, object's shape and albedo estimation, etc.

Each material has reflective signatures, which enable us to distinguish different features on the object’s surface and provide information about the object’s attitude or utilize the categorization into the population or material groups. In the work [10] authors proposed new physics-based taxonomy characterization of reflectance spectra of ASOs. To establish this method, authors used 107 reflectance spectra published in the available literature (Fig. 2.4, left).

Authors defined regions of interest in the wavelength range with commonly present absorptions. Authors considered the range of visible spectrum wavelengths to analyze between 370 nm and 900 nm. Three major materials have been distinguished - absorbing materials (A) which exhibit significant absorption features, materials with moderate sign of absorption due to some absorbing elements added to their mixture (M) and non-absorbing materials showing no signs of absorption (N). Additionally, identified have been three wavelength ranges containing absorption bands – (u) for ultraviolet, (b) for blue and (v) for visible. A special case of aluminum absorption feature at 850 nm has been assigned as well as category (a). Eventually, all these properties could be organized into a 3 × 3 matrix where absorbing, mixtures and non-absorbing materials (A, M and N) are given in rows and the specific wavelength ranges (u, b, v, -a) are defined in columns. In total, 9 taxonomy categories were defined – Au, Ab, Av, Mu, Mb, Mb-a, N, Nb, N-a. Authors successfully applied new defined spectra classification method to spectra collected by [11] as well as on newly collected spectra using the 80-cm telescope operated by the Astronomical Institute of the University of Bern (Fig. 2.4, right).

In work [12] authors focus on darkening and reddening effects induced by space weathering and aging on single geostationary satellites and satellites with similar platforms.

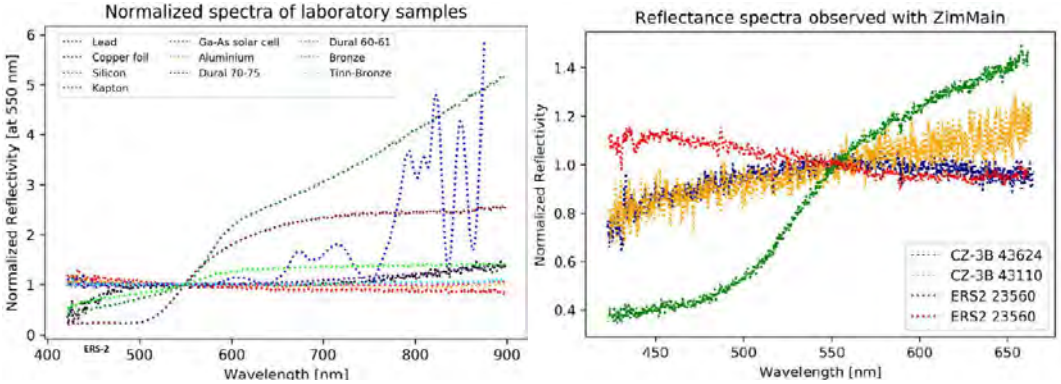

Figure 2.4. *Left: Reflectance spectra of aerospace material samples measured in a laboratory with absolute reflectivity relative to silicon and normalized to 550 nm. Right: Spectra of two upper stage rockets CZ-RB with Norad 43624 and 43110, and two spectra of the ERS-2 satellite (23560) observed at different attitudes, glinting phase (red) and non-glinting (green). Source: [10].*

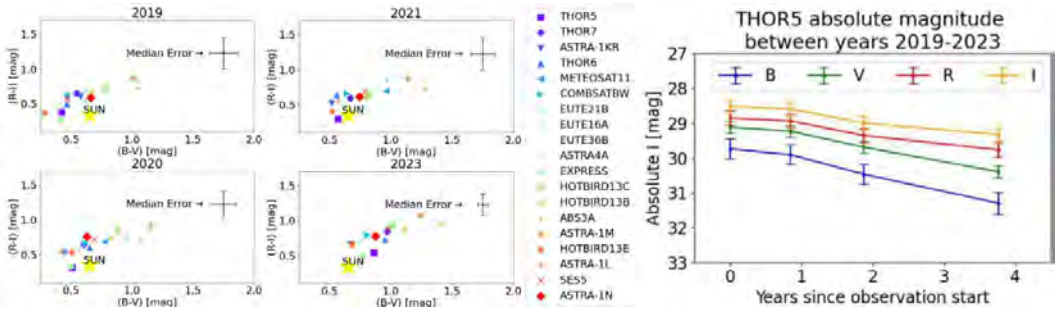

Figure 2.5. *Left: Changes of the annual color indices of all targets observed during the campaign. The median error represents the uncertainties in B-V and R-I estimated as median of all plotted data. The median error is introduced for better readability of the figure. Right: Absolute magnitude evolution in all measured passbands over the 4 years during the campaign. Source: [11].*

The published results contain BVRI color index measurements and their year-to-year variation rates. In total, 18 active GEO satellites have been monitored over the course of four years (Figure 2.5, left). Authors observed change in related color indices, as well as in absolute brightness. The average change values measured were 0.1 mag/year in *B-V* index, 0.5 mag/year in *R-I* index and 0.21 mag/year in *B-I* index. Observations showed that all objects undergo reflectivity losses in each passband and that absolute magnitude losses are not equal in different passbands.

Photometric observations and research of asteroids using a 60-cm telescope at AGO Modra Observatory

Part of our archive photometric data contributed to the spin and shape analysis of a few near-Earth asteroids [13, 14] and to the orbital characteristics of distant satellites of some main-belt binary asteroids [15]. After 13 years, our photometric survey of V-type asteroids ended in 2025. The results are planned to be mentioned in the next report.

References:

[1] TÓTH, J. – KORNOŠ, L. – ĎURIŠ, F. – MATLOVIČ, P. – ZIGO, P. – KALMANČOK, D. – PAULECH, T. – ŠIMON, J. – BALÁŽ, M. – VÖRÖS, T. – PAPRSKÁROVÁ, M. – PAZDEROVÁ, V. – SOLČÁNI, J. – SCHICHMAN, M. – VARGA, P.: AMOS global meteor network: instrumentation, procedures, accuracy validation and results, *Icarus* (2026) in press

[2] TÓTH, J. – MATLOVIČ, P. – LOEHLE, S. – VAUBAILLON, J. – PISARČÍKOVÁ, A. – LEISER, D. – GRIGAT, F. – EBERHART, M. et al. Overview of the MetSpec project-Artificial meteors in ground testing, *Icarus*, 407, 115791 (2024) https://doi.org/10.1016/j.icarus.2023.115791

[3] MATLOVIČ, P. – PISARČÍKOVÁ, A. – PAZDEROVÁ, V. – LOEHLE, S. – TÓTH, J. – FERRIÈRE, L. – ČERMÁK, P. - LEISER, D. - VAUBAILLON, J. – RAVICHANDRAN, R., Spectral properties of ablating meteorite samples for improved meteoroid composition diagnostics, *Astronomy & Astrophysics,* 689, A323 (2024) https://doi.org/10.1051/0004-6361/202450913

[4] MATLOVIČ, P. – PISARČÍKOVÁ, A. – PAZDEROVÁ, V. – VÖRÖS, T. – HLOBIK, F. – DEVILLEPOIX, H. A. R. – BOROVIČKA, J. – PAPRSKÁROVÁ, M. – DEAM, S. – TÓTH, J. – KORNOŠ, L. – PAULECH, T. – ZIGO, P., Achondrites in meteor data: Spectra, dynamics, and physical properties of candidate aubrite and eucrite impactors, *Astronomy & Astrophysics*, 706, A247 (2026) https://doi.org/10.1051/0004-6361/202558248

[5] VIDA, D. – BROWN, P. G. – DEVILLEPOIX, H. A. R. – WIEGERT, P. – MOSER, D. E. – MATLOVIČ, P. – HERD, Ch. D. K. – HILL, P. J. A. – SANSOM, E. K. – TOWNER, M. C. – TÓTH, J. – COOKE, W. J. – HLADIUK, D. W., Direct measurement of decimetre-sized rocky material in the Oort cloud, *Nature Astronomy*, vol. 7, pp. 318–329 (2023), https://doi.org/10.1038/s41550-022-01844-3

[6] SHOBER, P. M. – VAUBAILLON, J. – ANGHEL, S. - DEVILLEPOIX, H. A. R. – HLOBIK, F. – MATLOVIČ, P. – TÓTH, J. – VIDA, D. – SANSOM, E. K. – JANSEN – STURGEON, T. – COLAS, F. – MALGOYRE, A. – KORNOŠ, L. ĎURIŠ, F – PAZDEROVÁ, V. – BOULEY, S. – ZANDA, B. – VERNAZZA, P., Comparing the data-reduction pipelines of FRIPON, DFN, WMPL, and AMOS: Case study of the Geminids, *Astronomy & Astrophysics*, 705, A65 (2026), https://doi.org/10.1051/0004-6361/202554364

[7] KOTEN, P. – ČAPEK, D. – TÓTH, J. – SHRNBENÝ, L. – BOROVIČKA, J. - VAUBAILLON, J. – ZANDER, F. – BUTTSWORTH, D. – LOEHLE, S., A very young τ-Herculid meteor cluster observed during a 2022 shower outburst, *Astronomy & Astrophysics,* 695, A189 (2025). https://doi.org/10.1051/0004-6361/202553764

[8] CHROBÁKOV, Ž. – KREČKOVÁ, V. – NAGY, R. – GAZDOVÁ, J., & Butka, P., Deep Learning-based Detection and Segmentation of Edge-on and Highly Inclined Galaxies. Publications of the Astronomical Society of the Pacific, 137, 034101 (2025). https://doi.org/10.1088/1538-3873/adbcd6

[9] NAGY, R. – JÁNK, F. – ŠTURC, M. – JURČÍK, M., & PUCHÁ, E., Comparing radial migration in dark matter and MOND regimes. Astronomy & Astrophysics, 693, A216 (2025). https://doi.org/10.1051/0004-6361/202452112

[10] ŽILKOVÁ, D. – ŠILHA, J. – VOJTEK, P. – RODRIGUEZ-VILLAMIZAR, J. – DE LEON, J. – MATLOVIČ, P. – SABOLOVÁ, K. – SCHILDKNECHT, T. – TÓTH, J. – LÁSZLÓ, R.: Connecting laboratory and spectroscopic observations of aerospace materials to characterize the reflectivity of artificial space objects and debris in LEO regimes. *Acta Astronautica* 236, 479–486, (2025), https://doi.org/10.1016/j.actaastro.2025.07.003

[11] ŽILKOVÁ, D. – ŠILHA, J. – MATLOVIČ, P. – TÓTH, J., Space debris spectroscopy: Specular reflections at LEO regime, *Advances in Space Research,* 71, 8, (2023), 3249-3261, https://doi.org/10.1016/j.asr.2022.12.001

[12] ZIGO, M. – ŠILHA, J. – SABOLOVÁ, K. – HROBÁR, T.: Investigation of the space weathering rate of the geostationary satellites' surface materials using BVRI photometry. *Advances in Space Research* 75(10), 7365–7376, (2025), https://doi.org/10.1016/j.asr.2025.02.048

[13] ĎURECH J. – VOKROUHLICKÝ, D. PRAVEC, P. – KRUGLY, Yu. – POLISHOOK, D. – HANUŠ, J. – MARCHIS, F. – ROŽEK, A. – SNODGRASS, C. – ALEGRE, L. – DONCHEY, Z. – EHGAMBERDIEV, Sh. A. – FATKA, P. – GAFTONYUK, N. M. – GALÁD, A. – HORNOCH, K. – INASARIDZE, R. Ya. – KHALOUEI, E. – KUČÁKOVÁ, H. – KUŠNIRÁK, P. – OEY, J. – PRAY, D. P. – SERGEEV, A. – SLYUSAREV, I., Secular change in the spin states of asteroids due to radiation and gravitation torques. New detections and updates of the YORP effect, Astronomy & Astrophysics 682, A93 (2024), doi: 10.1051/0004-6361/202348350.

[14] FATKA, P. – PRAVEC, P. – SCHEIRICH, P. – KUŠNIRÁK, P. – HORNOCH, K. – KUČÁKOVÁ, H. – ERGASHEV, K. E. – SOUZA DE JOODE, M., BURKHONOV, O. A., EHGAMBERDIEV, Sh. A. – GALÁD, A. – VILÁGI, J. – REDDY, V. – DYVIG, R. – RIES, J. G., SNODGRASS, C. – DONALDSON, A. – PEIXINHO, N. – KHALOUEI, E., Spins and shapes of 11 near-Earth asteroids observed within the NEOROCKS project, Astronomy & Astrophysics 695, A139 (2025), doi: 10.1051/0004-6361/202450027.

[15] MINKER, K. – CARRY, B. – VACHIER, F. – SCHEIRICH, P. – PRAVEC, P. – MÜLLER, T. – MOÓR, A. – ARCIDIACONO, C. – CONRAD, A. – VEILLET, C. – JACOBSON, S. A. – MARSSET, M. – MERLINE, W. J. – TAMBLYN, P. – BROWN, M. E. – PRAY, D. – MONTAIGUT, R. – LEROY, A. – GILLIER, C. – KUŠNIRÁK, P. – HORNOCH, K. – HUSÁRIK, M. – BENISHEK, V. – COONEY, W. – GROSS, J. – TERRELL, D. – JEHIN, E. – VILÁGI, J. – GAJDOŠ, Š., CHIORNY, V. – CHRISTMANN, B. – BRINDFIELD, J. – DUMAS, C. – ENKE, B. L. – DURDA, D. D. – CHRISTOU, J. C., GRUNDY, W. M. – CLOSE, L. M. – PORTER, S. B., Orbits of very distant asteroid satellites, Astronomy & Astrophysics 698, A13 (2025), doi: 10.1051/0004-6361/202451124.

At **the *Earth Science Institute of the Slovak Academy of Sciences in Bratislava and Hurbanovo***, research on space weather modeling and forecasting was conducted, alongside ground-based geomagnetic field measurements.

In May 2024, an extremely intense magnetic storm occurred, the strongest observed in the past 20 years. This exceptional event remained at the forefront of interest among space weather experts in 2025. It was intensively discussed at scientific forums and was also the subject of special issues of professional journals. The May 2024 magnetic storm was analyzed in [1] from the perspective of auroral activity, with particular emphasis on the auroral electrojet (AE) index and its modifications. An adjusted AE index was proposed, designed to capture the intensification of auroral currents taking into account the equatorward shift of the auroral oval to mid-latitudes (Figs. 2.6 and 2.7). The results of the study were published in the journal *Advances in Space Research* as part of the special issue "The Powerful Solar-Terrestrial and Space Weather Event in May 2024 – Observations, Data and Preliminary Analysis." The results were also presented in the poster session at the ESWW 2025 conference in Sweden [2].

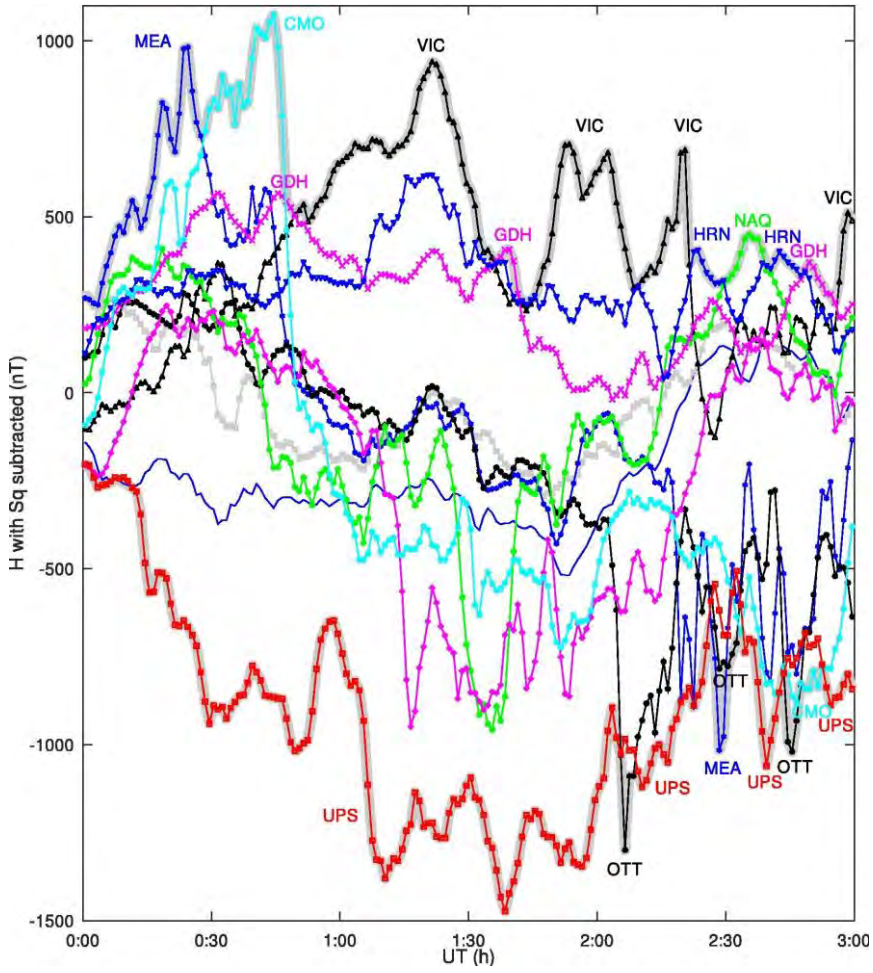

Figure 2.6. *Variations of the horizontal geomagnetic field intensity (H) at selected observatories within the auroral oval on 11 May 2024 between 00:00 and 03:00 UT. Quiet daily variations have been subtracted from the data. The upper and lower thick grey lines represent the adjusted AU^a and AL^a indices, respectively. The IAGA codes indicate the observatories contributing to the index extrema. (From [1].)*

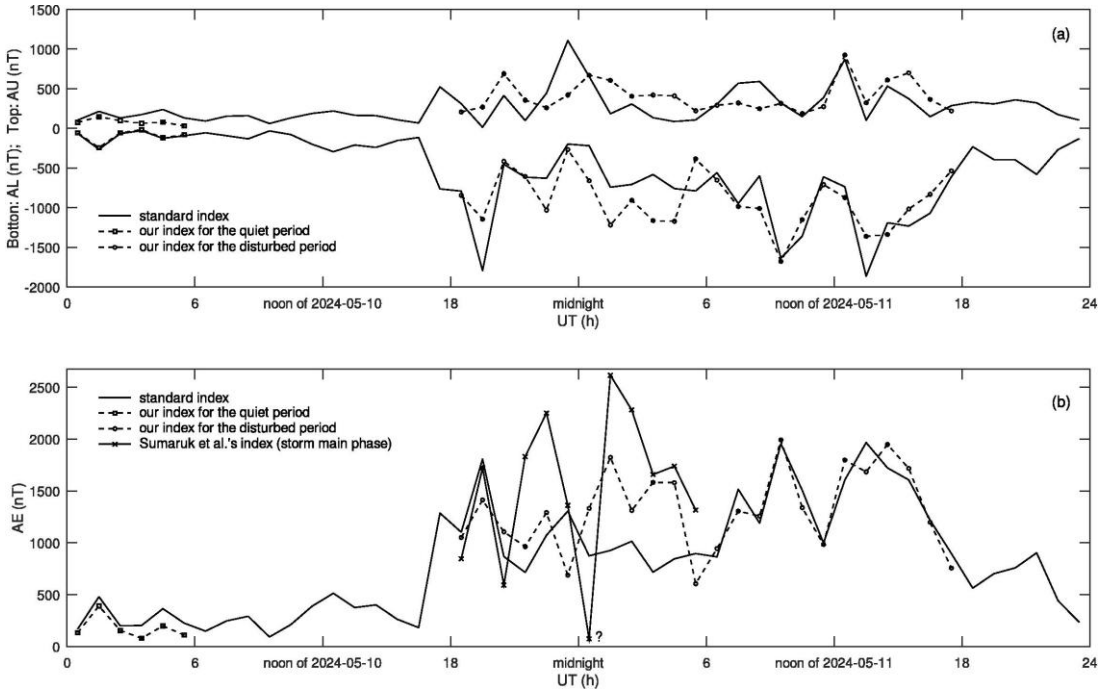

Figure 2.7. *Hourly means of the AU and AL indices (top panel, a) and the AE index (bottom panel, b). Solid lines without added symbols represent the standard AE index. Dashed lines denote the adjusted AE^a index; periods of high geomagnetic activity (Kp = 8+, 9−, and 9) are marked with circle symbols, while an example of relatively low activity (Kp = 3−) is indicated by square symbols. The solid line with x-symbols in panel (b) show the modified AE^m index calculated using a previously derived empirical model. Question marks indicate suspicious values resulting from limitations of the applied procedure. (From [1].)*

In [3], a systematic overview was presented of the physical mechanisms associated with the extreme geomagnetic storm of May 2024, with emphasis on magnetic storm development and solar wind–magnetosphere interaction. In the classical framework, magnetic storms are primarily associated with the development of the ring current. Their basic characteristics can be described by considering processes in the subsolar region of the magnetosphere and its interaction with the solar wind. Coupling functions derived from satellite and ground-based observations are used to characterize energy transfer across the solar wind–magnetosphere boundary. Modelling approaches take into account the temporal evolution of the interaction as well as nonlinear processes during the recovery phase. Attention is also paid to the turbulent region between the bow shock and the magnetopause and to the solar drivers of geomagnetic disturbances.

Further interest in extreme magnetic storms led to study [4], which investigates changes in magnetic declination recorded at European mid-latitude observatories during the extreme Carrington-type geomagnetic storm of 29 October 2003 (the Halloween storm). Spatial and temporal variations of declination (Figs. 2.8 and 2.9) were analyzed to assess their relationship with intense magnetospheric and ionospheric current systems. The study contributes to a better understanding of the manifestations of severe space weather disturbances in mid-latitude regions.

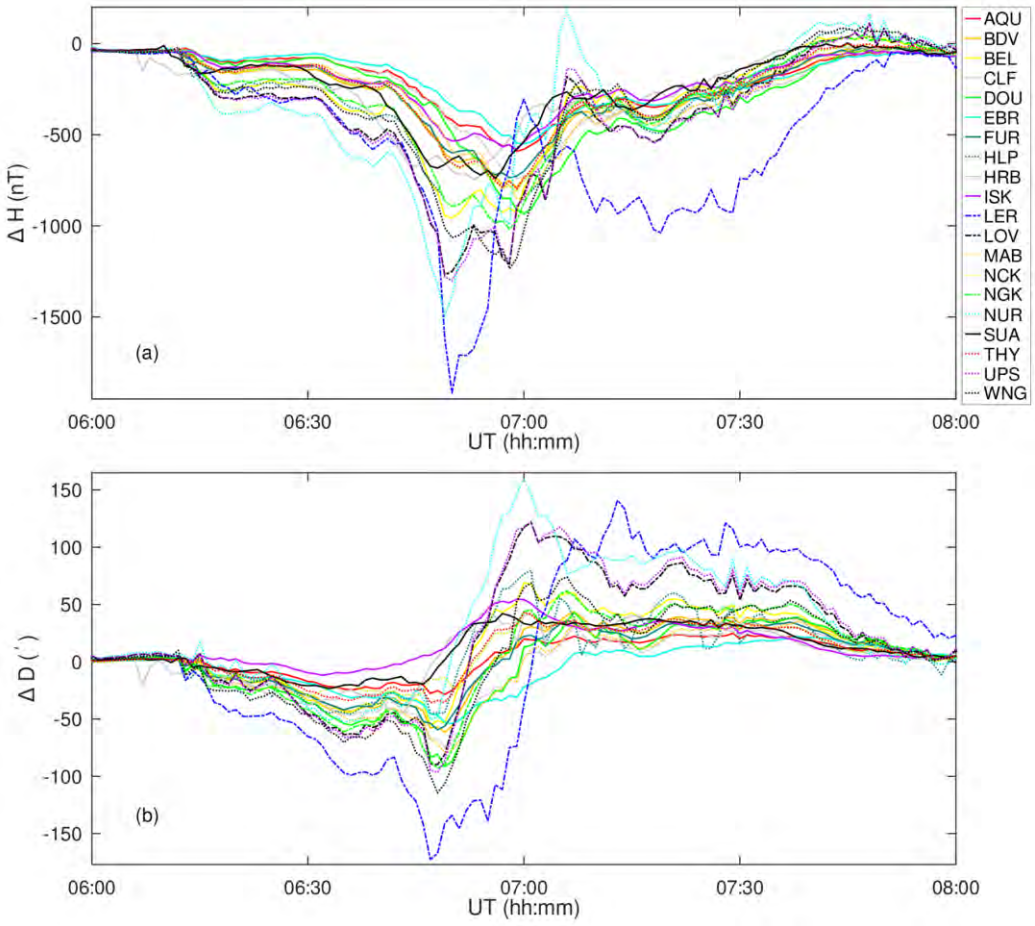

Figure 2.8. *Variations of (a) horizontal geomagnetic field intensity and (b) magnetic declination at European mid-latitude observatories during the 29 October 2003 event. (From [4].)*

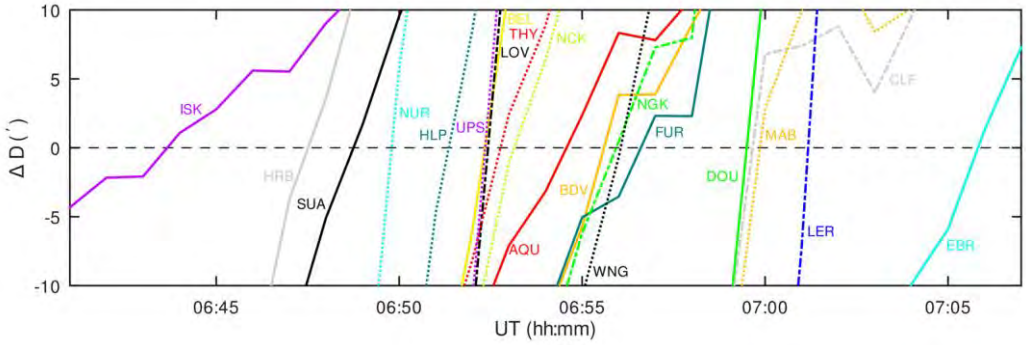

Figure 2.9. *Variations in magnetic declination at European mid-latitude observatories during the passage of the current wedge centre across the stations on 29 October 2003. (From [4].)*

Building on previous research of historical geomagnetic records, unique archival magnetograms from the Ógyalla Observatory were analyzed in [5–8]. In particular, geomagnetic observations from 16 April 1938 reveal the presence of a dayside current wedge during a significant magnetospheric disturbance [8]. Characteristic features in the magnetic data were identified and interpreted in the context of the dayside current wedge system. The

study provides historical evidence of this phenomenon and contributes to a better understanding of magnetospheric dynamics during strong disturbances.

In addition to its theoretical research activities, regular observatory measurements of the geomagnetic field are carried out at the Hurbanovo Geomagnetic Observatory of the Earth Science Institute of the SAS. The observatory is located at a geographic latitude of 47.87° and a geographic longitude of 18.18°. It performs continuous monitoring and recording of the geomagnetic field components. One-minute mean values of the geomagnetic field components are available. K-indices characterizing geomagnetic activity at mid-latitudes are computed on a regular basis. The main equipment includes a digital variometer station TPM (manufactured in Poland in 1996) and a DI-fluxgate magnetometer (Magson), acquired through cooperation with the GeoForschungsZentrum Potsdam and the Volkswagen Foundation. Absolute geomagnetic measurements are performed using a DI-fluxgate magnetometer and a proton precession magnetometer. One-minute magnetovariational data are transmitted via the Internet to the INTERMAGNET centre and are subsequently forwarded to the World Data Centers in Paris, where they are made available to the international geomagnetic and space weather community. The data are also published on CD-ROMs prepared within the INTERMAGNET framework. The observatory is a member of INTERMAGNET, the international network of world first-order magnetic observatories. Information on current geomagnetic activity is also available on the observatory's website (www.geomag.sk).

References:

[1] VALACH, F. – REVALLO, M. – KOČI, E. Auroral-oval activity during the intense magnetic storm of May 2024 - Overcoming the underestimation of the AE index. *Advances in Space Research*, 2025, vol. 76, no. 12, p. 7251-7260. ISSN 0273-1177. https://doi.org/10.1016/j.asr.2025.03.052

[2] KOČI, E. – VALACH, F. – DOROTOVIČ, I. – REVALLO, M. Understanding the May 2024 magnetic storm – interplanetary origins and limitations of standard AE index computation, European Space Weather Week 2025, Umeå, Sweden, 27–31 October 2025, Conference poster abstract link: https://events.spacepole.be/event/222/contributions/4458/

[3] REVALLO, M. – VALACH, F. – HEJDA, P. Interakcia slnečného vetra s magnetosférou a geomagnetická aktivita. In AMBRÓZ, J. et al. Zborník referátov z 27. celoštátneho slnečného seminára, Košice 2024: Slovenská ústredná hvezdáreň Hurbanovo, 2024, s. 12-13. ISBN 978-80-89998-45-6.

[4] VALACH, F. – VÁCZYOVÁ, M. – KOČI, E. Variations in the magnetic declination at mid-latitude European stations during the Carrington-like event on 29 October 2003. *Annales Geophysicae*, 2025, vol. 43, issue 2, pp. 441-445. ISSN 0992-7689. https://doi.org/10.5194/angeo-43-441-2025

[5] VALACH, F. – VÁCZYOVÁ, M. – VÝBERČI, D. – KOČI, E. Regular observations of the geomagnetic field at the Ógyalla observatory (present-day Hurbanovo) near the turn of the 20th century, including magnetic storms accompanied by auroras in March 1894, September 1898, and October 1903. *Contributions to Geophysics and Geodesy*, 2024, vol. 54, no. 1, p. 23-48. ISSN 1335-2806. https://doi.org/10.31577/congeo.2024.54.1.2

[6] KOČI, E. – VALACH, F. The extreme geomagnetic storm on 13–15 May 1921: a study based on hourly means, including observations at Stará Ďala (Hurbanovo). EGU General Assembly 2024, Vienna, Austria, 14–19 Apr 2024, EGU24-16216. https://doi.org/10.5194/egusphere-egu24-16216

[7] VALACH, F. – VÁCZYOVÁ, M. – KOČI, E. Geomagnetické porovnania v Ógyalle, dnešnom Hurbanove, na prelome 19. a 20. storočia. In AMBRÓZ, J. et al. Zborník referátov z 27. celoštátneho slnečného seminára, Košice 2024: Slovenská ústredná hvezdáreň Hurbanovo, 2024, s. 14. ISBN 978-80-89998-45-6.

[8] KOČI, E. – VALACH, F. A sign of the dayside current wedge in geomagnetic observations at Stará Ďala (present-day Hurbanovo) on 16 April 1938. *Contributions to Geophysics and Geodesy*, 2025, vol. 55, no. 3, p. 297-311. ISSN 1335-2806.
https://doi.org/10.31577/congeo.2025.55.3.2

In **the *Slovak Central Observatory* (SCO)** in Hurbanovo (http://www.suh.sk) a number of activities related to space research were performed. We observed sunspots (the Wolf number data were submitted to the SILSO in Brussels, Belgium and to the SONNE Netz in Germany), solar chromosphere and prominences (images are published at https://www.kozmos-online.sk/obs/aktivita/activity.htm). We performed also spectrographic observations of the solar spectrum (variations of selected spectral lines during a solar activity cycle) using a horizontal solar telescope with spectrograph. Using this horizontal solar telescope combined with an image selector and Hα telescope we also mnonitored several solar flares. We registered solar radio bursts using a solar radio spectrometer CALLISTO. The research activities comprise study of the differential rotation of the solar corona.

One researcher from the SCO is the national ISWI (International Space Weather Initiative, http://iswi-secretariat.org) coordinator for the Slovak Republic and since October 2022 he is also delegate of the Slovak Republic in the programme board of ESA for space safety (PB-SSA). He is member of the National Committee of the SCOSTEP and chair and representative to the COSPAR.

We continued to publish at the website of the SCO data on the modified coronal index (MCI) and the modified homogeneous data set (MHDS) of coronal intensities based on satellite EUV measurements as a replacement of ground-based coronagraphic observations at Lomnický Štít. Both the MCI and the MHDS data sets can be used further for studies of the coronal solar activity and its cycle. These data are available at https://www.kozmos-online.sk/slnko.

In the SCO we developed also an alternative software tool to estimate the solar rotational profile based on cross-correlation (CC) method. Analysis of additional SDO data from the years 2024 -2025 is being performed.

E. Koči, researcher from the SCO, is a PhD student at the Geomagnetic Observatory Hurbanovo of the Earth Science Institute of the Slovak Academy of Sciences (Bratislava). His published results are referenced in the previous section.

The SCO organised in the year 2024 in Košice the 27th National Solar Physics Meeting with participation from abroad. The goal of the Meeting was to present new results of solar physics and from the field of the space weather (Sun-Earth connections), to provide overview of present status in selected fields of solar physics, geophysics, meteorology, and climatology. A separate space was devoted to the presentation of research results of undergraduate and PhD students of university and academic departments and also to results of scientific and popularisation activities of Astronomical Observatories in the Slovak Republic and the Czech Republic. Invited talks, short contributions and posters covered the following fields: physical phenomena in the solar atmosphere, solar activity, total solar eclipses, space weather, geoactivity, meteorological events with solar forcing.

The activities of **the *Astronomical Institute of the Slovak Academy of Sciences (AISAS)***, Tatranská Lomnica (*www.astro.sk*), related to COSPAR, were devoted to research in stellar, solar, solar system, and interplanetary physics using different satellite observations, mainly in the UV, XUV and X-ray spectral regions. Stellar data of the Swift, XMM-Newton, TESS, CHEOPS, and Kepler satellites, were used for research of various variable stars [1, 2, 5, 19, 22, 25, 29, 31], stars hosting exoplanets and the exoplanets themselves [3, 6, 9, 11, 15, 18, 20, 21, 23, 24, 26, 30, 32]. Data of the current SDO, SoHO, Hinode, STEREO, and other satellites were used for solar research. In common, these data were used with the simultaneously acquired data by the ground-based solar telescopes and radiospectrometers [4, 10, 12, 13, 33]. Different topics of the solar system bodies have been addressed, in many articles from the laboratory physics side [7, 8, 14, 27, 28] or from close approach satellites to asteroids [16, 17]. Hereby we present some examples of the results obtained by the AISAS staff.

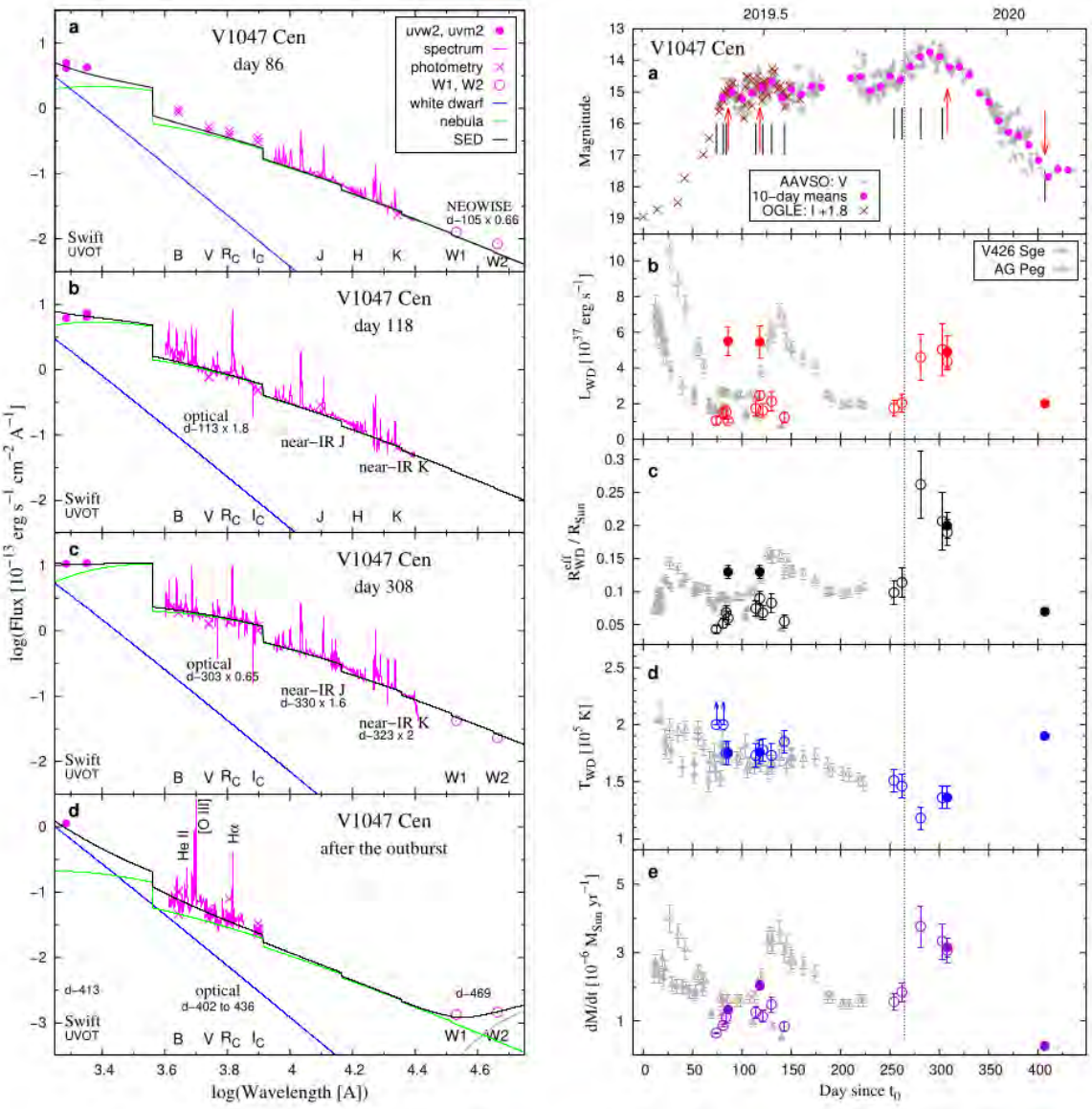

Figure 2.10. *Left: Observed (magenta) and modelled (black line) spectral energy distribution (SED) of V1047 Cen on selected days during its 2019 outburst. Right: Evolution of the V/I light curve (panel (a)) and SED model parameters, luminosity (b), radius (c), temperature (d), and mass-loss rate (e) throughout the 2019 outburst of V1047 Cen. All of these characteristics are typical of a Z And type outburst.*

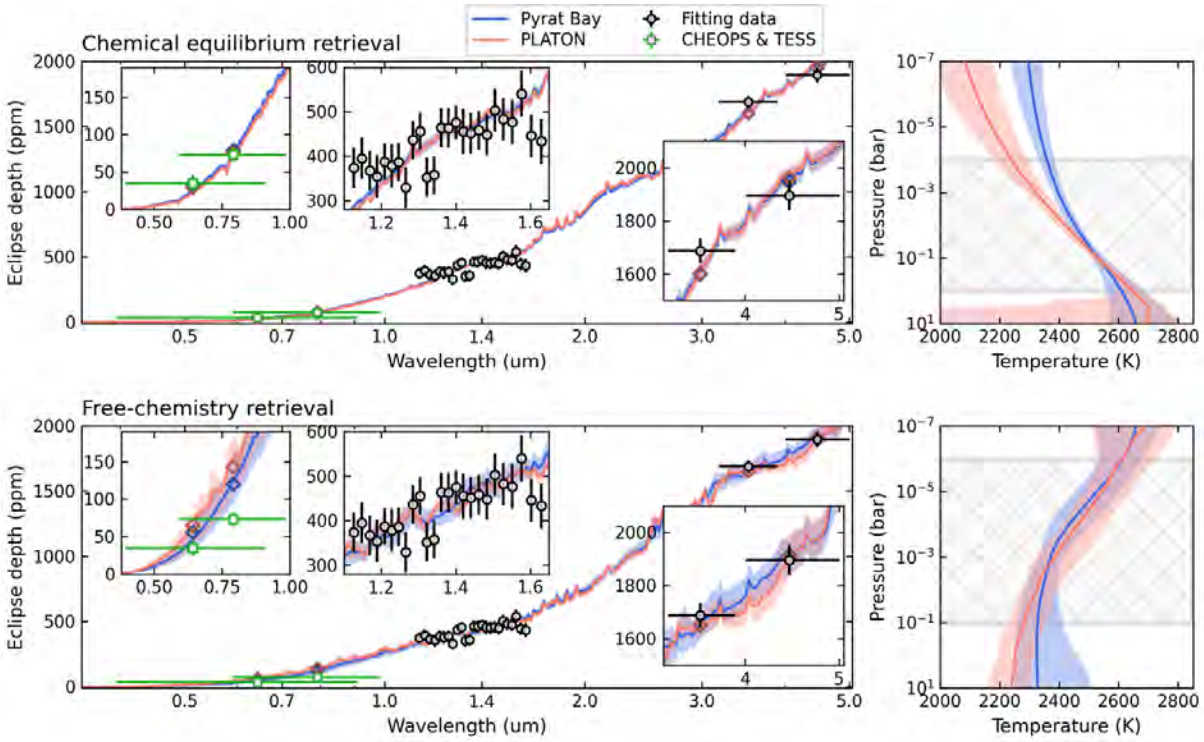

Figure 2.11. *KELT-7b atmospheric retrieval of the infrared occultations. Top left panel: retrievals assuming thermochemical equilibrium with Pyrat Bay (blue) and PLATON (pink). Top right panel: retrieved T-P profiles for each software. The gray hatched area denotes the range of pressures probed by the observations. Bottom panels: same as above, but for the free-chemistry retrievals.*

Observations carried out with the Neil Gehrels Swift Space Observatory (Swift), particularly those using its UltraViolet-Optical Telescope (UVOT) for the ultraviolet photometry (filter UVW1 at 260 nm, UVM2 at 225 nm and UVW2 at 193 nm), were used to model the spectral energy distribution (SED) of the mysterious outburst of the classical nova V1047 Cen that appeared in 2019 and lasted more than 400 days [29]. Having the SED model from the ultraviolet to the near-infrared, allowed us to reveal its true nature as the “Z And” type outburst, which was a surprising result because this type of outbursts has been observed exclusively in symbiotic stars (SySt – interacting binaries with orbital periods of several years). We have shown that after a classical nova explosion, a "Z And" type outburst can occur not only in SySt but also in short-period (hours) cataclysmic variables (CVs), when the accretion-powered system changes to a nuclear-powered system due to the reaction of the donor to the nova explosion. This result thus challenges the typical behavior of CVs after a nova explosion and suggests a new path of stellar evolution that terminates with a Type Ia supernova explosion.

Early theoretical works suggested that ultrahot Jupiters have inverted temperature-pressure (T-P) profiles in the presence of optical absorbers, such as TiO and VO. Recently, an inverted T-P profile of KELT-7b was detected, in agreement with the theoretical predictions. However, the diagnosis of T-P inversions has long been recognized as a model-dependent process. We used the Characterising Exoplanet Satellite (CHEOPS), the Transiting Exoplanet Survey Satellite (TESS), and additional literature data to characterize the atmosphere of KELT-7b [26]. We find that when adopting a thermochemical-equilibrium atmospheric composition, the emission retrievals return a non-inverted T-P profile, in contrast with previous results. When adopting a free-chemistry atmospheric parameterization, the emission retrievals return an

inverted T-P profile. The 3D general circulation model supports a TiO-induced temperature inversion. We can conclude that the choice of a free-chemistry approach or a thermochemical-equilibrium chemistry is the main factor determining the retrieval results. Free-chemistry retrievals generally yield better fits; however, assuming free chemistry risks adopting unphysical scenarios for ultrahot Jupiters, such as KELT-7b.

A quiescent solar prominence was observed using Hα imaging spectroscopy with the Solar Dynamics Doppler Imager (SDDI) attached to the Solar Magnetic Activity Research Telescope (SMART). In contrast to earlier studies that identified 4- and 15-minute oscillations using long-slit, one-dimensional wavelet techniques, the present study extends wavelet analysis to fully three-dimensional data, enabling an exploration of the prominence as a whole. Complementary observations from the Solar Dynamics Observatory/Atmospheric Imaging Assembly (304 and 171 Å), the STEREO-A Extreme Ultraviolet Imager (EUVI; 304 Å), and the Solar Orbiter EIU Imager (304 and 174 Å) provide a multi-view, multi-thermal perspective on wave periodicities across the prominence. The analysis aims to characterize the distribution of oscillatory periods in plasma at different temperatures and viewing angles, thereby assessing wave propagation and variability throughout the prominence body [33]. Time series of Doppler signals from SMART/SDDI Hα data are analyzed together with extreme-ultraviolet intensity variations from the space-based instruments. Oscillatory plasma motions with periods ranging from 3 to 74 minutes are detected. In neutral plasma traced by Hα, strong periodicities at 20, 31, and 53 minutes dominate, whereas oscillations at 13 and 74 minutes are prominent in the 304 Å passband and are mainly concentrated in the central region of the prominence. This multi-instrument, three-dimensional approach advances understanding of how prominence plasma supports and modulates a diverse spectrum of wave modes.

A statistical spectroscopic analysis of coordinated prominence observations in the hydrogen Lyman lines (Lyα–Lyδ) and the Mg II k and h lines obtained on 22 October 2013 by the SoHO/SUMER spectrograph and the Interface Region Imaging Spectrograph (IRIS) is a rare coordinated datasets providing the first combined analysis of these spectral lines in prominences while also assessing, for the first time, the impact of noise on the statistical

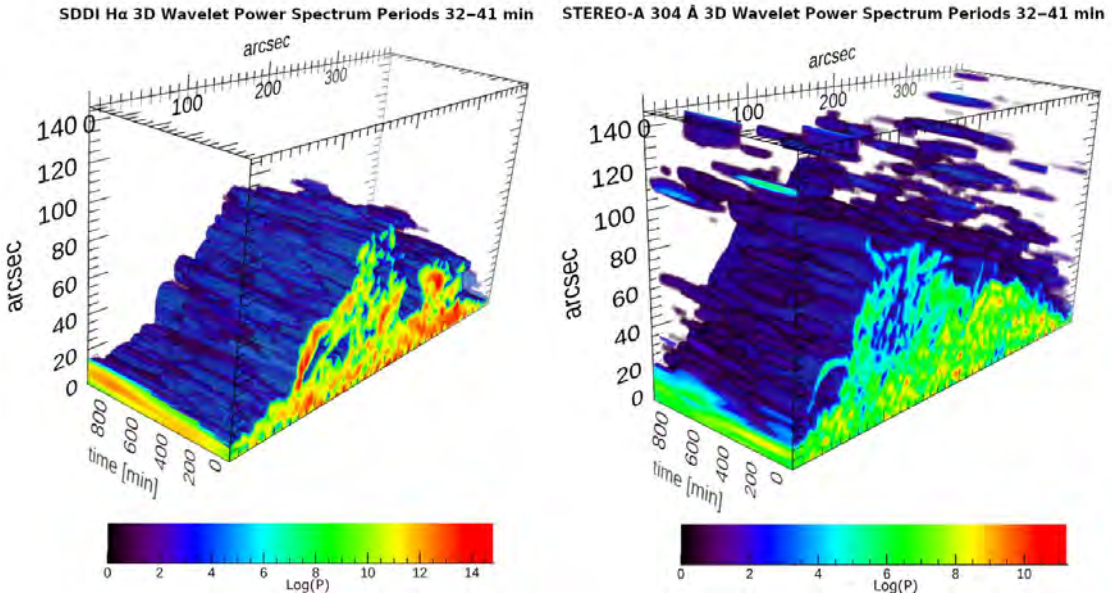

Figure 2.12. *The 3D wavelet power spectra (WPS) of a quiescent prominence, highlighting dominant oscillatory periods in the 32–41 min range. The WPS are derived from Hα Dopplergrams (left panel) obtained with the Solar Dynamics Doppler Imager, and from EUV observations (right panel) acquired in the STEREO-A He II 304 Å passband.*

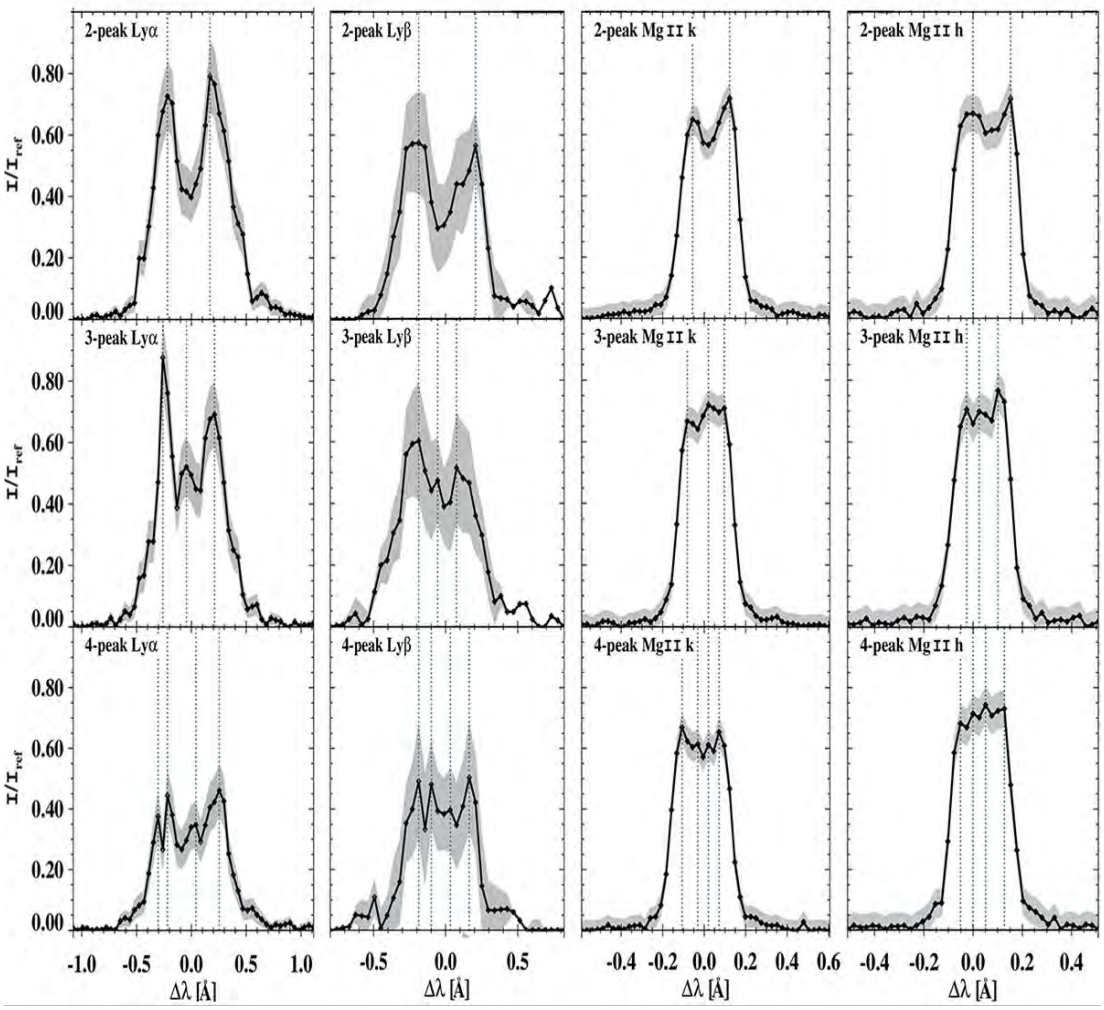

Figure 2.13. *Examples illustrating the diversity of Lyα, Lyβ, Mg II k, and Mg II h spectral line profiles. Columns (from left to right) show profiles observed by the SoHO/SUMER instrument and the IRIS spacecraft. Rows (from top to bottom) display two-, three-, and four-peaked profiles. Peak positions are indicated by vertical dotted lines. The ordinates show the relative intensities (I/I_{ref}). For a given profile type (i.e. within a single row), the Lyman-line profiles originate from different spatial locations and times, whereas the Mg II k and h profiles of that type are co-spatial and co-temporal.*

properties of spectral profile characteristics [12]. The results show that noise has little effect on integrated intensities but strongly influences profile classification by peak number, reversal depth, and asymmetry, making noise treatment essential for reliable prominence diagnostics. Subordinate peaks in the Lyman-line profiles are found to be largely noise-induced, indicating that only dominant peaks should be used in statistical analyses and comparisons with synthetic spectra. In contrast, variations in Mg II k and h profile shapes are closely linked to the dynamics of multiple fine structures along the line of sight: complex, multi-peaked profiles arise from overlapping structures with differing velocities, whereas deeply reversed profiles correspond to single structures or to multiple structures with similar velocities. These results indicate that prominence fine-structure dynamics are best diagnosed using Lyman-line asymmetries together with complex Mg II k and h profiles, while temperature and pressure diagnostics should focus on deeply reversed Mg II k and h lines combined with Lyman-line intensities and reversal depths.

Sulfur is the tenth most abundant element in the universe and plays a significant role in biological systems. However, astrochemistry is facing a great problem related to sulfur chemistry and its abundance in interstellar media. While gas-phase sulfur satisfactorily accounts for its total cosmic abundance in diffuse regions and more primitive interstellar environments, within dense molecular clouds and star-forming regions, there is an unexpected paucity of molecular sulfur. The principal drivers and mechanisms behind this so-called sulfur depletion problem are not fully understood, though a number of experimental and computational studies have suggested various reservoirs that may accommodate this missing sulfur. It was investigated whether simple inorganic sulfur-bearing molecules that could be detected by

Figure 2.14. *Conceptual illustration of the experimental approach used to search for sulfur-bearing molecules. An S-free ice is deposited on a layer of allotropic sulfur supported by a ZnSe substrate. Irradiation with 1 MeV He^+ ions simulates energetic particle processing in astrophysical environments. Energy deposition in the ice and sulfur layer may trigger chemical reactions and mixing, potentially leading to the formation of sulfur-bearing molecular products in the processed ice.*

ground- or space-borne telescopes can be formed in interstellar ices as a result of the irradiation of sulfur-free icy material on top of sulfur-rich dust grains. Neat ices of O2, CO, CO2, and H2O were irradiated on top of layers of allotropic sulfur at 20 K using 1 MeV He+ ions as a mimic of space radiation. A qualitative mid-infrared spectroscopic evidence was found for the synthesis of SO2, CS2, OCS, and H2SO4 hydrates in our experiments and quantified their formation efficiency by calculating the number of molecules formed per 100 eV of deposited energy (the *G*-value) for each ice-refractory system [28]. Reactions leading to the radiolytic synthesis of observed products have been suggested. Regarding the commonly observed radiolysis products SO2 and CS2 in our experiments, it may be worthwhile for future observational studies to search for spectroscopic evidence of CS2 in astrophysical ices, such as in interstellar icy grain mantles, where it may coexist alongside the already detected SO2. In

the contrary, we have not detected formation of H2S in the experiments with water, which suggests that the possible formation and retention of H2S in the ice phase as a result of the cosmic ray or stellar wind irradiation of H2O ice on allotropic sulfur is not efficient, and thus, alternative strategies to explain its hypothesised presence in icy astrophysical environments must be sought. The low G-value of OCS and high G-value of SO2 in our radiation experiments are consistent with recent observational surveys toward protostellar regions that suggest SO2 formation in interstellar ices proceeds primarily *via* an "energetic route" involving radiolytic processes, while OCS forms as a result of "nonenergetic" processes such as atom or radical addition reactions.

References:

[1] BRUNO, G. – PAGANO, I. – SCANDARIATO, G. – FLORÉN, H.-G. – BRANDEKER, A. – OLOFSSON, G. – MAXTED, P. F. L. – FORTIER, A. – SOUSA, S. G. – SULIS, S. – VAN GROOTEL, V. – GARAI, Z. – BOLDOG, A. – KRISKOVICS, L. – SZABÓ, Gy. M. – GANDOLFI, D. – ALIBERT, Y. – ALONSO, R. – BÁRCZY, T. – BARRADO Y NAVASCUES, D. – BARROS, S. C. C. – BAUMJOHANN, W. – BECK, M. – BECK, T. – BENZ, W. – BILLOT, N. – BORSATO, L. – BROEG, C. – COLLIER CAMERON, A. – CSIZMADIA, S. – CUBILLOS, P. E. – DAVIES, M. B. – DELEUIL, M. – DELINE, A. – DELREZ, L. – DEMANGEON, O. D. S. – DEMORY, B.-O. – EHRENREICH, D. – ERIKSON, A. – FARINATO, J. – FOSSATI, L. – FRIDLUND, M. – GILLON, M. – GUEDEL, M. – GÜNTHER, M. N. – HEITZMANN, A. – HELLING, Ch. – HOYER, S. – ISAAK, K. G. – KISS, L. L. – LAM, K. W. F. – LASKAR, J. – LECAVELIER DES ETANGS, A. – LENDL, M. – MAGRIN, D. – MORDASINI, C. – NASCIMBENI, V. – OTTENSAMER, R. – PALLÉ, E. – PETER, G. – PIOTTO, G. – POLLACCO, Don – QUELOZ, D. – RAGAZZONI, R. – RANDO, N. – RATTI, F. – RAUER, H. – RIBAS, I. – SANTOS, N. C. – SARAJLIC, M. – SÉGRANSAN, D. – SIMON, A. E. – SINGH, V. – SMITH, A. M. S. – STALPORT, M. – THOMAS, N. – UDRY, S. – ULMER, B. – VENTURINI, J. – VILLAVER, E. – WALTON, N. – WILSON, T. G. Detailed cool star flare morphology with CHEOPS and TESS. In Astronomy and Astrophysics, 2024, vol. 686, article no. A239, p. 1-27.

[2] FORTIER, A. – SIMON, A. E. – BROEG, C. – OLOFSSON, G. – DELINE, A. – WILSON, T. G. – MAXTED, P. F. L. – BRANDEKER, A. – COLLIER CAMERON, A. – BECK, M. – BEKKELIEN, A. – BILLOT, N. – BONFANTI, A. – BRUNO, G. – CABRERA, J. – DELREZ, L. – DEMORY, B.-O. – FUTYAN, D. – FLORÉN, H.-G. – GÜNTHER, M. N. – HEITZMANN, A. – HOYER, S. – ISAAK, K. G. – SOUSA, S. G. – STALPORT, M. – TURIN, A. – VERHOEVE, P. – AKINSANMI, B. – ALIBERT, Y. – ALONSO, R. – BÁNHIDI, D. – BÁRCZY, T. – BARRADO, D. – BARROS, S. C. C. – BAUMJOHANN, W. – BAYCROFT, T. – BECK, T. – BENZ, W. – BIRÓ, I. B. – BÓDI, A. – BONFILS, X. – BORSATO, Luca – CHARNOZ, S. – CSEH, B. – CSIZMADIA, S. – CSÁNYI, I. – CUBILLOS, P. E. – DAVIES, M. B. – DAVIS, Y. T. – DELEUIL, M. – DEMANGEON, O. D. S. – DEREKAS, A. – DRANSFIELD, G. – DUCROT, E. – EHRENREICH, D. – ERIKSON, A. – FARINA, C. – FOSSATI, L. – FRIDLUND, M. – GANDOLFI, Davide – GARAI, Z. – GARCIA, L. – GILLON, M. – GOMEZ MAQUEO CHEW, Y. – GOMEZ-MUNOZ, M. A. – GRANATA, V. – GUEDEL, M. – GUTERMAN, P. – HEGEDUS, T. – HELLING, Ch. – JEHIN, E. – KALUP, Cs. – KILKENNY, D. – KISS, L. L. – KRISKOVICS, L. – LAM, K. W. F. – LASKAR, J. – LECAVELIER DES ETANGS, A. – LENDL, M. – LOPEZ PINA, A. – LUNTZER, A. – MAGRIN, D. – MILLER, N. J. – MODREGO CONTRERAS, D. – MORDASINI, C. – MUNARI, M. – MURRAY, C. A. – NASCIMBENI, V. – OTTACHER, H. – OTTENSAMER, R. – PAGANO, I. – PÁL, A. – PALLÉ, E. – PASETTI, A. – PEDERSEN, P. P. – PETER, G. –

PETRUCCI, R. – PIOTTO, G. – PIZARRO-RUBIO, A. – POLLACCO, D. – PRIBULLA, Th. – QUELOZ, D. – RAGAZZONI, R. – RANDO, N. – RAUER, H. – RIBAS, I. – SABIN, L. – SANTOS, N. C. – SCANDARIATO, G. – SCHANCHE, N. – SCHROFFENEGGER, U. – SCUTT, O. J. – SEBASTIAN, D. – SÉGRANSAN, D. – SELI, B. – SMITH, A. M. S. – SOUTHWORTH, R. – STANDING, M. R. – SZABÓ, Gy. M. – SZAKÁTS, R. – THOMAS, N. – TIMMERMANS, M. – TRIAUD, A. H. M. J. – UDRY, S. – VAN GROOTEL, V. – VENTURINI, J. – VILLAVER, E. – VINKO, J. – WALTON, N. – WELLS, R. – WOLTER, D. CHEOPS in-flight performance : A comprehensive look at the first 3.5 yr of operations. In Astronomy and Astrophysics, 2024, vol. 687, article no. A302, p. 1-43.

[3] GARAI, Z. – PRIBULLA, Th. – KOMŽÍK, R. Search for the wide-orbit massive companion of XO-7b in the follow-up radial-velocity and transit-timing data: no significant clues. In Monthly Notices of the Royal Astronomical Society, 2024, vol. 527, no. 2, p. 3474-3485.

[4] KARLICKÝ, M. – DUDÍK, J. – RYBÁK, J. Periods and frequency drifts of groups of the decimetric spikes in two solar flares. In Solar Physics, 2024, vol. 299, no. 8, article no. 113, p. 1-16.

[5] KRTIČKA, J. – BENÁČEK, J. – BUDAJ, J. – KORČÁKOVÁ, D. – PÁL, A. – PIECKA, M. – ZEJDA, M. – BAKIS, V. – BROŽ, M. – CHANG, H.-K. – FALTOVÁ, N. – GÁLIS, R. – JADLOVSKÝ, D. – JANÍK, J. – KÁRA, J. – KOLÁŘ, J. – KRTIČKOVÁ, I. – KUBÁT, J. – KUBÁTOVÁ, B. – KURFURST, P. – LABAJ, M. – MERC, J. – MIKULÁŠEK, Z. – MÜNZ, F. – PAUNZEN, E. – PRIŠEGEN, M. – RAMEZANI, T. – RIEVAJOVÁ, T. – ŘÍPA, J. – SCHMIDTOBREICK, L. – SKARKA, M. – SZÁSZ, G. – WEISS, W. W. – ZAJAČEK, M. – WERNER, N. Science with a small two-band UV-photometry mission II: Observations of stars and stellar systems. In Space Science Reviews, 2024, vol. 220, no. 2, art. no. 24, pp. 1-34.

[6] LUKYANYK, I. – KULYK, I. – SHUBINA, O. – PAVLENKO, Ya. – VASYLENKO, M. – DOBRYCHEVA, D. V. – KORSUN, P. Numerical simulations of exocomet transits: Insights from beta Pic and KIC 3542116. In Astronomy and Astrophysics, 2024, vol. 688, article no. A65, p. 1-9.

[7] MIFSUD, D. V. – HERCZKU, P. – RAMACHANDRAN, R. – SUNDARARAJAN, P. – RAHUL, K. K. – KOVÁCS, S. T. S. – SULIK, B. – JUHÁSZ, Z. – RÁCZ, R. – BIRI, S. – KAŇUCHOVÁ, Z. – IOPPOLO, S. – SIVARAMAN, B. – MCCULLOUGH, R. W. – MASON, N. A systematic mid-infrared spectroscopic study of thermally processed H2S ices. In Spectrochimica Acta Part A: Molecular and Biomolecular Spectroscopy, 2024, vol. 319, article no. 124567, p. 1-9.

[8] MIFSUD, D. V. – KAŇUCHOVÁ, Z. – HERCZKU, P. – JUHÁSZ, Z. – KOVÁCS, S. T. S. – LAKATOS, G. – RAHUL, K. K. – RÁCZ, R. – SULIK, B. – BIRI, S. – RAJTA, I. – VAJDA, I. – IOPPOLO, S. – MCCULLOUGH, R. W. – MASON, N. Sulphur ion implantation into O2, CO, and CO2 ices: Implications for the formation of sulphur-bearing molecules in the Kuiper Belt. In Icarus, 2024, vol. 411, article no. 115926, p. 1-12.

[9] RAPPAPORT, S. A. – BORKOVITS, T. – MITNYAN, T. – GAGLIANO, R. – EISNER, N. – JACOBS, T. – TOKOVININ, A. – POWELL, B. P. – KOSTOV, V. B. – OMOHUNDRO, M. – KRISTIANSEN, M. H. – JAYARAMAN, R. – TERENTEV, I. – SCHWENGELER, H. M. – LACOURSE, D. – GARAI, Z. – PRIBULLA, Th. – MAXTED, P. F. L. – BIRÓ, I. B. – CSÁNYI, I. – PÁL, A. – VANDERBURG, A. Seven new triply eclipsing triple star systems. In Astronomy and Astrophysics, 2024, vol. 686, art. no. A27, p. 1-34.

[10] RODRÍGUEZ-GÓMEZ, J. M. – KUCKEIN, Ch. – GONZÁLEZ MANRIQUE, S. J. – SAQRI, J. – VERONIG, A. – GÖMÖRY, P. – PODLADCHIKOVA, T. The plasma β in quiet

Sun regions: Multi-instrument view. In The Astrophysical Journal, 2024, vol. 964, no. 1, article no. 27, p. 1-13.

[11] SCHULTE, J. – RODRIGUEZ, J. E. – BIERYLA, A. – QUINN, S. N. – COLLINS, K. A. – YEE, S. W. – NINE, A. C. – SOARES-FURTADO, M. – LATHAM, D. W. – EASTMAN, J. D. – BARKAOUI, K. – CIARDI, D. R. – DRAGOMIR, D. – EVERETT, M. E. – GIACALONE, S. – MIRELES, I. – MURGAS, F. – NARITA, N. – SHPORER, A. – STRAKHOV, I. A. – STRIEGEL, S. – VAŇKO, M. – VOWEL, N. – WANG, G. – ZIEGLER, C. – BELLAVER, M. – BENNI, P. – BERGERON, S. – BOFFIN, H. M. J. – BRICENO, C. – CLARK, C. A. – COLLINS, K. I. – DE LEON, J. P. – DRESSING, C. D. – EVANS, P. – ESPARZA-BORGES, E. – FEDEWA, J. – FUKUI, A. – GAN, T. – GERASIMOV, I. S. – HARTMAN, J. – GILL, H. – GILLON, M. – HORNE, K. – GRAU HORTA, F. – HOWELL, S. B. – ISOGAI, K. – JEHIN, E. – JENKINS, J. M. – KARJALAINEN, R. – KIELKOPF, J. F. – LESTER, K. V. – LITTLEFIELD, C. – LUND, M. B. – MANN, A. W. – MCCORMACK, M. – MICHAELS, E. J. – PAINTER, S. – PALLÉ, E. – PARVIAINEN, H. – PETERSON, D.-M. – POZUELOS, F. J. – RAUP, Z. – REED, P. – RELLES, H. – RICKER, G. R. – SAVEL, A. B. – SCHWARZ, R. P. – SEAGER, S. – SEFAKO, R. – SRDOC, G. – STOCKDALE, Ch. – SULLIVAN, H. – TIMMERMANS, M. – WINN, J. N., Migration and Evolution of giant ExoPlanets (MEEP). I. Nine newly confirmed hot Jupiters from the TESS mission. The Astronomical Journal, 2024, v. 168, no. 1, article no. 32, p. 1-30.

[12] SCHWARTZ, P. – GUNÁR, S. – KOZA, J. – HEINZEL, P. The diversity of spectral shapes of hydrogen Lyman lines and Mg ii lines in a quiescent prominence. In Astronomy and Astrophysics, 2024, vol. 684, article no. A197, p. 1-25.

[13] ZEMANOVÁ, A. – KARLICKÝ, M. – DUDÍK, J. – KAŠPAROVÁ, J. – RYBÁK, J. Slowly positively drifting bursts generated by large-scale magnetic reconnection. In Astronomy and Astrophysics, 2024, vol. 690, article no. A241, p. 1-16.

[14] ZHANG, J. – TRASPAS MUIÑA, A. – MIFSUD, D. V. – KAŇUCHOVÁ, Z. – CIELINSKA, K. – HERCZKU, P. – RAHUL, K. K. – KOVÁCS, S. T. S. – RÁCZ, R. – SANTOS, J. C. – HOPKINSON, A. T. – CRACIUNESCU, L. – JONES, N. C. – HOFFMANN, S. V. – BIRI, S. – VAJDA, I. – RAJTA, I. – DAWES, A. – SIVARAMAN, B. – JUHÁSZ, Z. – SULIK, B. – LINNARTZ, H. – HORNEKAER, L. – FANTUZZI, F. – MASON, N. – IOPPOLO, S. A systematic IR and VUV spectroscopic investigation of ion, electron, and thermally processed ethanolamine ice. In Monthly Notices of the Royal Astronomical Society, 2024, vol. 533, no. 1, p. 826-840.

[15] DOBRYCHEVA, D. V. – VASYLENKO, M. Yu. – KULYK, I. – PAVLENKO, Ya. – SHUBINA, O. – LUKYANYK, I. V. – KORSUN, P. Hunting for exocomet transits in the TESS database using the Random Forest method. In Kosmična nauka i technologija, 2023, vol. 29, no. 6, p. 68-79.

[16] CHABOT, N. L. – RIVKIN, A. S. – CHENG, A. F. – BARNOUIN, O. S. – FAHNESTOCK, E. G. – RICHARDSON, D. C. – STICKLE, A. M. – THOMAS, C. – ERNST, C. M. – DALY, T. R. – DOTTO, E. – ZINZI, A. – CHESLEY, S. R. – MOSKOVITZ, N. A. – BARBEE, B. V. – ABELL, P. – AGRUSA, H. F. – BANNISTER, M. T. – BECCARELLI, J. – BEKKER, D. L. – SYAL, M. B. – BURATTI, B. J. – BUSCH, M. W. – CAMPO BAGATIN, A. – CHATELAIN, J. – CHOCRON, S. – COLLINS, G. S. – CONVERSI, L. – DAVISON, T. M. – DECOSTER, M. E. – DESHAPRIYA, J. D. P. – EGGL, S. – ESPIRITU, R. C. – FARNHAM, T. – FERRAIS, M. – FERRARI, F. – FÖHRING, D. – FUENTES-MUNOZ, O. – GAI, I. – GIORDANO, C. – GLENAR, D. A. – GOMEZ, E. – GRANINGER, D. M. – GREEN, S. F. – GREENSTREET, S. – HASSELMANN, P. H. – HERREROS, I. – HIRABAYASHI, M.

– HUSÁRIK, M. – IEVA, S. – IVANOVSKI, S. L. – JACKSON, S. L. – JEHIN, E. – JUTZI, M. – KARATEKIN, O. – KNIGHT, M. M. – KOLOKOLOVA, L. O. – KUMAMOTO, K. M. – KUPPERS, M. – LA FORGIA, F. – LAZZARIN, M. – LI, J.-Y. – LISTER, T. – LOLACHI, R. – LUCAS, M. P. – LUCCHETTI, A. – LUTHER, R. – MAKADIA, R. – MAZZOTTA EPIFANI, E. – MCMAHON, J. – MERISIO, G. – MERRILL, C. C. – MEYER, A. J. – MICHEL, P. – MICHELI, M. – MIGLIORINI, A. – MINKER, K. – MODENINI, D. – MORENO, F. – MURDOCH, N. – MURPHY, B. – NAIDU, S. P. – NAIR, H. – NAKANO, R. – OPITOM, C. – ORMO, J. – OWEN, M. – PAJOLA, M. – PALMER, E. E. – PALUMBO, P. – PANICUCCI, P. – PARRO, L. M. – PEARL, J. M. – PENTILLA, A. – PERNA, D. – PETRESCU, E. – PRAVEC, P. – RADUCAN, S. D. – RAMESH, K. T. – RIDDEN-HARPER, R. – RIZOS, J. L. – ROSSI, A. – ROTH, N. X. – ROZEK, A. – ROZITIS, B. – RYAN, E. – RYAN, William – SANCHEZ, Paul – SANTANA-ROS, T. – SCHEERES, D. J. – SCHEIRICH, P. – SENEL, C. B. – SNODGRASS, C. – SOLDINI, S. – SOUAMI, D. – STATLER, T. S. – STREET, R. – STUBBS, T. J. – SUNSHINE, J. M. – TAN, N. J. – TANCREDI, G. – TINSMAN, C. L. – TORTORA, P. – TUSBERTI, F. – WALKER, J. D. – WALLER, C. D. – WUNNEMANN, K. – ZANNONI, M. – ZHANG, Y. Achievement of the planetary defense investigations of the double asteroid redirection test (DART) mission. In The Planetary Science Journal, 2024, vol. 5, no. 2, article no. 49, p. 1-24.

[17] MOSKOVITZ, N. A. – THOMAS, C. – PRAVEC, P. – LISTER, T. – POLAKIS, T. – OSIP, D. J. – KARETA, T. – ROZEK, A. – CHESLEY, S. R. – NAIDU, S. P. – SCHEIRICH, P. – RYAN, W. – RYAN, E. – SKIFF, B. A. – SNODGRASS, C. – KNIGHT, M. M. – RIVKIN, A. S. – CHABOT, N. L. – AYVAZIAN, V. – BELSKAYA, I. – BENKHALDOUN, Z. – BERTESTEANU, D. N. – BONAVITA, M. – BRESSI, T. H. – BRUCKER, M. J. – BURGDORF, M. J. – BURKHONOV, O. – BURT, B. – CONTRERAS, C. – CHATELAIN, J. – CHOI, Y.-J. – DAILY, M. – DE LEON, J. – KAMOLIDDIN, E. – FARNHAM, T. – FATKA, P. – FERRAIS, M. – GEIER, S. – GOMEZ, E. – GREENSTREET, S. – GRÖLLER, H. – HERGENROTHER, C. – HOLT, C. – HORNOCH, K. – HUSÁRIK, M. – INASARIDZE, R. – JEHIN, E. – KHALOUEI, E. – KIKWAYA ELUO, J.-B. – KIM, M.-J. – KRUGLY, Y. N. – KUČÁKOVÁ, H. – KUŠNIRÁK, P. – LARSEN, J. A. – LEE, H.-J. – LEJOLY, C. – LICANDRO, J. – LONGA-PEÑA, P. – MASTALER, R. A. – MCCULLY, C. – MOON, H.-K. – MORRELL, N. – NATH, A. – OSZKIEWICZ, D. – PARROTT, D. – PHILLIPS, L. – POPESCU, M. – PRAY, D. P. – PANTELIMON PRODAN, G. – RABUS, M. – READ, M. T. – REVA, I. – ROARK, V. – SANTANA-ROS, T. – SCOTTI, J. V. – TATARA, T. – THIROUIN, A. – THOLEN, D. – TROIANSKYI, V. – TUBBIOLO, A. F. – VILLA, K. Photometry of the Didymos system across the DART impact apparition. In The Planetary Science Journal, 2024, vol. 5, no. 2, article no. 35, p. 1-28.

[18] GARAI, Z. – OSBORN, H. P. – TUSON, A. – ULMER-MOLL, S. Confirming long-period transiting exoplanets with TESS and CHEOPS : The case of HD 22946 d. In Contributions of the Astronomical Observatory Skalnaté Pleso, 2024, vol. 54, no. 2, pp. 150-156.

[19] LEITZINGER, M. – KABÁTH, P. – VAŇKO, M. – PRIBULLA, Th. – KOMŽÍK, R. – GARAI, Z. – KARJALAINEN, R. – ODERT, P. – LIPTÁK, J. – HEINZEL, P. – WOLLMANN, J. – GREIMEL, R. – GUENTHER, E. Spectroscopic characterization of superflares on solar-type stars - a joint observing campaign. In Contributions of the Astronomical Observatory Skalnaté Pleso, 2024, vol. 54, no. 2, p. 190-193.

[20] MALIUK, A. – BUDAJ, J. – MKRTICHIAN, D. – GARAI, Z. – ZHARIKOV, S. – PRIBULLA, Th. – KOMŽÍK, R. – KUSAKIN, A. – SHESTAKOVA, L. – KOKUMBAEVA, R. I. – REVA, I. – JOSHI, S. – VALEEV, A. F. – GADELSHIN, D. – VALYAVIN, G. – A-THANO, N. – MENNICKENT, R. – SEREBRYANSKIY, A. – KAYE, T. G. Studying of

exoasteroids orbiting around WD 1145 + 017. In Contributions of the Astronomical Observatory Skalnaté Pleso, 2024, vol. 54, no. 2, p. 98-106.

[21] MESARČ, M. – HAMBÁLEK, Ľ. Validation of selected TESS exoplanetary candidates. In Contributions of the Astronomical Observatory Skalnaté Pleso, 2024, vol. 54, no. 2, p. 219-227.

[22] SKOPAL, A. Exploring outbursts of accreting white dwarfs in symbiotic binaries - basic concept. In Contributions of the Astronomical Observatory Skalnaté Pleso, 2024, vol. 54, no. 2, p. 85-97.

[23] BOLDOG, A. – SZABÓ, Gy. M. – KRISKOVICS, L. – BORSATO, L. – GANDOLFI, D. – LENDL, M. – GÜNTHER, M. N. – HEITZMANN, A. – WILSON, T. G. – BRANDEKER, A. – GARAI, Z. – ALIBERT, Y. – ALONSO, R. – BÁRCZY, T. – BARRADO Y NAVASCUES, D. – BARROS, S. C. C. – BAUMJOHANN, W. – BENZ, W. – BILLOT, N. – BROEG, C. – COLLIER CAMERON, A. – CORREIA, A. C. M. – CSIZMADIA, S. – CUBILLOS, P. E. – DAVIES, M. B. – DELEUIL, M. – DELINE, A. – DEMANGEON, O. D. S. – DEMORY, B.–O. – DEREKAS, A. – EDWARDS, B. – EGGER, J. A. – EHRENREICH, D. – ERIKSON, A. – FORTIER, A. – FOSSATI, L. – FRIDLUND, M. – GAZEAS, K. – GILLON, M. – GUEDEL, M. – GUTERMAN, P. – HELLING, Ch. – ISAAK, K. G. – KISS, L. L. – KOPP, E. – KORTH, J. – LAM, K. W. F. – LASKAR, J. – LECAVELIER DES ETANGS, A. – LUNTZER, A. – MAGRIN, D. – MANTOVAN, G. – MARAFATTO, L. – MAXTED, P. F. L. – MERÍN, B. – MORDASINI, C. – MUNARI, M. – NASCIMBENI, V. – OLOFSSON, G. – OTTENSAMER, R. – PAGANO, I. – PALLÉ, E. – PETER, G. – PIAZZA, D. – PIOTTO, G. – POLLACCO, D. – POPPENHAEGER, K. – QUELOZ, D. – RAGAZZONI, R. – RANDO, N. – RAUER, H. – RIBAS, I. – RIEDER, M. – SANTOS, N. C. – SCANDARIATO, G. – SÉGRANSAN, D. – SIMON, A. E. – SMITH, A. M. S. – SOUSA, S. G. – SOUTHWORTH, R. – STALPORT, M. – SULIS, S. – UDRY, S. – ULMER-MOLL, S. – VAN GROOTEL, V. – VENTURINI, J. – VILLAVER, E. – WALTON, N. – ZINGALES, T. Transit-timing variations in the AU Mic system observed with CHEOPS. In Astronomy and Astrophysics, 2025, vol. 694, article no. A137, p. 1-15.

[24] BUDAJ, J. – BERNHARD, K. – JONES, D. – MUNDAY, J. A swarm of dusty objects in orbit around the central star of planetary nebula WeSb1. In Nature Astronomy, 2025, vol. 9, no. 3, p. 380-392.

[25] FIORI, M. – ZAMPIERI, L. – BURTOVOI, A. – NALETTO, G. – OCHNER, P. – MUNARI, U. – MANZINI, F. – VAGNOZZI, A. – BARSUKOVA, E. A. – BURLAK, M. – GORANSKIJ, V. P. – IKONNIKOVA, N. – KATYSHEVA, N. A. – SHEYANOV, E. G. – SHUGAROV, S. – ZHAROVA, A. V. – ZUBAREVA, A. M. – MOTTA, S. E. Optical and X-ray timing analysis of the 2018-2020 outburst and rebrightening of the black hole transient MAXI J1820+070. In Astronomy and Astrophysics, 2025, vol. 697, article no. A222, p. 1-18.

[26] GARAI, Z. – KRENN, A. – CUBILLOS, P. E. – BRUNO, G. – SMITH, A. M. S. – WILSON, T. G. – BRANDEKER, A. – GÜNTHER, M. N. – HEITZMANN, A. – CARONE, L. – SINGH, V. – LENDL, M. – DEMANGEON, O. D. S. – ALIBERT, Y. – ALONSO, R. – ASQUIER, J. – BÁRCZY, T. – BARRADO, D. – BARROS, S. C. C. – BAUMJOHANN, W. – BENZ, W. – BILLOT, N. – BORSATO, L. – BROEG, C. – COLLIER CAMERON, A. – CORREIA, A. C. M. – CSIZMADIA, S. – DAVIES, M. B. – DELEUIL, M. – DELINE, A. – DEMORY, B.-O. – DEREKAS, A. – EDWARDS, B. – EGGER, J. A. – EHRENREICH, D. – ERIKSON, A. – FARINATO, J. – FORTIER, A. – FOSSATI, L. – FRIDLUND, M. – GANDOLFI, D. – GAZEAS, K. – GILLON, M. – GUEDEL, M. – HELLING, Ch. – ISAAK, K. G. – KERSCHBAUM, F. – KISS, L. L. – KORTH, J. – LAM, K. W. F. – LASKAR, J. –

LECAVELIER DES ETANGS, A. – MAGRIN, D. – MAXTED, P. F. L. – MERÍN, B. – MORDASINI, C. – NASCIMBENI, V. – OLOFSSON, G. – OTTENSAMER, R. – PAGANO, I. – PALLÉ, E. – PETER, G. – PIAZZA, D. – PIOTTO, G. – POLLACCO, D. – QUELOZ, D. – RAGAZZONI, R. – RANDO, N. – RAUER, H. – RIBAS, I. – SANTOS, N. C. – SCANDARIATO, G. – SÉGRANSAN, D. – SIMON, A. E. – SOUSA, S. G. – STALPORT, M. – SULIS, S. – SZABÓ, Gy. M. – UDRY, S. – ULMER-MOLL, S. – VAN GROOTEL, V. – VENTURINI, J. – VILLAVER, E. – WALTON, N. – WOLF, S. – WOLTER, D. – ZINGALES, T. The KELT-7b atmospheric thermal-inversion conundrum revisited with CHEOPS, TESS, and additional data. In Astronomy and Astrophysics, 2025, vol. 700, article no. A5, p. 1-26.

[27] KAŇUCHOVÁ, Z. – BORCHERT, L. E. – MIFSUD, D. V. – TRASPAS MUIÑA, A. – WILSON, A. M. – PROCHAL, M. – JONES, N. C. – HOFFMANN, S. V. – CASSIDY, A. – HORNEKAER, L. – MASON, N. – STRAZZULLA, G. – IOPPOLO, S. Vacuum ultraviolet photoabsorption spectroscopy of space-related ices: Formation of (cyano)polyynes in 1 keV electron irradiated hydrocarbon-rich ices. In Astronomy and Astrophysics, 2025, vol. 700, article no. A115, p. 1-19.

[28] MIFSUD, D. V. – KAŇUCHOVÁ, Z. – AURIACOMBE, O. – HERCZKU, P. – QASIM, D. – KOVÁCS, S. T. S. – RÁCZ, R. – SULIK, B. – JUHÁSZ, Z. – RAJTA, I. – VAJDA, I. – BIRI, S. – MCCULLOUGH, R. W. – IOPPOLO, S. – RAUT, U. – MASON, N. Cosmic ray irradiation of interstellar ices on sulfur-rich grains: A possible source of sulfur-bearing molecules. In ACS Earth and Space Chemistry, 2025, vol. 9, p. 1227-1242.

[29] SKOPAL, A. – SHAGATOVA, N. V1047 Cen: The first Z And-type outburst observed in the classical nova binary. In The Astrophysical Journal, 2025, vol. 983 no. 2, article no. 148, p. 1-11.

[30] YU, H. – GARAI, Z. – CRETIGNIER, M. – SZABÓ, Gy. M. – AIGRAIN, S. – GANDOLFI, D. – BRYANT, E. M. – CORREIA, A. C. M. – KLEIN, B. – BRANDEKER, A. – OWEN, J. E. – GÜNTHER, M. N. – WINN, J. N. – HEITZMANN, A. – CEGLA, H. M. – WILSON, T. G. – GILL, S. – KRISKOVICS, L. – BARRAGÁN, O. – BOLDOG, A. – NIELSEN, L. D. – BILLOT, N. – LAFARGA, M. – MEECH, A. – ALIBERT, Y. – ALONSO, R. – BÁRCZY, T. – BARRADO, D. – BARROS, S. C. C. – BAUMJOHANN, W. – BAYLISS, D. – BENZ, W. – BERGOMI, M. – BORSATO, L. – BROEG, C. – COLLIER CAMERON, A. – CSIZMADIA, S. – CUBILLOS, P. E. – DAVIES, M. B. – DELEUIL, M. – DELINE, A. – DEMANGEON, O. D. S. – DEMORY, B.-O. – DEREKAS, A. – DOYLE, L. – EDWARDS, B. – EGGER, J. A. – EHRENREICH, D. – ERIKSON, A. – FORTIER, A. – FOSSATI, L. – FRIDLUND, M. – GAZEAS, K. – GILLON, M. – GUEDEL, M. – HELLING, Ch. – ISAAK, K. G. – KISS, L. L. – KORTH, J. – LAM, K. W. F. – LASKAR, J. – LECAVELIER DES ETANGS, A. – LENDL, M. – MAGRIN, D. – MAXTED, P. F. L. – MCCORMAC, J. – MERÍN, B. – MORDASINI, C. – NASCIMBENI, V. – O';BRIEN, S. M. – OLOFSSON, G. – OTTENSAMER, R. – PAGANO, I. – PALLÉ, E. – PETER, G. – PIAZZA, D. – PIOTTO, G. – POLLACCO, D. – QUELOZ, D. – RAGAZZONI, R. – RANDO, N. – RAUER, H. – RIBAS, I. – SANTOS, N. C. – SCANDARIATO, G. – SÉGRANSAN, D. – SIMON, A. E. – SMITH, A. M. S. – SOUSA, S. G. – SOUTHWORTH, R. – STALPORT, M. – STEINBERGER, M. – SULIS, S. – UDRY, S. – ULMER, B. – ULMER-MOLL, S. – VAN GROOTEL, V. – VENTURINI, J. – VILLAVER, E. – WALTON, N. – WHEATLEY, P. J. A possible misaligned orbit for the young planet AU Mic c. In Monthly Notices of the Royal Astronomical Society, 2025, vol. 536, no. 3, p. 2046-2063.

[31] DZYGUNENKO, A. – BARANSKY, O. – KRUSHEVSKA, Viktoriia. Physical parameters of superhumps in five dwarf nova systems based on TESS observations. In

Kinematics and Physics of Celestial Bodies : space physics, 2025, vol. 41, no. 5, p. 187-196.

[32] ORTIZ, J. L. – MORALES, N. – SICARDY, B. – ROMMEL, F. L. – BRAGA-RIBAS, F. – KILIC, Y. – FERNANDEZ-VALENZUELA, E. – RIZOS, J. L. – MORGADO, B. – CATANI, L. – KRETLOW, M. – GÓMEZ-LIMÓN, J. M. – DESMARS, J. – SANTOS-SANZ, P. – ERECE, O. – AKOZ, I. – ULUC, K. – KASPI, S. – MARCINIAK, A. – TURCU, V. – MOLDOVAN, D. – SONKA, A. – PETRESCU, E. – NEDELCU, A. – NEHIR, C. – MORALES, R. – DUFFARD, R. – SOUAMI, D. – THUILLOT, W. – CAMARGO, J. I. B. – VIEIRA-MARTINS, R. – LECACHEUX, J. – ALVAREZ-CANDAL, A. – ASSAFIN, M. – BENEDETTI-ROSSI, G. – GOMES-JUNIOR, A. R. – BOUFLEUR, R. C. – HOPP, U. – GOESSL, C. – SCHMIDT, M. – TAKEY, A. – ABDELAZIZ, A. M. – MIKUZ, H. – MOHAR, A. – SKVARČ, J. – SCHREURS, O. – LECOSSOIS, M. – JANIK, T. – BAGIRAN, M. N. – FIEK, S. – ALIS, S. – YELKENCI, F. K. – ACAR, M. – TAKACS, N. – SZAKÁTS, R. – PÁL, A. – MÁNEK, J. – DUMITRU, B. A. – GAZEAS, K. – URSACHE, F. – NARDIELLO, D. – NASCIMBENI, V. – ROTTENBORN, M. – SONBAS, E. – OGLOZA, W. – NASTASI, A. – LEONINI, S. – CONTI, M. – ROSI, P. – TINJACA RAMIREZ, L. M. – BELLIZI, L., astro - MARCHINI, A. – VERNA, G. – SOLMAZ, A. – TEKES, M. – ANTUSZEWICZ, D. – PICA, D. – ILIC, D. – GROZDANOVIC, M. – STOIAN, L. – BACCI, P. – MAESTRIPIERI, M. – KRANNICH, G. – BACCI, R. – ALTAN, M. – HORNOCH, K. – NESCI, R. – CIABATTARI, F. – SZABÓ, Gy. M. – KOVÁCS, J. – GARAI, Z. – BORA, Z. – ZELENY, P. – GAEHRKEN, B. – FIEDLER, M. – CURELARU, L. – ION, S. – SCHAEFER, R. – KUBÁNEK, J. – DELINCAK, P. – KALKAN, S. A high geometric albedo and small size for the Haumea cluster member (24835) 1995 SM55 determined from a stellar occultation and photometric observations. In *Astronomy and Astrophysics*, 2025, vol. 703, article no. A147, p. 1-13.

[33] WIŚNIEWSKA, A. – ICHIMOTO, K. – KOZA, J. – KONTOGIANNIS, I. – PIETROW, A. G. M. – MURO, G. D. – GÖMÖRY, P. Wave Period Variability in a Quiescent Solar Prominence, In The Astrophysical Journal, 2025, vol. 995, no. 1, p. 17.

3. LIFE SCIENCES

M. Musilová

At this time, life sciences research in Slovakia, related to the space sector, is primarily performed through a non-profit organization called Michaela Musilová, o.z. The non-profit is focused on astrobiology and human space exploration research and educational activities, in collaboration with multiple Slovak and international partners. The Slovak collaborating organizations include the Comenius University Science Park, and the Cosmic Region simulated space station at the Rožňava Observatory. Teams from the NASA Goddard Space Flight Center, NASA Headquarters, University of Maryland, Georgetown University, University of Zurich, Honeybee Robotics and others are among the international partners of the non-profit's projects.

The research of Michaela Musilová, o.z.'s team can be subdivided into two main areas. First of all, it is concerned with studying the limits of life in extreme environments to define the possibilities of where to search for life beyond Earth for astrobiology purposes. This research also has applications to the pharmaceutical, food and other industries, since substances from these extreme life-forms (so-called extremophiles) can enhance the products of these industries. The second area of research involves studying human behaviour in isolated and extreme and/or confined conditions with the goal of preparing humans for long duration space exploration missions.

The astrobiology-focused research projects include Astro Seven Summits, which involves performing a series of scientific and educational expeditions to the summits of the tallest mountain on each continent (the Seven Summits), in collaboration with NASA, the Comenius University Science Park in Slovakia and multiple other institutions around the world. Michaela Musilová, o.z.'s lead scientist collects biochemical, microbiological and geological samples to understand what lifeforms can survive in these extreme conditions and whether similar extreme lifeforms could potentially survive in similar environments on Mars. The team also conducts sensor measurements to evaluate the changing environmental conditions in some of the most extreme habitats on the planet.

With regards to the human space exploration research by Michaela Musilová, o.z., it is being performed during the Astro Seven Summits expeditions in collaboration with the University of Zurich, as well as in collaboration with the European Space Agency (ESA) and the newly established Cosmic Region simulated space station at the Rožňava Observatory in Slovakia. The collaboration with the University of Zurich involves performing psychological studies of human performance in small teams under stressful conditions during expeditions in isolated and extreme environments.

As for the collaboration with ESA, Michaela Musilová, o.z.'s lead scientist was asked to join ESA's Topical Team to evaluate space analogs and the behavioral health performance research that is conducted during simulated space missions. The Topical Team reviewed analog space habitats and their missions worldwide and prepared a recommendations checklist for ESA and future simulated space missions.

Finally, the Cosmic Region station was created in collaboration with Michaela Musilová, o.z. in 2025 to provide a facility for simulated space mission research, as well as educational and outreach programs. Michaela Musilová, o.z.'s lead scientist is the main person overseeing the research aspects of the Cosmic Region, since they have experience with organizing over 40 simulated missions to the Moon and Mars. These missions were performed in collaboration with NASA, ESA and numerous other space organizations and companies from around the world.

A simulated space mission involves a crew of six people living as if they were on the Moon or Mars, while performing various scientific and engineering projects. This means that they are subject to time delays when communicating with the Mission Control Centre on 'Earth', they eat freeze-dried astronaut-like food and they have to survive on their own with very limited supplies of all the materials they bring with them. They are also isolated from the rest of the world, as if they were truly on another planet. The missions typically last from several days up to a whole year, depending on the research goals of the mission.

The overall objectives of analog space missions are to field-test scientific and technological initiatives aimed to help humans return to the Moon and explore Mars one day. Cosmic Region's goal is not only to perform simulated space missions, but also to provide possibilities for research in astrobiology, geology, engineering, psychology, physiology, botany, in situ resource utilization and others. Additionally, when the facility isn't being used for research purposes, it can be used for educational and outreach activities.

Michaela Musilová, o.z.'s representatives regularly present about these varied research projects worldwide at multiple international conferences, including the International Astronautical Congress (IAC) run by the International Astronautical Federation (IAF), American Geophysical Union (AGU), European Geophysical Union (EGU), Europlanet Science Congress (EPSC), Lunar and Planetary Science Conference (LPSC), various NASA workshops and forums, COSPAR Scientific Assembly and others. Michaela Musilová, o.z.'s team is currently preparing several peer-reviewed publications from the results of their research as well. Michaela Musilová, o.z.'s lead scientist is also a reviewer for the NASA Planetary Protection Research Program and many other grant programs and research journals in space life sciences, such as Astrobiology and the National Science Foundation. Additionally, they are a Global Faculty of the International Space University, where they lecture and organize workshops in astrobiology, and the robotic and human exploration of the Moon and Mars.

Michaela Musilová, o.z.'s lead scientist is performing geobiochemical studies and sampling for astrobiology research during a NASA scientific expedition in Iceland in 2025. (Photo credit: Michaela Musilova)

The Astro Seven Summits project lead is examining extreme lifeforms that can survive in challenging cold conditions with limited nutrient availability for astrobiology research during their expedition to Mount Vinson – the tallest mountain in Antarctica. (Photo credit: Michaela Musilova)

Sensors, developed by Slovak high school and university students, are being tested by Michaela Musilová, o.z.'s lead scientist during their expedition to Mount Everest – the tallest mountain in Asia and the world. (Photo credit: Michaela Musilova)

There are a couple of other Slovak scientists performing space life sciences research in collaboration with international institutions. Their research also includes astrobiology and analog space mission studies. A Slovak scientist is part of research conducted by the Space Agri Technologies Department of Chemistry and Biochemistry Mendel University in the Czech Republic. Their research has implications for life-support systems during space missions and future settlements on the Moon and Mars. In particular, they're studying cyanobacteria through synthetic biology. They're trying to see if these types of organisms could be used to improve current bioregenerative life-support and in situ biomanufacturing plans for future long-duration crewed missions. These microbes could potentially help reduce the resupply dependence of human space missions and improve the performance of planned crop systems in controlled space habitats and extraterrestrial cultivation scenarios.

Furthermore, two Slovak scientists, including the principal investigator, were involved in a Czech-Taiwanese consortium led by the Hydronaut Project in Prague, Czech Republic, between 2023 and 2025. They developed a platform to assess and maintain the physical fitness of teams operating in isolated, confined and extreme (ICE) environments. The primary objective of the project was to study and mitigate the negative effects of ICE conditions on human physical health. To achieve this, a tool called the "Virtual Trainer" was developed, which incorporates various biosensors utilizing artificial intelligence/machine learning and augmented reality. The Virtual Trainer consists of hardware, software and exercise routines specifically designed for the ICE environment. It provides real-time feedback to users and visualizes correct exercise execution. The tool was tested during analog space missions at the DeepLab H03 habitat in Little Moon City, Prague in the Czech Republic, with support from the Czech Technological Agency under the Delta program (Project number TM04000062).

References:

[1] DE LA TORRE, G. G. – GROEMER, G. – DIAZ-ARTILES, A. – PATTYN, N. – VAN CUTSEM, J. – MUSILOVÁ, M. *et al.* (2024) Space Analogs and Behavioral Health Performance Research review and recommendations checklist from ESA Topical Team. *npj Microgravity,* **10**, 98, doi: https://doi.org/10.1038/s41526-024-00437-w

[2] MUSILOVÁ, M. – MOLNÁR, Z. – KLEINOVÁ, A. (2025) Space analogs as a means to engage school children in STEM subjects. *Proceedings of the 76th International Astronautical Congress (IAC) by the International Astronautical Federation (IAF)*, 29 September – 3 October 2025, Sydney, Australia. Paper IAC- 25,E5,6,9,x101033

[3] PĚNČÍK, O. – KOLÁČKOVÁ, M. – MOLNAROVÁ, K. – HÚSKA, D. (2025) What would a hypothetical supercyanobacterium look like? *Trends in Biotechnology*, Volume 43, Issue 10, 2410-2426, ISSN 0167-7799, doi: https://doi.org/10.1016/j.tibtech.2025.04.006.

[4] HEJDA, J. – SOKOL, M. – LEOVÁ, L. – VOLF, P. – TONNER, J. – HSU, W.-C. – LIN, Y.-J. -SUGIARTO, T. – ROZLOŽNÍK, M. – KUTÍLEK, P. (2026). Multimodal Wearable Monitoring of Exercise in Isolated, Confined, and Extreme Environments: A Standardized Method. *Methods and Protocols*, *9*(1), 15. doi: https://doi.org/10.3390/mps9010015

4. RESEARCH IN MATERIALS AND TECHNOLOGIES FOR SPACE APPLICATIONS

M. Gebura, N. Beronská, E. Hodúlová, T. Dvorák, L. Karaffa, R. Sekerka, M. Čavojský

During the 2024–2025 reporting period, the Institute of Materials and Machine Mechanics of the Slovak Academy of Sciences (IMSAS) continued and significantly advanced its research on Contact Capacitor Discharge Stud (CCDS) welding for space applications. The results presented here from high-level perspective represent the final experimental phase of the ESA PECS contract *"**Feasibility Study of Contact Capacitor Discharge Welding Gear for In-orbit and Lunar Applications**"* (Contract No. 4000141916/23/NL/MH/rp), with a primary focus on validating the robustness, repeatability, and mechanical relevance of CCDS joining under space-representative vacuum conditions. The final presentation of this activity is already planned on 30th of April 2026.

The research activities concentrated on two scenarios defined as non-impact welding without electrical breakdown (with spring loaded stud being in contact to the workpiece), and impact welding without electrical breakdown (stud ejected from above the workpiece surface by the means of actuated spring assembly towards the workpiece) which are both particularly relevant for robotic in-orbit assembly where controlled mechanical contact and predictable energy input are required.

4.1. Experimental Infrastructure Overview

During the 2024–2025 reporting period, IMSAS completed the development and commissioning of a dedicated experimental infrastructure for the investigation of Contact Capacitor Discharge Stud (CCDS) welding under space-representative conditions. The infrastructure was designed to enable controlled, repeatable experiments combining **vacuum environment, high-power pulsed electrical systems, mechanical loading, and synchronized diagnostics**, forming the experimental backbone for the CCDS feasibility study.

The infrastructure integrates three core subsystems:

1. a laboratory-scale CCDS welding system with modular power electronics,
2. an upgraded vacuum chamber and pumping system,
3. an instrumented laboratory model of the welding end-effectors and workpiece interface.

The laboratory model allows:

- precise control of discharge voltage and energy,
- integration of current and voltage probes (I-probe and V-probe),
- high-bandwidth acquisition of electrical and mechanical signals,
- flexible adaptation to different stud geometries and surface conditions.
- Variations in spring assembly to control loading conditions for welding

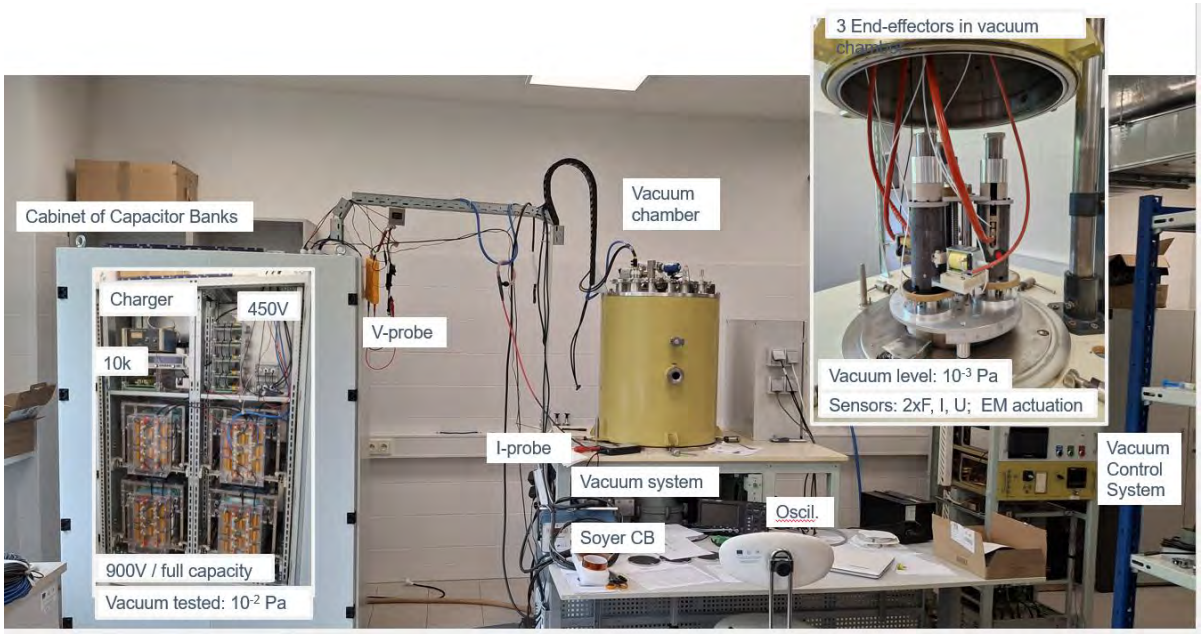

Figure 4.1. *Assembled CCDS laboratory infrastructure integrated with the vacuum chamber. The setup includes a modular capacitor bank system with high-voltage charger, current and voltage probes, oscilloscope-based data acquisition, and an instrumented vacuum chamber. The inset shows multiple welding end-effectors installed inside the chamber during vacuum operation (10^{-3} Pa), enabling simultaneous measurement of force, current, voltage, and electromechanical actuation during CCDS welding experiments.*

The welding head and workpiece interface were deliberately designed to allow slight misalignment and compliance, reflecting realistic conditions expected during robotic in-orbit assembly rather than idealized laboratory contact.

The CCDS laboratory model was integrated into an upgraded vacuum chamber system equipped with rotary and diffusion pumps. The chamber was modified to accommodate multiple electrical, mechanical, and diagnostic feedthroughs, enabling operation of the welding system and sensors directly inside the vacuum environment. Functional tests of the upgraded vacuum infrastructure demonstrated the ability to reach pressures on the order of **10^{-3} Pa** within approximately 1–2 hours, even with the welding end-effector and associated cabling installed inside the chamber. This pressure range is representative of low Earth orbit conditions and sufficient to suppress atmospheric effects such as oxidation and gas-assisted arc behaviour during welding.

The vacuum control system provides continuous monitoring of chamber pressure and stable operation during welding experiments, ensuring reproducible environmental conditions across test campaigns.

The experimental infrastructure was instrumented to enable **synchronized, multi-modal diagnostics**, which is essential for understanding CCDS joining behaviour. The system supports simultaneous measurement of:

- welding current and voltage,
- instant electrical power,
- dynamics of the mechanical forces acting on the stud and substrate,
- vacuum pressure during operation.

This instrumentation framework enabled the identification of characteristic electro-mechanical process signatures associated with high-quality CCDS joints, as discussed in the

subsequent results sections. The developed infrastructure does not represent a finalized flight system, but rather a **research-grade experimental platform** specifically tailored to study CCDS welding physics under space-relevant conditions. Its modular design allows systematic variation of:

- environmental conditions (air vs vacuum),
- surface states (bare, anodized, painted, insulated),
- electrical parameters,
- mechanical compliance at the interface.

4.2. Systematic Weldability Mapping

A comprehensive weldability matrix was experimentally evaluated using AA6061-T6 aluminium alloy workpieces and commercially available ISO 13918 studs. The study covered a wide range of discharge voltages, stud materials, and surface conditions, including bare metallic surfaces, anodized layers, painted coatings, Kapton tape, and multi-layer insulation (MLI). Experiments were performed both under atmospheric conditions and in vacuum (10^{-3} Pa level).

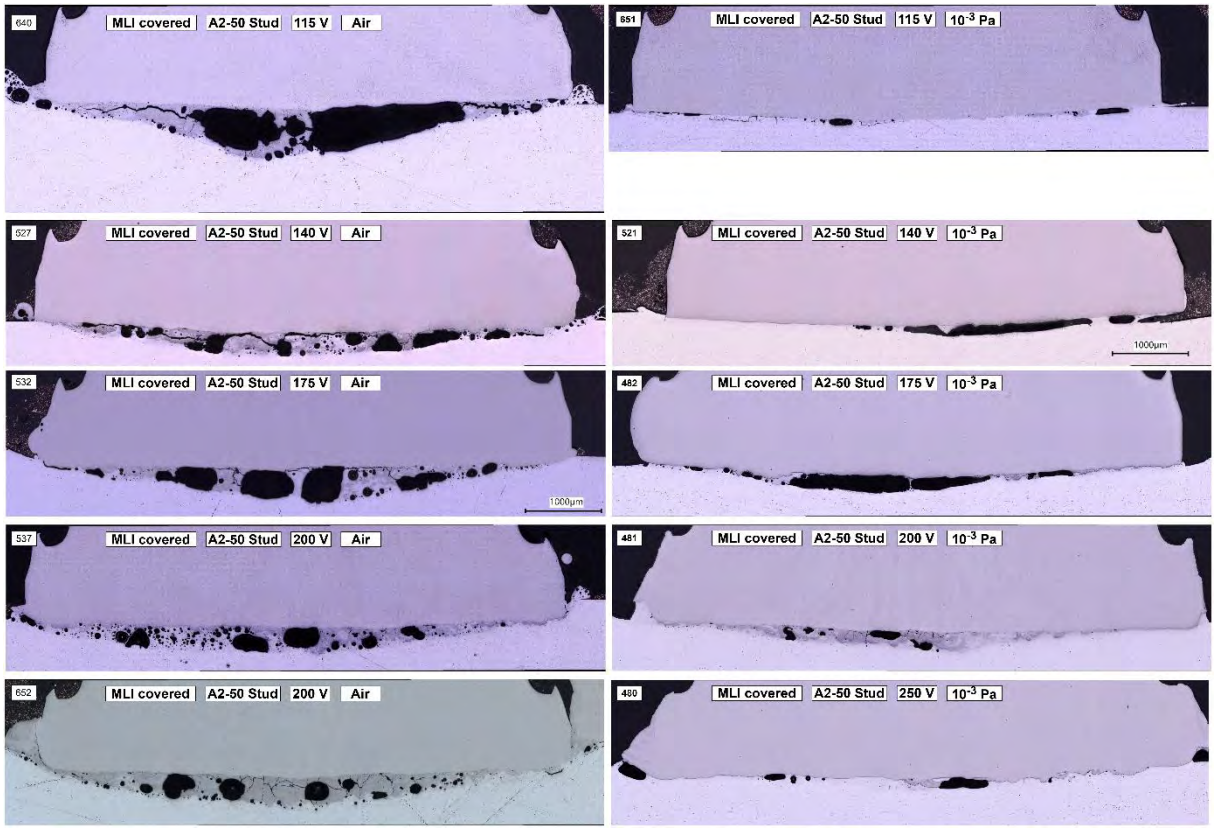

Figure 4.2. *Cross-sectional optical micrographs of CCDS joints produced using A2-50 steel studs on MLI-covered aluminium substrates under atmospheric conditions (left) and under vacuum (≈10^{-3} Pa, right), for discharge voltages ranging from 115 V to 250 V. Joints produced in air exhibit extensive porosity, discontinuous fusion zones, and irregular interfacial morphology, whereas joints produced under vacuum show a more continuous fusion interface with reduced porosity and improved metallurgical cohesion across the investigated voltage range.*

Out of 48 predefined process states for non-impact welding scenario, **46 states (96%) were already successfully tested**, providing a near-complete mapping of the intended parameter space. The results demonstrate that CCDS welding under vacuum conditions is not only feasible but, in many cases, exhibits a broader and more stable process window than under atmospheric conditions. In particular, A2-50 steel studs showed robust weldability across multiple surface conditions, including non-conductive layers, when appropriate stud geometry and voltage ranges were applied.

4.3. Electro-Mechanical Process Signatures of High-Quality Joints

To move beyond binary weldability assessment, IMSAS established characteristic electro-mechanical process signatures associated with high-quality CCDS joints. Synchronized measurements of force, current, voltage, and instant power enabled the identification of distinct process phases during joining.

A typical high-quality joint exhibits:

- an initial phase characterized by stable electrical contact and gradual tip softening,
- a contact closure event marked by a transient force peak and voltage collapse,
- a short rebound phase without loss of electrical continuity,
- a thermo-mechanical phase with sustained current flow and decreasing instant power,
- and a controlled cooling phase under maintained mechanical preload.

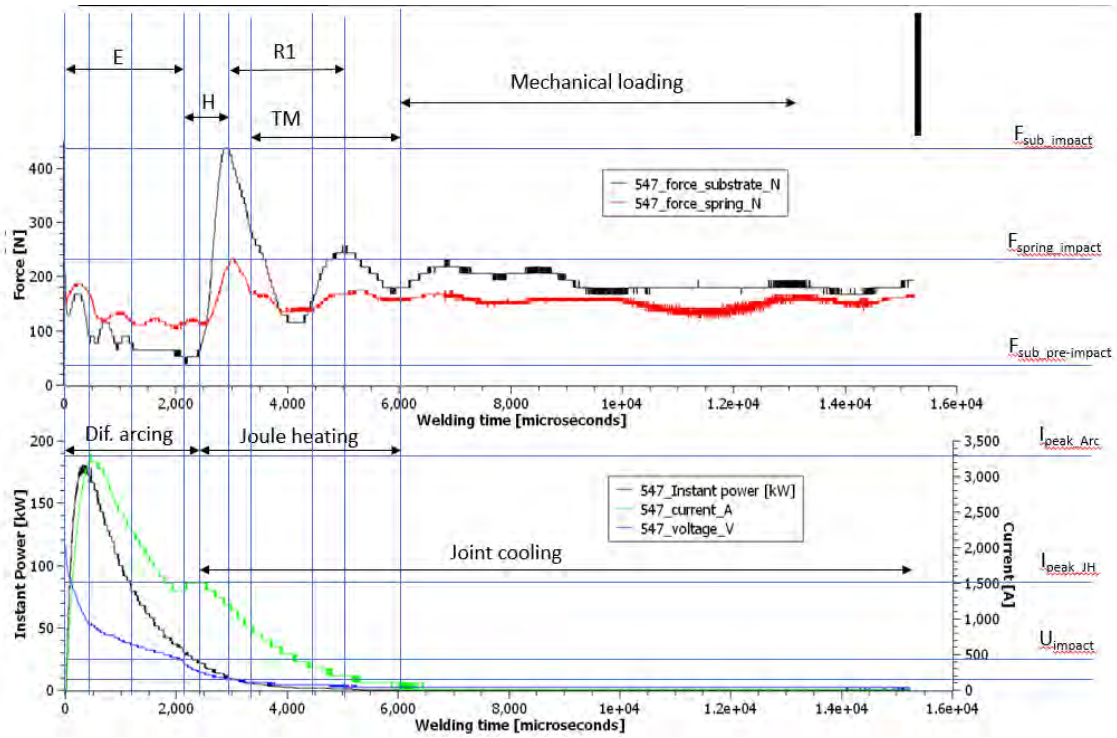

Figure 4.3. *Representative electro-mechanical process signature of a high-quality CCDS joint (non-impact welding scenario). The upper plot shows the evolution of forces acting on the substrate and spring during welding, while the lower plot presents the corresponding current, voltage, and instant power. Distinct process phases are identified, including initial contact and tip softening (E), head contact (H), first rebound (R1), thermo-mechanical interaction (TM), and subsequent mechanical loading and joint cooling. The stable coupling between electrical energy input and mechanical response is characteristic of successful joints formed under vacuum conditions.*

The repeatability of this coupled electro-mechanical signature across successful welds confirms that CCDS joining under vacuum conditions is governed by controlled thermo-mechanical interactions rather than stochastic arc behaviour. These signatures provide a physically meaningful basis for process monitoring, quality assessment, and future automation.

4.4. Mechanical Performance under Vacuum and Atmospheric Conditions

The mechanical relevance of CCDS joints was evaluated through tensile testing. A pronounced dependence of joint strength on environmental conditions was observed. For A2-50 steel studs welded to AA6061-T6 substrates, joints produced under vacuum conditions achieved ultimate tensile strengths in the range of approximately **30–50 MPa**, whereas joints produced under atmospheric conditions remained significantly weaker, typically below **25 MPa**.

The tensile strength exhibited a non-monotonic dependence on discharge voltage, with an optimal voltage window identified around **115–140 V** under vacuum conditions. At lower voltages, insufficient interfacial plasticization limited joint strength, while at higher voltages excessive melting and material redistribution reduced the effective load-bearing cross-section.

Welding through representative spacecraft insulation materials was further investigated using MLI. Under vacuum conditions, mechanically stable joints with tensile strengths up to approximately **45 MPa** were achieved. In contrast, specimens produced under atmospheric conditions were mechanically unstable and often detachable by hand, exhibiting tensile strengths below **5 MPa**. These results demonstrate that CCDS welding through non-conductive surface layers is feasible only under vacuum conditions and can yield structurally meaningful joints when appropriate parameters are applied.

A particularly important outcome of the mechanical testing concerns the combined effect of environment and surface condition on joint strength. For anodized aluminium surfaces welded using A2-50 steel studs, joints produced under atmospheric conditions at high discharge voltage (500 V) achieved an ultimate tensile strength of only **16.5 ± 4.2 MPa**. Performing the same joining operation under vacuum increased the strength to **28.8 ± 5.3 MPa**, confirming the beneficial role of vacuum conditions alone.

However, when the anodized surface was locally laser-ablated prior to welding under vacuum, the required discharge voltage could be reduced to **140 V**, while the resulting joint strength increased markedly to **40.7 ± 7.6 MPa**. This strength level is comparable to that obtained on clean, non-anodized aluminium surfaces welded under identical conditions (**44.1 ± 17.2 MPa at 140 V**).

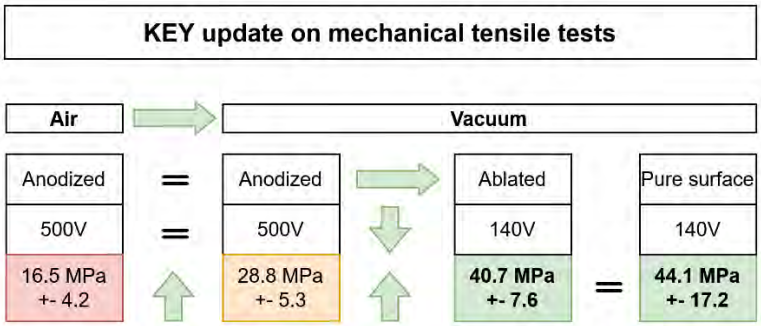

Figure 4.4. *Effect of environment and surface condition on CCDS joint strength, showing the transition from atmospheric to vacuum welding and the impact of local oxide removal on anodized surfaces.*

These results demonstrate that the dominant limitation in CCDS welding on anodized surfaces is not the vacuum environment itself, but the presence of the oxide layer. Once this layer is locally removed, CCDS welding under vacuum converges toward the mechanical performance of joints produced on clean metallic substrates, while operating at significantly lower energy levels. This knowledge turned our attention to laser ablation as one of the critical subsystem of the technology in the next development.

4.5 Summary of CCDS Research Outcomes (2024–2025)

During the 2024–2025 reporting period, IMSAS finalized the experimental validation of Contact Capacitor Discharge Stud (CCDS) welding within the ESA PECS framework. A dedicated laboratory infrastructure was established, combining a modular capacitor discharge welding system with an upgraded vacuum chamber capable of reaching pressures on the order of 10^{-3} Pa, together with synchronized electrical and mechanical diagnostics.

A systematic weldability campaign was conducted for non-impact welding without electrical breakdown (Scenario C), achieving near-complete coverage of the predefined parameter space. The results demonstrate that CCDS welding under vacuum is a stable and reproducible process across a wide range of surface conditions, including bare aluminium, anodized layers, painted coatings, Kapton tape, and multi-layer insulation (MLI), with broader operational windows than under atmospheric conditions.

Electro-mechanical process signatures derived from force, current, voltage, and power measurements revealed repeatable phase behaviour characteristic of high-quality joints, confirming that the joining process is governed by controlled thermo-mechanical interaction rather than stochastic arc phenomena. Mechanical testing showed that joints produced under vacuum exhibit significantly higher tensile strength than those produced in air, reaching approximately 30–50 MPa for A2-50 steel studs on AA6061-T6 substrates. A key result demonstrated that appropriate surface preparation enables joint strengths comparable to clean metallic surfaces while operating at substantially reduced discharge voltage.

In parallel, IMSAS was successful in a national space programme call and is now **contracted to develop a large-scale vacuum chamber equipped with a robotic arm and an instrumented measurement plate.** This new infrastructure will enable the transition from component-level experiments toward a robotic CCDS simulator, supporting further advancement of the technology toward higher technology readiness levels.

5. REMOTE SENSING

I. Barka, K. Buchová, J. Černecký, Z. Číčová, J. Feranec, Z. Fulmeková, M. Gallay, T. Goga, Ľ. Halada, A. Halabuk, J. Hofierka, P. Kenderessy, M. Kopecká, S. Košánová, K. Merganičová, K. Onačillová, Š. Opravil, R. Pazúr, M. Rusnák, I. Sačkov, M. Sedliak, † M. Sviček, D. Szatmári, J. Tomes, A. Zverková

Selected activities of five institutions are included in this report:

Institute of Geography, Slovak Academy of Sciences in Bratislava

Destructed grassland identified using the PlanetScope satellite images

Completion of the ESA RPA project solution: *Land Cover Change Monitoring for Identification of Potential Illegal Activities in Slovakia (LAPIA)*, No. 4000141176/23/NL/SC/rp (2023-2024): Institute of Geography, Slovak Academy of Sciences, Bratislava (prime contractor); National Agricultural and Food Centre, Soil Science and Conservation Research Institute, Bratislava; Slovak University of Technology, Faculty of Civil Engineering, Department of Theoretical Geodesy and Geoinformatics, Bratislava (subcontractors).

One of the results achieved by solution this project outlines a methodology for detecting potential illegal environmental activities in Slovakia using Earth observation data, focusing on the destruction of protected grasslands and non-forest woody vegetation, ecosystems essential for climate resilience. Experimental areas were selected based on illegal activities identified by

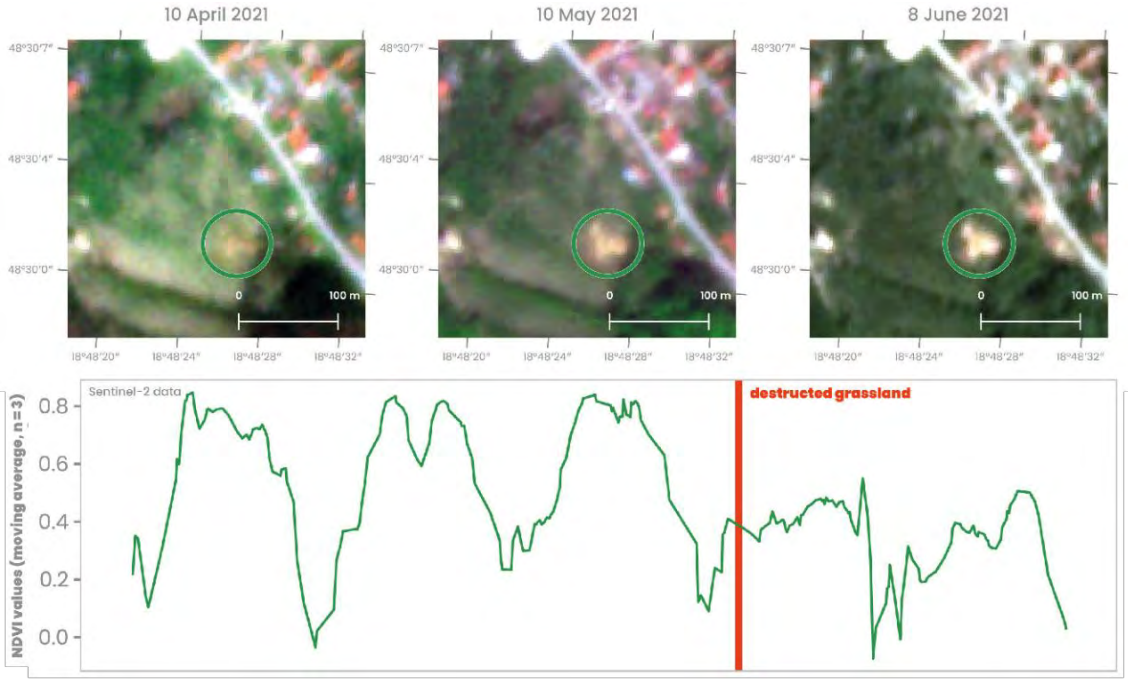

Figure 5.1. *Example of illegal activity recorded by the Slovak Environmental Inspectorate: destructed grassland identified using the PlanetScope satellite images with corresponding Sentinel-2 NDVI profile.*

the Slovak Environmental Inspectorate between 2017 and 2022. A custom web application, developed in the Google Earth Engine environment, was utilised for visualisation and verification, integrating the Normalised Difference Vegetation Index and the Bare Soil Index generated from the Sentinel-2 satellite imagery. The cutting of non-forest woody vegetation was identified using NDVI anomalies, which indicated disruptions in vegetation phenology. At the same time, lower NDVI values and changes in surface reflectance detected the destruction of grasslands. The results highlight the usefulness of optical remote sensing data for detecting landscape transformations. However, challenges remain in distinguishing between legal and illegal activities and their representation through maps and infographics (Goga et al., 2025).

Multi-sensor and machine-learning-based assessment of ecological and riparian land-cover changes in Slovak watercourses.

Result was achieved within the framework of the Slovak Research and Development Agency (SRDA/APVV) project 23-0265 solution: ***3D technology and machine learning methods for remote environmental monitoring and assessment of river health***.

The research aims to assess the trend in the development of Slovak watercourses in the context of a changing climate and the intensive influence of direct human interventions. The first part of the research was devoted to the incision of the Bela River channel, where the original multi-channel system is changing into a simple river system (Rusnák et al. 2024, 2025). Modern 3D technologies offer new opportunities to analyse and assess parameters that were previously difficult to obtain or could not be identified with sufficient accuracy. Degradation of the Bela River in the Western Carpathians has been monitored since 1949 using lidar data

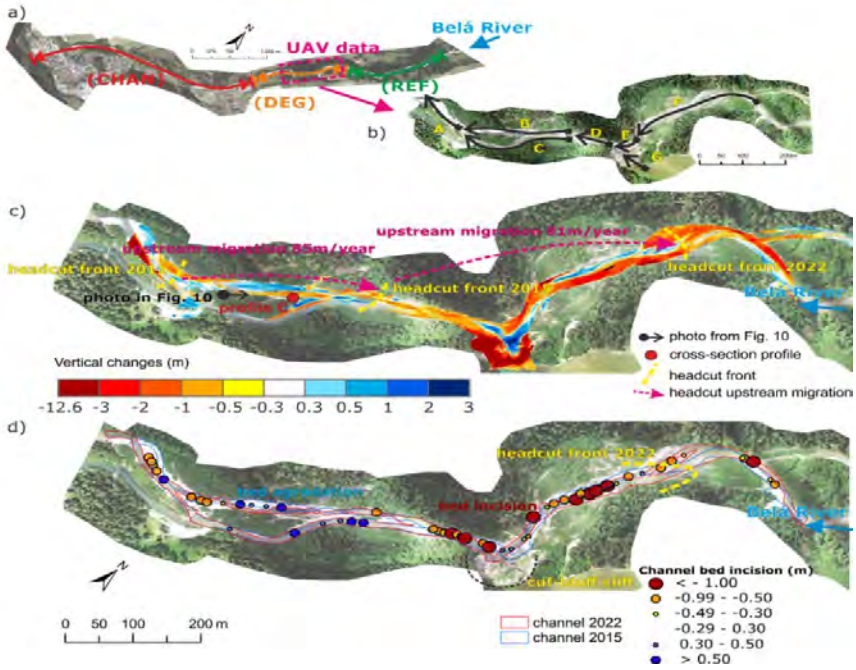

Figure 5.2. *Channel incision of the former braided and multi-channel wandering river system is transforming into a single-thread channel. Paper Rusnák et al. (2024) answers questions about the natural channel transformation of the Belá River in Slovakia. Evaluate long-term channel pattern alterations using an innovative approach by a combination of aerial images, LiDAR data and drone mapping. The results quantify channel incision in some sections up to 4 m from 1949. Drone survey confirms erosion of 22,759 m^3 of sediment between 2015 and 2022, equivalent to roughly 3832 trucks.*

analysis, historical aerial imagery and UAV data. The model analyses indicate a maximum channel deepening of up to 4 m, at a rate of 5.7 cm/yr, in the most degraded reach. Overall, volumetric changes from the drone survey indicated the entrainment of 22,759 m^3 of gravel sediments between 2015 and 2022 and a total erosion of 573,303 m^3 from the analysis of historical data between 1949 and 2020.

High-resolution 3D data are later compared with satellite data for long-term river monitoring of the Belá and Danube River (Afzali et al. 2025, Afzali and Rusnák, 2026). Historical aerial photographs are well-known as a reliable source of information on historical land cover and land use. However, extracting this information can be challenging due to the limited spectral characteristics in black-and-white images. The textural-based approach using Machine Learning (ML) models enables the detection of the spatial pattern of the braided-wandering multichannel system from historical aerial images, with an emphasis on riparian vegetation. Despite limitations, the proposed approach addresses key challenges in extracting information from historical orthophotos and can be extended to broader ecological and environmental applications. Monitoring riparian vegetation using a multi-sensor approach (Landsat-5/8 and Sentinel-2) enabled evaluation of ecological processes, spatial errors, misclassification, and the spatial distribution of LC changes within the riparian zone.

Mapping of land use intensity pattern in agricultural landscapes – dissertation focused on the use of Sentinel satellite data

The dissertation of Mgr. Šimon Opravil completed in 2025 focused on mapping the intensity of grassland use in agricultural landscape using remote sensing data. The research compares two major mountain regions of Europe, the Alps and the Carpathians, which are characterized by different trajectories of agricultural development. In the first stage, the author increased the accuracy of grassland identification through the consensual integration of multiple land cover datasets derived from Sentinel data. In the second stage, he focused on the detection of mowing as an indicator of management intensity using satellite time series data analysis. The result is a spatially transferable methodological framework applicable in the assessment of grassland management and the support of agro-environmental policies.

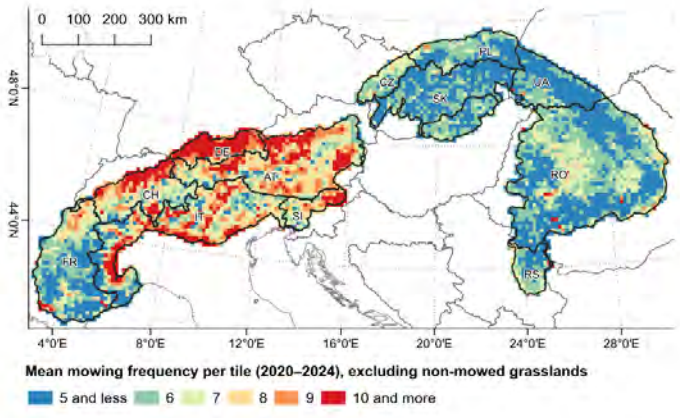

Figure 5.3. *Mean mowing frequency at 10 km grid, calculated only for grasslands mown at least once during 2020-2024 period.*

Project: ***G4B – Grasslands for biodiversity: supporting the protection of biodiversity-rich grasslands and related management practices in the Alps and Carpathians*** (part of the Biodiversa+ project)

Within our G4B project we developed a geospatial dataset of grassland habitats for the European Alps and Carpathian mountain ranges, two of the continent's most significant biodiversity hotspots. The classification framework is based on the European Nature Information System (EUNIS) Habitat Classification, consistent with European-wide monitoring and conservation standards. The model outputs were generated at two hierarchical levels of the EUNIS classification and identified the temperate, alpine, and subalpine grassland types with a high accuracy of accuracy. The outcomes provide a baseline for further research, conservation planning, and ecosystem management

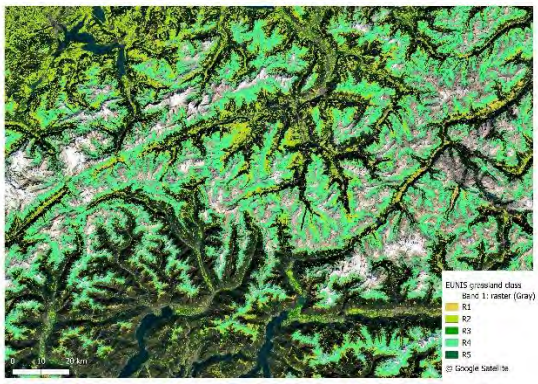

Figure 5.4*. Illustration of the results of mapping the habitat structures. The categories are as follows: R1 Dry grasslands, R2 Mesic grasslands, R3 Seasonally wet and wet grasslands, R4 Alpine and subalpine grasslands, R5 Woodland fringes and clearings and tall forb stands.*

Institute of Landscape Ecology, Slovak Academy of Sciences (ILE SAS)

Within the reporting period 2024–2025, the main EO-related activities at ILE SAS focused on advancing Copernicus/ESA mission readiness through (i) development of hybrid retrieval workflows for next-generation hyperspectral products, (ii) large-area monitoring of agricultural production potential and yield stability from Copernicus Sentinel-2 time series, and (iii) strengthening Cal/Val-oriented technical infrastructure for biophysical and structural product validation.

1. ESA project completed in 2025: ***CHIME_NPV – feasibility study towards quantitative NPV products for Copernicus CHIME***

In 2024–2025, ILE SAS successfully finalised the ESA-funded CHIME_NPV feasibility study, delivering an end-to-end concept for quantitative retrieval of non-photosynthetic vegetation (NPV) variables from upcoming Copernicus hyperspectral mission (CHIME). The project directly supports the planned Copernicus hyperspectral mission CHIME by developing the methodological and validation foundations for an operational Level-3 NPV quantification product (with an emphasis on quantitative variables rather than only fractions/classes). The work explicitly targets the identified gap between widely used fractional/area-based NPV indicators and physically meaningful quantities (e.g., NPV biomass, crop residue biomass, brown LAI), which remain underrepresented mainly due to reference-data scarcity and transferability limitations.

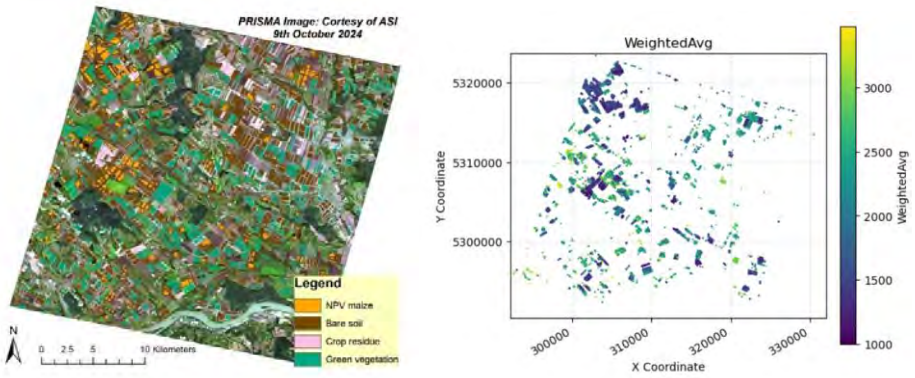

Figure 5.5. *Left: Example of Baseline Classification Map. Right: Ensemble-based NPV biomass prediction (g.m^2).*

Core technical outcome is a hybrid workflow that links (i) structured field spectroscopy + biomass sampling campaigns across diverse agricultural NPV forms, (ii) 3D RTM-based synthetic data generation (DART LUTs and inference), (iii) feature-level unsupervised domain adaptation using an MMD-minimising neural network, (iv) multi-model biomass regression (Fig. 5.5), and (v) distribution-based plausibility validation. The study also provided evidence that such a combined physics–ML–DA approach can overcome key obstacles that historically prevented robust and transferable NPV biomass models.

Project results and follow-up recommendations were presented to the CHIME Mission Advisory Board (July 2025), supporting alignment of the proposed retrieval and validation strategy with CHIME product priorities (including Level-3 NPV quantification). Based on recent consultations with ESA, follow-up activities will aim to progress the workflow toward higher TRL. In particular, fire-risk management, e.g. implementing the hybrid approach in areas where NPV is a key indicator of fuel load and fire risk, while maintaining robustness under limited ground truth and domain shifts.

A critical technical bottleneck for hyperspectral algorithm development and Cal/Val is the limited availability of airborne/UAS hyperspectral platforms. In 2024, this limitation was strategically mitigated by initiating a partnership with VUJE, enabling helicopter-based acquisitions with the HySpex sensor infrastructure. This creates a practical bridge between plot-scale reference data and satellite products, strengthening future CHIME-oriented validation and application transfer.

2. *Continued Copernicus Sentinel-2 work (2018–2024): crop production potential and yield-stability patterns over a large agricultural region*

In 2024–2025, we continued the evaluation of production potential and long-term stability over a large agricultural region using dense Copernicus Sentinel-2 time series, culminating in a 7-year assessment (2018–2024) of stable yield productivity zones (sYPZ) and unstable zones at 10 m resolution. The analysis covered approximately 35,000 crop fields, highlighting that unstable zones dominated (47% of cropland), while stable classes were partitioned into medium (36.3%), low (10.2%) and high (6.5%) sYPZ; high sYPZ accounted for roughly 170 km².

The study demonstrates that multi-year Sentinel-2 trajectories can be used to derive robust, comparable stability patterns at sub-field scale and to separate persistent productivity signals from year-to-year variability. Spatial aggregation revealed broader gradients (e.g., high sYPZ

more concentrated in the north, low sYPZ more prevalent in the south), supporting interpretation across both local and regional drivers (Fig. 5.6).

The resulting stability layers provide an actionable baseline for (i) stratified within-field management and targeted interventions (precision agriculture), (ii) prioritisation of monitoring and advisory services, (iii) risk-aware planning (e.g., identifying persistently low/unstable zones), and (iv) integration with follow-up yield estimation workflows (including late-season, pre-harvest applications in cereals). The work also supports Copernicus downstream use by translating freely available EO time series into management-ready stability products.

To support interpretation and improve transferability, the accompanying paper (Košánová et al., 2025) applied an XGBoost classifier with SHAP diagnostics to explain sYPZ patterns using environmental and management proxies (topography, wetness, climate/soil classes, and soil spectral properties derived from a Sentinel-2 bare-soil mosaic). The SHAP results suggest non-linear effects of elevation and slope, and highlight a strong influence of SWIR2 (Sentinel-2 band B12) bare-soil reflectance. These findings motivate follow-up work with a stronger emphasis on causal links, particularly soil spectroscopy and soil health drivers underpinning long-term yield stability.

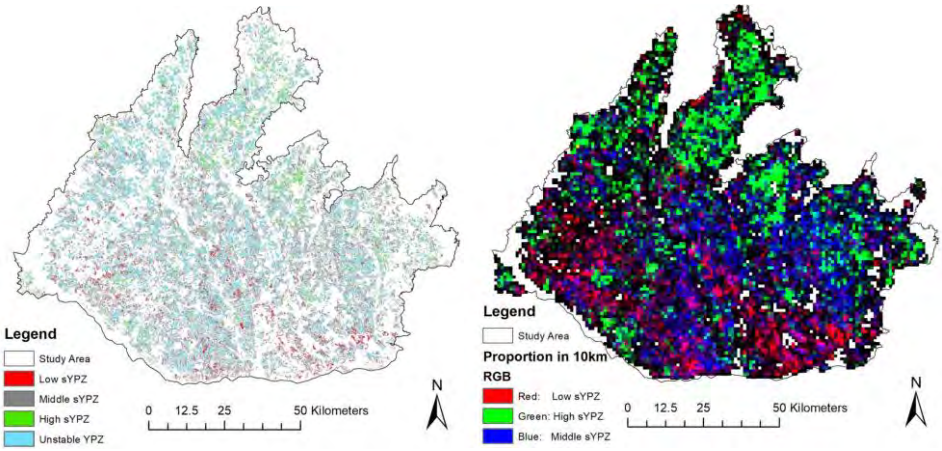

Figure 5.6. *Left: Distribution of low, and high yield sYPZ and unstable YPZ at 10 m spatial resolution. Right: Low, and high sYPZ. Proportion within a 10 km window of respective stability classes constitutes RGB composite.*

3. Building technical and infrastructural background for Cal/Val initiatives linked to new EO missions (CHIME, FLEX)

During 2024–2025, ILE SAS systematically strengthened its technical and measurement infrastructure to support calibration/validation (Cal/Val) activities for upcoming and new-generation Earth observation missions, with main focus on hyperspectral and fluorescence-based products and their downstream Level-2/Level-3 biophysical retrievals. This capacity building is directly aligned with the increasing demand for robust, metrologically sound Cal/Val protocols and interoperable validation practices for optical land-imaging and advanced vegetation products.

The activity was motivated by mission-driven product needs across (i) Copernicus CHIME hyperspectral observations (VIS–SWIR, 400–2500 nm; 30 m class products and broad land applications), which requires pre-launch algorithm readiness and traceable validation datasets, ii) ESA FLEX fluorescence observations and derived vegetation functioning variables (e.g., fluorescence-related quantities and photosynthesis proxies), and (iii) ESA Biomass, targeting

Figure 5.7. *Field Cal/Val infrastructure supporting ESA FLEX mission at VÚRV Piešťany. Left: Flux tower (LI-Cor Env.) with FLOX box (JB Hyperspectral) continuous measurements. Right: Mobile FLOX box for ambient SIF measurements.*

(global maps of above-ground biomass, forest height and disturbances and requiring extensive Cal/Val reference capacity and cross-sensor consistency. In this context, ESA's FLEX Cal/Val Announcement of Opportunity provided an additional framework for positioning ILE SAS infrastructure and protocols within a broader European Cal/Val ecosystem.

A core technical step in 2024–2025 was the integration and harmonisation of field optical, physiological, and flux measurements around the ILE SAS eddy-covariance site and associated experimental plots (VÚRV Piešťany/Borovce region). The infrastructure is designed to support both (a) validation of lower-level products (spectral reflectance; SIF-related observables) and (b) calibration and parameterisation of process- and radiative-transfer models used to generate higher-level biochemical/structural variables. In practice, this included dual field spectroscopy capability (fixed tower-based FLOX plus mobile FLOX box, Fig. 5.7), FieldSpec4 with integrating sphere support, canopy structural sampling (SunScan/LAI-related measurements), thermal sensing, leaf gas-exchange (LI-COR 6800), PAM-based fluorescence measurements and pigment analytics as complementary constraints for model parameterisation and uncertainty reduction.

In parallel, structural measurement capacity relevant to both Cal/Val and RTM parameterisation through mobile LiDAR scanning (Lixel 2 Pro, XGrids) and SLAM algorithm processor supporting structural priors and scene realism (Fig. 5.8) for radiative transfer modelling (e.g., 3D RTMs), improve interpretability of hyperspectral retrievals under canopy-

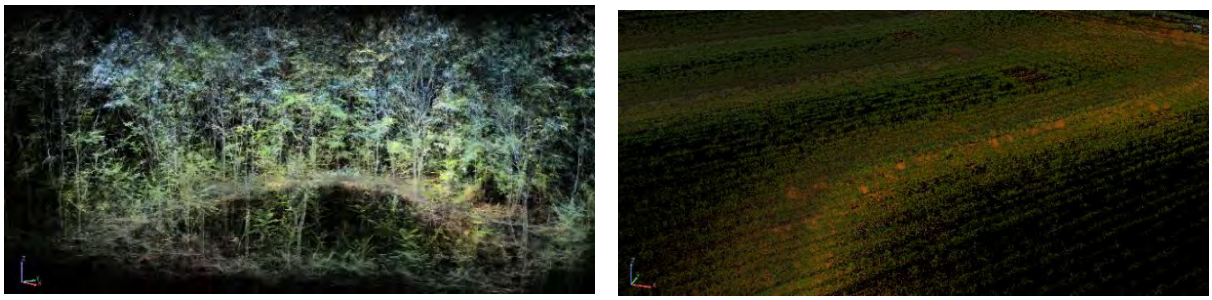

Figure 5.8. *Left: Mobile LiDAR (Lixel 2 Pro) acquisition over a forest stand (Bábsky les): field campaign for multi-sensor synergy product development. Right: Weed affected maize parcelt (VÚRV Borovce): canopy height and weed volume representation for 3D RTM model parameterisation.*

structure variability, and create a pathway to multi-sensor synergy (structure + optics) that is relevant across CHIME vegetation products and Biomass-linked structural variables.

Institute of Geography, Faculty of Science, Pavol Jozef Šafárik University in Košice

Project: ***URBANA: Development and Verification of Urban Analytics*** *(Contract No.: AO/1-11889/23/I-DT)*

The URBANA (URBan ANAlytics) project is an ESA-funded initiative led by GMATICS, focused on the development of innovative analytical tools to support urban planning and the assessment of urban environmental parameters and their impacts on people and infrastructure. The project responds to the growing need to integrate satellite and spatial data into public administration processes, with the aim of strengthening analytical capacities and supporting informed decision-making in urban environments. Developed and tested in collaboration with the cities of Rome, Milan, Pesaro, Zurich, Barcelona, Hamburg, Bratislava, and Košice, URBANA promotes the use of Earth observation data for building more sustainable, resilient, and responsive cities.

Our task within the URBANA project was the development and testing of the B.3 – Thermal Stress Assessment service, focused on producing high-resolution urban heat stress maps through the integration of satellite imagery, vector data, LiDAR point clouds, population grids, and meteorological (SYNOP) forcing data. Using advanced preprocessing workflows and ENVI-met modelling, we derived key thermal stress indices (PET, SET, UTCI, Fig. 5.9), which were subsequently analysed in relation to the spatial distribution of urban populations. The objective was to support evidence-based urban adaptation and mitigation planning by providing scalable, transferable methodologies applicable to different cities with available data, with pilot implementations carried out for the municipalities of Bratislava and Košice.

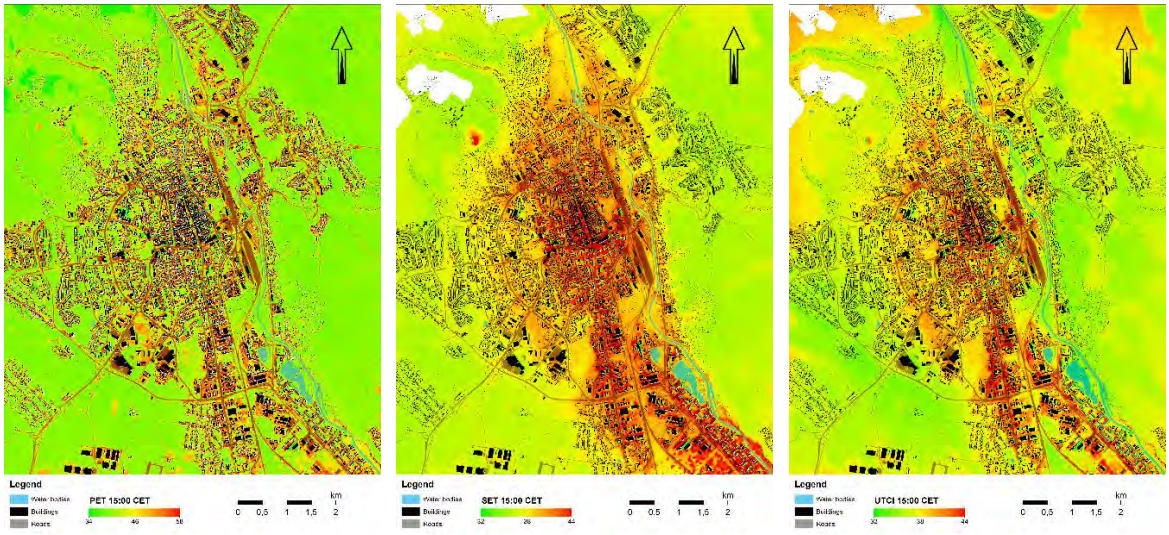

Figure 5.9. *Thermal indices PET, SET and UTCI at 15:00 CET at pedestrian height (1.5 m) in Košice.*

Project: ***VEGA No. 1/0780/24 (2024–2026) Integration of LiDAR and Hyperspectral Data with Machine Learning Methods for Improved Land Cover Classification***

The project is funded by the Slovak Scientific Grant Agency **VEGA No. 1/0780/24 (2024–2026)** and is carried out at the Institute of Geography, Faculty of Science, Pavol Jozef Šafárik University in Košice. It focuses on integrating airborne and UAV-based **LiDAR point clouds** with **hyperspectral imagery** and **machine learning** to improve land-cover classification and 3D landscape characterization. The research develops transferable spectral-structural workflows combining LiDAR-derived metrics (e.g., CHM, vegetation volume, surface morphology) with VNIR–SWIR features, emphasizing feature fusion, dimensionality reduction (e.g., PCA), supervised classification, and independent validation. Applications include urban vegetation assessment, precision viticulture, and CAL/VAL support for hyperspectral satellite missions. A key output concerning urban environment is **Svetozarov & Gallay (2024)** (*Geografický časopis*, 76(3), 221-247, https://doi.org/10.31577/geogrcas.2024.76.3.12), which quantified **31.12 million m³** of urban vegetation in Košice from airborne laser scanning and showed that 3D volumetric indicators substantially refine green infrastructure assessment compared to 2D metrics. The project also contributes to hyperspectral CAL/VAL research. **Melis et al. (2024)** (*ISPRS Archives*, XLVIII-3-2024, 337–343; https://doi.org/10.5194/isprs-archives-XLVIII-3-2024-337-2024) reported first spectral and LiDAR results for **Sal'e Porcus** (Sardinia, ~3.3 km²), including an initial evaporite spectral library, cross-scale consistency between field/UAV/satellite data (PRISMA, EnMAP), and LiDAR-based morphology patterns, supporting the site as a candidate European CAL/VAL area for current and forthcoming hyperspectral missions (e.g., PRISMA-SG, CHIME). The project team presented **at WHISPERS 2025 conference in Barcelona two contributions** on (i) hyperspectral–LiDAR integration for improved discrimination/classification of vineyards and (ii) UAV hyperspectral bridging ground and satellite measurements for CAL/VAL at Sal 'e Porcus. The project enters its **final year in 2026 (**https://www.ieee-whispers.com/wp-content/uploads/2025/11/Whispers_Program_2025_final.pdf**)**.

Events*:* ***International Remote Sensing Summer School, Experiencing Remote Sensing on Sardinia inland site: Advanced summer school on instruments and methodology for a CAL/VAL site for Optical data,*** 21-25 July, 2025, San Vero Milis, Italy

Three academic staff members of the Institute of Geography, Faculty of Science, Pavol Jozef Šafárik University in Košice actively participated in the fourth edition of this summer school, held from 21 to 25 July 2025 in western Sardinia near the village of San Vero Milis **as part of research and capacity-building activities linked to the VEGA project No. 1/0780/24.** Hands-on training research and educational activities were focused on the seasonally drying salt lake Stagno di Sal'e Porcus, which – due to its geological specificity and exceptional spectral stability – is emerging as a potential European calibration and validation site for hyperspectral satellite sensors. During the summer school, they demonstrated and taught laser scanning and hyperspectral mapping using unpiloted aerial systems (UAS). The training aimed at the mutual sharing of knowledge and skills in the processing of hyperspectral and lidar data from ground, aerial, and satellite measurements for the purposes of calibration and validation of hyperspectral satellite data.

The event was co-organized by the Department of Chemical and Geological Sciences of the University of Cagliari in cooperation with the Italian National Institute of Geophysics and Volcanology (INGV), the Italian Association for Remote Sensing of the Earth (AIT) and the Italian Space Agency (ASI). Over five intensive days, 30 doctoral students from around the globe took part in demanding fieldwork and data acquisition, generating more than 300 GB of geospatial data. The summer school provided advanced practical experience in EO-based

environmental monitoring and demonstrated the value of international collaboration for research training and methodological harmonization – outcomes that directly reinforce the VEGA project's research objectives and dissemination/education activities.

Figure 5.10. *Field data collection at the seasonally drying salt lake Stagno di Sal'e Porcus, Sardinia. Participants conducted laser scanning and hyperspectral mapping using UAS for calibration and validation of hyperspectral satellite data.*

National Forest Centre Zvolen

Remote Sensing activities of the National Forest Centre in Zvolen were aimed at two basic topics:

- Satellite-based observation of forest ecosystem's response to global environmental changes.
- Research of the applications of airborne laser scanner technology in the forest management

1) *Satellite-based observation of forest decline – STALES web service*

The operational activities are ongoing in a continuous manner. Recently, satellite data and layers of forest damage classification from both 2024 and 2025 have been integrated into the STALES web service, accessible at https://www.nlcsk.org/stales/. This system is designed to provide timely information to forest owners and the forest state administration, offering insights into the current condition of forest stands and any observable changes.

To establish a comprehensive historical perspective, individual satellite images spanning from 1990, 1996, 1998, 2000, 2003, and 2006-2025 have been meticulously combined into a nationwide mosaic. This mosaic serves as the foundation for assessing forest damage throughout these years. The services primarily utilize Landsat satellite images with a spatial resolution of 30 × 30 meters and Sentinel data with a resolution of 10 × 10 meters since 2016. Mosaics are crafted by blending Landsat (Sentinel) bands in false colours, specifically Near-infrared, Mid-infrared, and Red bands.

Mapping applications have been developed to showcase forest district boundaries at a scale of 1:100,000 and forest compartment boundaries at a scale of 1:20,000 and larger. The STALES service encompasses four distinct map applications:

Map Applic. 1 – facilitating the comparison of satellite scenes from two different periods (Fig. 5.11).

Map Applic. 2 – providing dynamic visualization of both current and historical satellite scenes.

Map Applic. 3 – presenting dynamic visualization of forest health condition (Fig. 5.12).

2) Identification of clear-cuts and damaged forest stands based on remote sensing data as a support for forest restoration.

Remote sensing products were used in the framework of research aimed at revitalisation of forest stands after bark beetle outbreak and restoration of ecosystem functions. Following an intensive summer drought in 2022, a bark beetle outbreak began in commercial Norway spruce forests in central part of Slovakia. In order to monitor development and to evaluate expected effects of this disturbance on forest ecosystems, remote sensing (RS) products have been utilised on an area of 21,900 ha. Using Sentinel 2 and Landsat scenes, combined with terrestrial data, we developed time series of spatial layers with affected forest stands. A normalized difference water index (NDWI, Gao 1996), combined with field observations, were the main RS-based features in the identification of bark beetle outbreak. Each layer in the time series identified newly affected forest stands (Fig. 5.11). This time series (evaluated period was 2021-2025), with an employment of forestry data sources, allowed us to estimate a loss of growing stocks as well as carbon stocks in living biomass due to the selective logging. Produced outputs were successfully utilised for the preparation of the strategy of forest revitalisation in affected area.

Figure 5.11. *An example of the identified newly damaged (in 2024) forest stand from the satellite scene (left), clear-cut in 2025 (middle) and comparison with aerial scene from 2025 (right).*

3) Quantification of aboveground shrub biomass on abandoned agricultural land in Slovakia using RS data

Abandonment of agricultural land is a pan-European problem, which is reaching a high intensity in Slovakia. The gradual overgrowth of abandoned land with woody species has several causes and consequences for the landscape and human society. The aim of the research was to create a raster layer of shrub vegetation on abandoned agricultural land in Slovakia based on remote sensing data and nationwide spatial data and subsequently determine the amount of

biomass stored in it. According to the cadastral data, the Land Parcel Identification System (LPIS) and the airborne laser scanning products, shrub vegetation on potentially abandoned agricultural land was mapped. Quantification of biomass was based on the height and density of bush vegetation, derived from airborne LiDAR data. Results were further filtered using Sentinel 2 satellite scenes and derived NDVI layer. Based on the resulting raster layer with 10 m spatial resolution (Fig. 5.12), the area of shrub vegetation on agricultural land (registered in the cadastre as arable land, permanent grassland, vineyards, orchards or hop fields) outside the LPIS system is 44,862 ha (Barka 2025). The amount of above-ground biomass represents a total of 1.843 mil. tons of dry mass, on average 41.07 tons/ha. In the absence of further management of these areas, it can be expected that these shrubs will gradually turn into forests. The results confirm the need to deal with woody species on non-forest land and thus carry out land parcel consolidation.

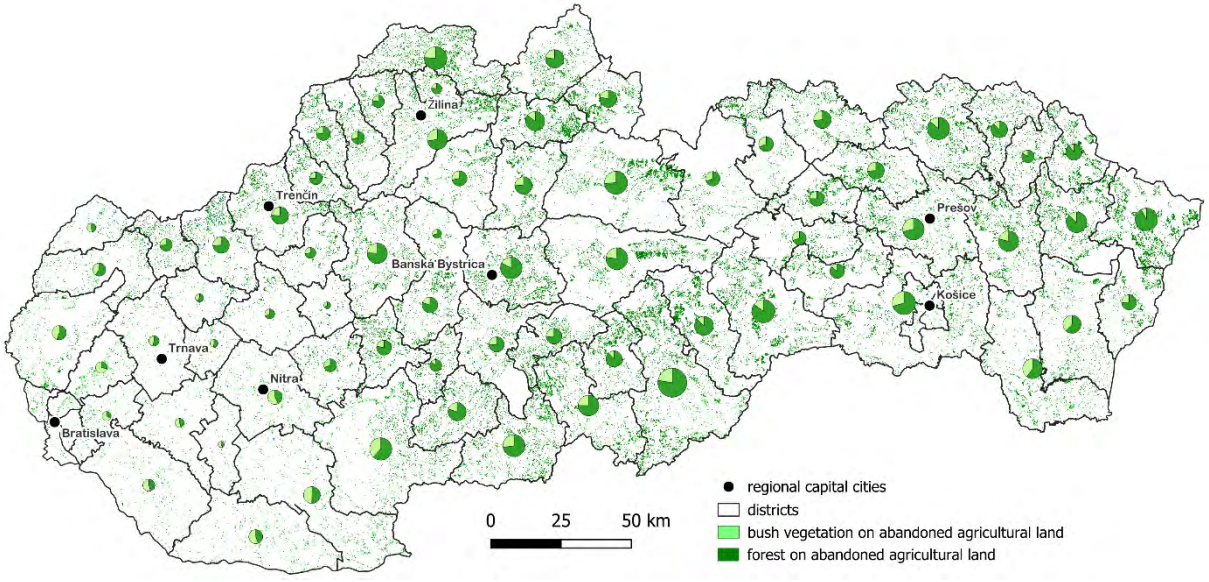

Figure 5.12. *Woody species on abandoned agricultural land outside of LPIS system in 2020. Pie charts show area (389 – 18,850 ha) and the share of forests and bush vegetation.*

4) Airborne LiDAR-based assessment of elevation accuracy of forest road maps

Forest road maps are a fundamental source of information for the sustainable management, protection, and public utilization of forests. However, the precision of these maps is crucial to their use.

In this context, we assessed and compared the elevation accuracy of terrain on three forest road surfaces (i.e., asphalt, concrete, and stone), which were derived based on data from three remote sensing technologies (i.e., aerial imaging, airborne laser scanning, and mobile laser scanning) using five geospatial techniques (i.e., inverse distance; natural neighbour; and conversion by average, maximal, and minimal elevation value). Specifically, the elevation accuracy was assessed based on 700 points at which elevation was measured in the field, and these elevations were extracted from fifteen derived forest road maps with a resolution of 0.5 m (Fig. 5.13).

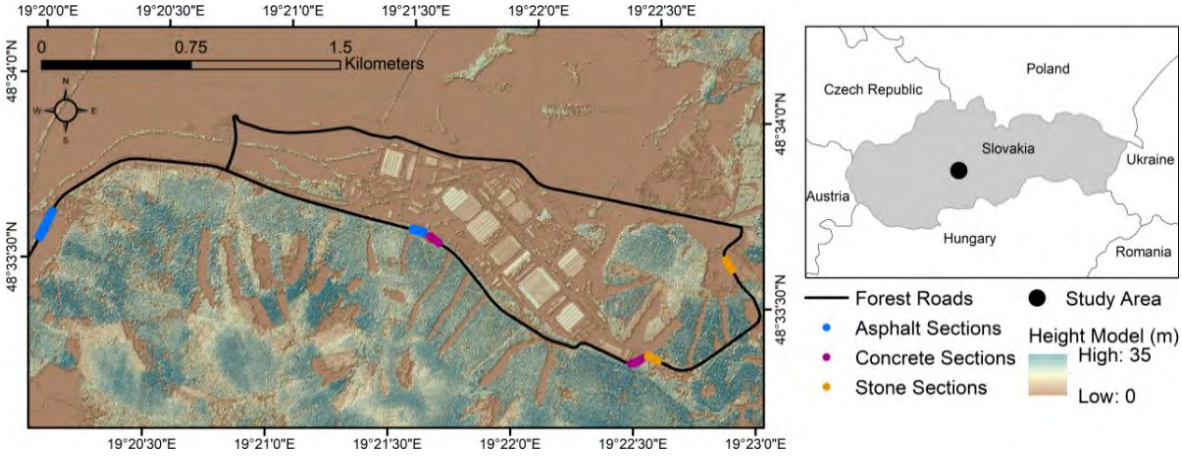

Figure 5.13. *Study area containing the forest road with three asphalt sections (total length of 150 m), two concrete sections (total length of 100 m), and two stone sections (total length of 100 m).*

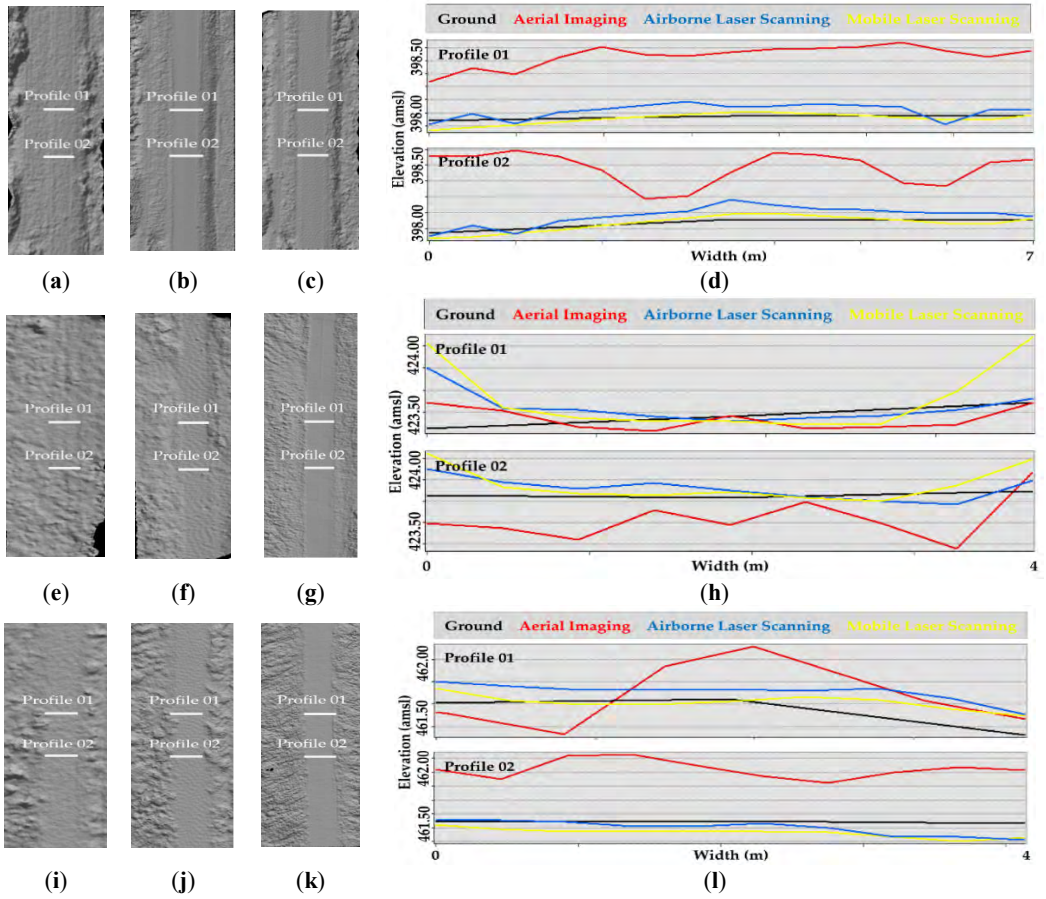

Figure 5.14. *Visualizations of terrains from forest road maps: (a) asphalt roads derived based on AI data; (b) asphalt roads derived based on ALS data; (c) asphalt roads derived based on MLS data; (d) longitudinal profiles of asphalt roads; (e) concrete roads derived based on AI data; (f) concrete roads derived based on ALS data; (g) concrete roads derived based on MLS da-ta; (h) longitudinal profiles of concrete roads; (i) stone roads derived based on AI data; (j) stone roads derived based on ALS data; (k) stone roads derived based on MLS data; (l) longitudinal profiles of stone roads. Note: AI: aerial imaging; ALS: airborne laser scanning; MLS: mobile laser scanning.*

The highest precision was found on asphalt roads derived from mobile laser scanning data (RMSE from ±0.01 m to ±0.04 m) and airborne laser scanning data (RMSE from ±0.03 m to ±0.04 m). On the other hand, the lowest precision was found on all roads derived from aerial imaging data (RMSE from ±0.11 m to ±0.23 m). Furthermore, we found significant differences in elevation between the measured and derived terrains. However, the differences in elevation between specific techniques, such as in-verse distance, natural neighbour, and conversion by average, were mostly random. Moreover, we found that airborne and mobile laser scanning technologies provided terrain on concrete and stone roads with random elevation differences. In these cases, it is possible to replace a specific technique or technology with one that is similar without significantly decreasing the elevation accuracy (Fig. 5.14).

National Agricultural and Food Centre – Soil Science and Conservation Research Institute

1. Remote sensing control of area-based subsidies in agriculture

The subsidies play a key role in agriculture sector and contribute to the prosperity of agricultural subjects. The subsidies to agriculture sector represent major part of European budget and that is why there is taken an emphasis to the control.

During the years 2024 and 2025, the CwRS was no longer performed at the NPPC – VÚPOP, unlike previous years / periods.

2. Quality Assessment of Land Parcel Information System – QA LPIS (2024;2025)

Integrated Administration and Control System - represent main tool of EU CAP– IACS manages, monitors and serves for EU countries to control all the area and animal-based common agricultural policy (CAP) interventions (such as direct payments interventions and area and animal-based rural development interventions), and ensures that comprehensive and comparable data is available throughout the EU. The general rules applying to the integrated system IACS for the common agricultural policy (CAP) period 2023-2027 are defined in Regulation (EU) 2021/2116. Three elements of the IACS: LPIS (the identification system for agricultural parcels), GSA (the geo-spatial application system) and AMS (the area monitoring system) are quality assessed in accordance with a methodology set up at European Union level. The quality assessments serve a different purpose than the control and penalty systems. The main purposes of the quality assessments are the assessment of the reliable implementation of each system, to provide diagnostic information on the sources of incorrect decisions at the level of interventions and eligibility conditions (AMS quality assessment) and to ensure that the integrated system provides reliable, comprehensive and verifiable data for the Annual Performance Reporting (APR). The quality assessments shall be carried out following a methodology set up at Union level for each Strategic Plan (SP). Union level methodology is elaborated by DG AGRI in collaboration with the Joint Research Centre (JRC) and EU member states.

Land Parcel Identification System (LPIS) is the main component of Integrated Administration and Control System (IACS) for area based direct support. LPIS quality assessment (QA LPIS) is an assessment done and used by the MS to identify recurrent/systemic potential weaknesses in their LPIS database. It is realized through 9 statistical quality elements. It is being assessed the maximum eligible area of the system (absence of bias (i.e. accuracy) of

the land represented in the LPIS as a whole; overestimation areas and underestimation areas); proportion of items with incorrectly recorded area or “contaminated” with ineligible features; classification error (incorrect recording of agricultural land cover classes); functional issues "critical defects” of the reference parcels; categorization of the non-conformities; error types (Changes of the underlying land were not applied – typical examples are a newly constructed road or building that is still being considered agricultural land or a recent conversion into agricultural land that has not been taken into account. Erroneous processing - the operator has used inappropriate (e.g. outdated) source material or there has been a manifest deviation from the documented instructions.), etc.

The geo-spatial application system (GSA) shall be used for all area-based interventions under the integrated system and for the relevant information in relation to conditionality, also in case of the beneficiaries who are subject to conditionality but are not applying for support under the area-based interventions. Area Monitoring System (AMS) verified whether the required agricultural activities have taken place on agricultural areas in accordance with the conditions for providing direct payments to beneficiaries. The verification is based on the evaluation of data from remote sensing of the Earth, specifically regularly produced satellite images (Planet / Sentinel). AMS has services: crops (presence of declared crop, occurrence of permanent grassland, non-homogeneity of the area), mowing (performance of agrotechnical operation on the required date/on an unauthorized date on non-productive areas), culture (change of declared culture, non-homogeneity of the area). AMS monitoring is mandatory for all EU Member States under the new Common Agricultural Policy (CAP) for the years 2023-2027 and Article 10 of the European Commission Implementing Regulation No. 2022/1173.

Quality assessment implementation is based on current satellite images taken in the year of review. Selected reference parcels for QA LPIS and QA GSA/AMS were on SSCRI (Soil Science and Conservation Research Institute) vectorised on the background of current satellite images, provided by EC. Subsequently, they are compared with the valid state of the selected (according to ranking list provided by JRC) reference parcels GSA/AMS and LPIS layer. Selected parcels are ranked according to the previous year. The satellite images were overlaid with the digitized vectors showing the position of the parcels which were checked. The land use check was completed by Rapid field visits RFVs; directly in the field in cases of ambiguous situation on satellite images.

VHR satellite imagery

Quality assessment of the Slovak IACS was realized in 14 zones for campaign year 2024 and in 14 zones for campaign year 2025 (Fig. 5.15; Tabs. 5.1, 5.2). VHR satellite imagery for each zone were delivered from JRC EC. The data provided are non-orthorectified, native resolution, pansharpened images with 4 multispectral bands. They are at georeferenced level, without correction from acquisition and off-nadir terrain effects, to allow for independent orthorectification. The reference system is UTM/WGS84 with UTM zone depending on the tile location, delivered in a 16 bits GeoTIFF format. The coverage will present homogeneous characteristics with respect to temporal, spectral and spatial properties (acquisition windows, spectral bands, radiometry stability). The Satellite images were georeferenced by SSCRI staff. Measured and archive control and check points were used. For all zones the Quality checks of georeference were carried out and control protocol were elaborated. The edited VHR images also serve as a basis for updating the relevant LPIS parcels (Fig. 5.16).

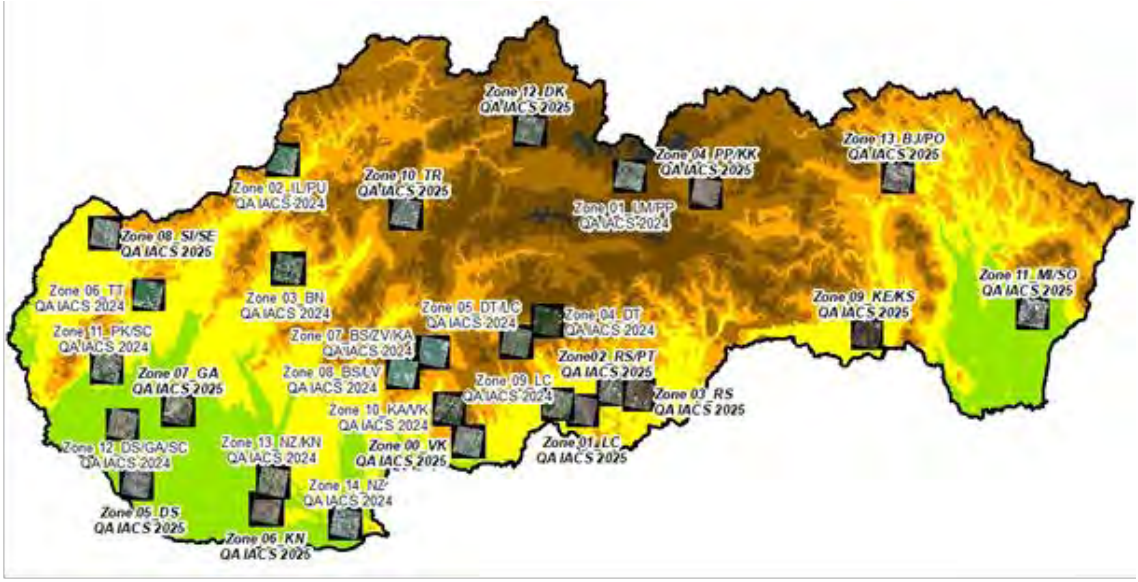

Figure 5.15. *Localization of the controlled sites in quality assessment QA IACS 2024 and 2025.*

ZoneID	Acquisition date	Platform	pixelsizeM	imageTypeETS	District	QA LPIS measured reference parcels
IACS2024-SK-1	12.04.2024	PLEIADESNEO3	0.3	PSH-FCC-RGB	Poprad/Kežmarok	12
IACS2024-SK-2	19.06.2024	PLEIADESNEO3	0.3	PSH-FCC-RGB	Ilava/Púchov	32
IACS2024-SK-3	05.06.2024	PLEIADESNEO4	0.3	PSH-FCC-RGB	Bánovce nad Bebravou	25
IACS2024-SK-4	26.05.2024	PLEIADESNEO4	0.3	PSH-FCC-RGB	Detva	45
IACS2024-SK-5	12.04.2024	PLEIADESNEO3	0.3	PSH-FCC-RGB	Detva/Lučenec	35
IACS2024-SK-6	05.06.2024	PLEIADESNEO4	0.3	PSH-FCC-RGB	Trnava	12
IACS2024-SK-7	24.06.2024	PLEIADESNEO3	0.3	PSH-FCC-RGB	Banská Štiavnica/Zvolen/Krupina	13
IACS2024-SK-8	24.06.2024	PLEIADESNEO3	0.3	PSH-FCC-RGB	Banská Štiavnica/Levice	9
IACS2024-SK-9	24.06.2024	PLEIADESNEO3	0.3	PSH-FCC-RGB	Lučenec	22
IACS2024-SK-10	07.07.2024	PLEIADESNEO4	0.3	PSH-FCC-RGB	Krupina/Veľký krtíš	33
IACS2024-SK-11	06.05.2024	PLEIADESNEO4	0.3	PSH-FCC-RGB	Pezinok/Senec	13
IACS2024-SK-12	19.06.2024	PLEIADESNEO3	0.3	PSH-FCC-RGB	Dunajská Streda/Galanta/Senec	16
IACS2024-SK-13	19.06.2024	PLEIADESNEO3	0.3	PSH-FCC-RGB	Nová Zámky/Komárno	19
IACS2024-SK-14	12.04.2024	PLEIADESNEO3	0.3	PSH-FCC-RGB	Nové Zámky	14
						300

Table 5.1. *VHR sites and localization of the measured reference parcels in quality assessment QA LPIS 2024.*

ZoneID	Acquisition	Platform	pixelsizeM	imageTypeETS	District	QA LPIS measured reference parcels
IACS2025-SK-0	09.04.2025	WORLDVIEW3	0.312	PSH-FCC-RGB	Veľký Krtíš	23
IACS2025-SK-1	22.04.2025	WORLDVIEW3	0.348	PSH-FCC-RGB	Lučenec/Rimavská Sobota	23
IACS2025-SK-2	29.04.2025	WORLDVIEW3	0,314	PSH-FCC-RGB	Rimavská Sobota/Poltár	27
IACS2025-SK-3	14.04.2025	WORLDVIEW2	0,476	PSH-FCC-RGB	Rimavská Sobota	16
IACS2025-SK-4	14.04.2025	WORLDVIEW2	0,476	PSH-FCC-RGB	Poprad/Kežmarok	17
IACS2025-SK-5	17.04.2025	WORLDVIEW3	0,318	PSH-FCC-RGB	Dunajská Streda	20
IACS2025-SK-6	29.04.2025	WORLDVIEW3	0,313	PSH-FCC-RGB	Komárno	17
IACS2025-SK-7	12.05.2025	WORLDVIEW2	0,479	PSH-FCC-RGB	Galanta/Šaľa	14
IACS2025-SK-8	2.5.2025; 13.6. 2025	WORLDVIEW3	0,316	PSH-FCC-RGB	Skalica/Senica	10
IACS2025-SK-9	14.04.2025	WORLDVIEW2	0,468	PSH-FCC-RGB	Košice - okolie/Košice II, IV	28
IACS2025-SK-10	29.04.2025	WORLDVIEW3	0,317	PSH-FCC-RGB	Turčianske Teplice/Martin	22
IACS2025-SK-11	21.04.2025	WORLDVIEW3	0,312	PSH-FCC-RGB	Michalovce/Sobrance	26
IACS2025-SK-12	19.06.2025	GEOEYE1	0,411	PSH-FCC-RGB	Dolný Kubín	42
IACS2025-SK-13	14.04.2025	WORLDVIEW2	0,477	PSH-FCC-RGB	Bardejov/Prešov	15
						300

Table 5.2. *VHR sites and localization of the measured reference parcels in quality assessment QA LPIS 2025.*

Figure 5.16. *Example of identification of a potential critical defect - Total absence of eligible features on the QA VHR 2025. It was confirmed by rapid field visit. It was not a systematic error, but a mistake caused by update – changes of the underlying land were not applied (the land use change occurred after the cyclical update of LPIS).*

3. Remote sensing within crop yield and crop production forecasting (2024; 2025), including further subsequent project Uranos activities dedicated to further improving the results

Development of crop-oriented yield forecasting

Since 2015, NPPC – VÚPOP has been carrying out crop and production forecasts in the current agricultural seasons for the main crops (winter – rapeseed, barley, wheat, summer – corn, sunflower, sugar beet and potatoes). The input data for these forecasts were weather data, crop areas and the NDVI vegetation index.

However, these forecasts do not take the NDVI index into account specifically for individual crops. In order to increase the accuracy of crop estimates, there was a need to create crop-oriented crop forecast, for which the NDVI vegetation index can be used.

NDVI (Normalized Difference Vegetation Index) are derived from NOAA's AVHRR sensor. The NDVI Vegetation Index, characterizes the total biomass state (volume and vitality), the higher the NDVI value, the more biomass is developed (characterized by a higher content of chlorophyll in plants and hence a more potent photosynthesis).

When creating a study in accordance with goals and methodological procedures within project URANOS (Data and knowledge support for decision-making and strategic planning systems in the field of agricultural landscape adaptation to climate change and minimization of agricultural soil degradation) and subsequent activities, dedicated to further improving the results; where we are dealing with the creation of a crop-oriented yield forecast, the two most agriculturally productive areas of Slovakia, which significantly affect the prices of agricultural commodities, were examined. Together, they make up almost 63% of the total arable land in Slovakia. These are the Danube Plain (Podunajská nížina), which occupies approximately 52% (9,820 km^2) – part of the Lesser Hungarian Plain and the East Slovak Plain (Východoslovenská nížina) 11% (2,500 km^2) – part of the Great Hungarian Plain.

The NDVI index was determined for the crops: rapeseed, wheat, barley, sunflower, corn, sugar beet, soybean and permanent grasslands. Each of the crops has unique spectral characteristics, different reflectance in spring or in summer, which allows their individual

distinction based on the obtained NDVI index data. Data for the years 2018, 2019, 2020, 2021 were used. At first we created a library of representative values of monitored parameters at different spatial resolution levels (agriculture parcel, district) From the satellite image records for all periods of the monitored period since 2011, only those that had reliable records were selected. Subsequently, a library of NDVI index values (and subsequently their weighted averages) was created at the level of parcels by crops (wheat; barley; canola; corn; sunflower; sugar beet; potatoes; soybeans and permanent grasslands) and districts for all periods (8 days NDVI average's) and years.

References:

[1] AFZALI, H. – RUSNÁK, M. (2025). Ensemble machine learning models for monitoring riparian vegetation dynamics using historical aerial orthophotos. *Remote Sensing Applications: Society and Environment*, 38, 101545. https://doi.org/10.1016/j.rsase.2025.101545

[2] BUCHA, T. – KONÔKA, B. – PAVLENDA, P. (2024). Vplyv stanovištných faktorov na poškodenie lesov suchom v roku 2022. [Impact of site conditions on drought-related forest damage in 2022*]. APOL: Aktuálne problémy v ochrane lesa – Časopis Lesníckej ochranárskej služby*. ISSN 2644-6308

[3] BUCHA, T. – PAVLENDA, P. – KONÔKA, B. – TOMAŠTÍK, J. – CHUDÁ, J. – SUROVÝ, P. (2024). Satellite Assessment of Forest Health in Drought Conditions: A Novel Approach Combining Defoliation and Discolouration. *Forests*, 15, 1567. https://doi.org/10.3390/f15091567

[4] BUCHA, T. – PAVLENDA, P. – KONÔKA, B. – TOMAŠTÍK, J. – CHUDÁ, J. – SUROVÝ, P. (2024). Identification of drought-induced forest damage in 2022 and of its key site condition drivers through satellite imagery. *Central European Forestry Journal*, 70, 3:156-175. https://doi.org/10.2478/forJ-2024-0013

[5] BUCHALOVÁ, D. – HOFIERKA, J. – ŠUPINSKÝ, J. – KAŇUK, J. (2025). Estimating Subcanopy Solar Radiation Using Point Clouds and GIS-based Solar Radiation Models. *Remote Sensing*, 17, 2, 328. https://doi.org/10.3390/rs17020328

[6] FISCHER, J. – GROENEMEIJER, P. – HOLZER, A. – FELDMANN, M. – SCHRÖER, K. – BATTAGLIOLI, F., – FEDOR, T. – HOFIERKA, J., et al. (2025). Invited perspectives: Thunderstorm intensification from mountains to plains. *Natural Hazards and Earth System Sciences*, 25, 8, 2629-2656. https://doi.org/10.5194/nhess-25-2629-2025

[7] GOGA, T. – OPRAVIL, Š. – RUSNÁK, M. – FERANEC, J. – SZATMÁRI, D – PAPČO, J. – FENCÍK, R. – PAZÚR, R. – KOPECKÁ, M. Detection of potential illegal environmental activities in Slovakia based on earth observation data. (2025). *Journal of Maps*, 21, 1, 2464054. https://doi.org/10.1080/17445647.2025.246405

[8] KARDOŠ, M. – BOROWSKI, Ł. – SAČKOV, I. – TOMAŠTÍK, J. – ČURILA, D. – MACIUK, K. – FERENČÍK, M. – BASISTA, I. (2025). Accuracy of Forest Road Digital Terrain Models Captured Using Airborne and Mobile Light Detection and Ranging Technology and Photogrammetry. *Advances in Geodesy and Geoinformation*, 74, 1, e65. https://doi:10.24425/agg.2025.154149

[9] KARDOŠ, M. – SAČKOV, I. – TOMAŠTÍK, J. – BASISTA, I. – BOROWSKI, Ł. – FERENČÍK, M. (2024). Elevation Accuracy of Forest Road Maps Derived from Aerial

Imaging, Airborne Laser Scanning and Mobile Laser Scanning Data. *Forests*, 15, 840. https://doi:10.3390/f15050840

[10] KOŠÁNOVÁ, S., HALABUK, A, KENDERESSY, P., RUSŇÁK, T. (2025) Assessment of yield stability patterns using sentinel-2 over a 7-year period. *Geocarto International*, 40, 1, 2532529. https://doi.org/10.1080/10106049.2025.2532529

[11] PAZÚR, R. – NOVÁČEK, J. – BÜRGI, M. – KOPECKÁ, M. – LIESKOVSKÝ, J. – PAZÚROVÁ, Z. – FERANEC, J. (2024). Changes in grassland cover in Europe from 1990 to 2018: trajectories and spatial patterns. *Regional Environmental Change*, 24, 2, 51. https://doi.org/10.1007/s10113-024-02197-5

[12] PRISHCHEPOV, A. – ANDERS, K. – FERANEC, J. – GOGA, T. – GRADINARU, S. – KOLÁŘ, J. – PAZÚR, R. – POTŮČKOVÁ, M. – ZAGAJEWSKI, B. – KUPKOVÁ, L. (2025). The progress and potential directions in the remote sensing of farmland abandonment. *Remote Sensing of Environment*, 331, 115019. https://doi.org/10.1016/j.rse.2025.115019

[13] RUSNÁK, M. – OPRAVIL, Š. – DUNESME, S. – AFZALI, H. – REY, L. – PARMENTIER, H. – PIÉGAY, H. (2025). A channel shifting GIS toolbox for exploring floodplain dynamics through channel erosion and deposition. *Geomorphology*, 477, 109688. https://doi.org/10.1016/j.geomorph.2025.109688

[14] RUSNÁK, M. – KAŇUK, J. – KIDOVÁ, A. – LEHOTSKÝ, M. – PIÉGAY, H. – SLÁDEK, J. – MICHALEJE, L. (2024). Inferring channel incision in gravel-bed rivers: Integrating LiDAR data, historical aerial photographs and drone-based SfM topo-bathymetry. *Earth Surface Processes and Landforms*, 49, 8. https://doi.org/10.1002/esp

[15] RUSNÁK, M. – KAŇUK, J. – ŠAŠAK, J. (2025). Coarse sediment grain size variability along gravel-bed rivers via automatic grain size detection (a case study of the Ondava River, Slovakia). *Geomatics, Natural Hazards and Risk*, 16, 1, 2582752. https://doi.org/10.1080/19475705.2025.2582752

[16] UHRIN, A. – ONAČILLOVÁ, K. (2025). Spatiotemporal analysis of land surface temperature and land cover changes in Prešov city using downscaling approach and machine learning algorithms. *Environmental Monitoring Assessment*, 197, 126. https://doi.101007/s10661-024-13598-8

[17] WITEK, A. – WALUSIAK, G. – HALICKI, M. – REMISZ, J. – BOROWICZ, D. – PARZÓCH, K. – KASPRZAK, Ł. – LANGHAMMER, J. – GALLAY, M. – MIŘIJOVSKÝ, J. – ŠAŠAK, J. – KAŇUK, J. – LENDZIOCH, T. – MINAŘÍK, R. – POPELKA, S. – NIEDZIELSKI, T. (2025). Reconstructing bed topography of a shallow river from close-range aerial imagery: Multi-UAV experimental campaign in the Izera river (SW Poland/N Czechia). *Geomorphology*, 471, 109544. https://doi.org/10.1016/j.geomorph.2024.109544

6. SPACE METEOROLOGY

Ján Kaňák, Ľuboslav Okon, Marian Jurašek, Peter Kaňák

6.1. Processing of data from geostationary MTG satellite at SHMÚ and new tools for visualization

MTG-I1 (Meteosat-12) satellite was declared operational on 4 December 2024 at 10:00 UTC. During 2025, at SHMÚ we have already been working with these data, although older systems had run in parallel. There are many applications that were created and used during the 20-year era of MSG satellites, and their transfer or adaptation to the new spectral bands of the new satellite, with higher spatial and temporal resolution, is not an easy task. Here we want to present only one new very useful application, which we called "GeoView-Compare RGBs". When more channels satellite provides, then more possible and useful RGB combinations can be created. For example, while we produced 20 RGB products with MSG satellites, we can generate almost 30 useful combinations from the FCI scanner placed on MTG satellite. In order of effective use such a number of products, suitable tool is needed. The above-mentioned tool allows us to arrange on the monitor screen 2, 3, 4, up to 8 different RGB products from the same timeslot and, in addition to these images, 8 additional overlay images. The user can thus choose combinations of pairs, trios, quads of images so that he can very quickly and easily compare the way a particular object can be recognized in individual RGB composites. A mouse-controlled pointer can be moved on each image at the same time and its position is synchronized during movement. A seemingly very simple idea, in practice, however, has proven to be a very effective way of visually comparing images. To demonstrate the functionality of the "Compare RGBs" tool, we study interesting winter situation with snow cover over the territory of Poland with a clear sky, without any clouds. In Figures 6.1.1, 6.1.2 and 6.1.3, we can only observe a limited feature marked on each image by a red ellipse, the position of which is synchronized on

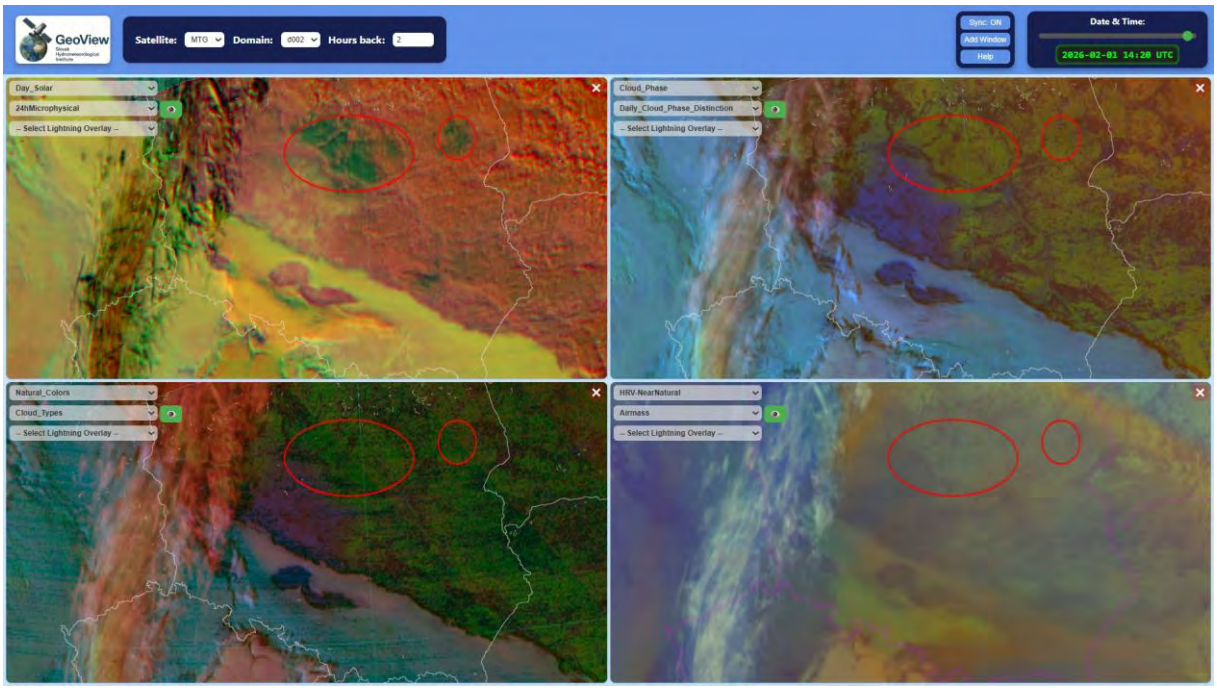

Figure 6.1.1. *Comparison RGBs from MTG satellite. Left top – 24h Microphysical, right top – Day Cloud Phase, left bottom – Cloud Types, right bottom – Airmass.*

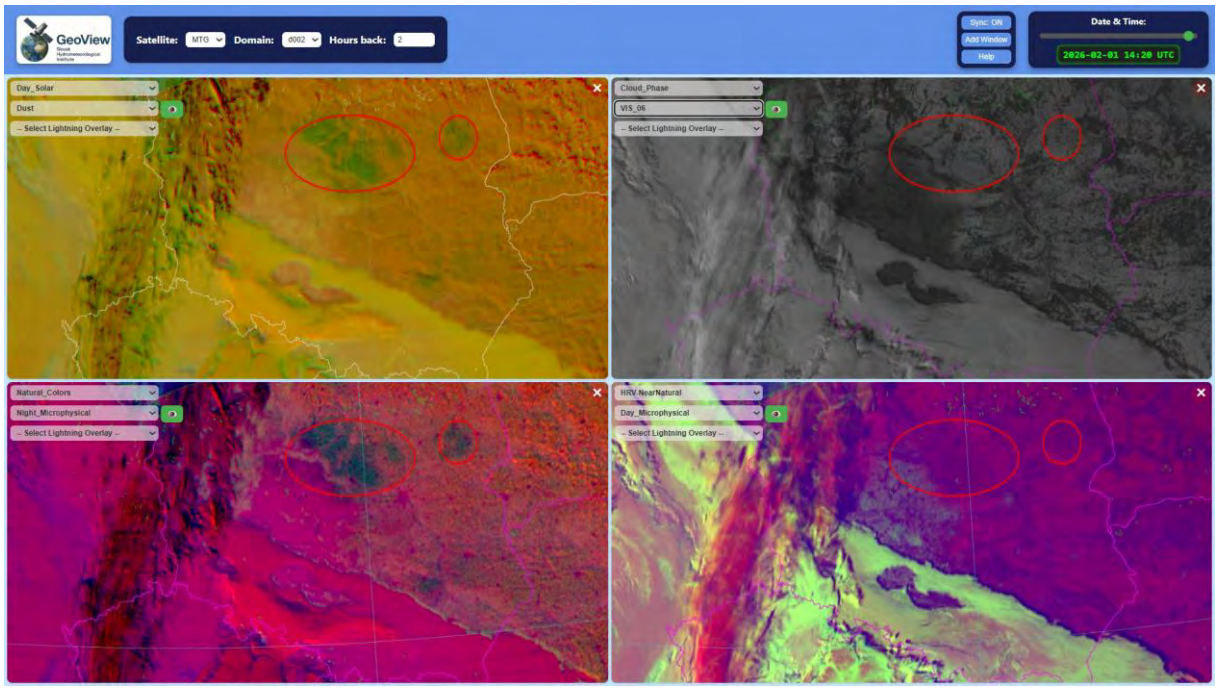

Figure 6.1.2. *Comparison RGBs from MTG satellite. Left top – Dust, right top – VIS 0,6μm, left bottom – Night Microphysical, right bottom – Day Microphysical.*

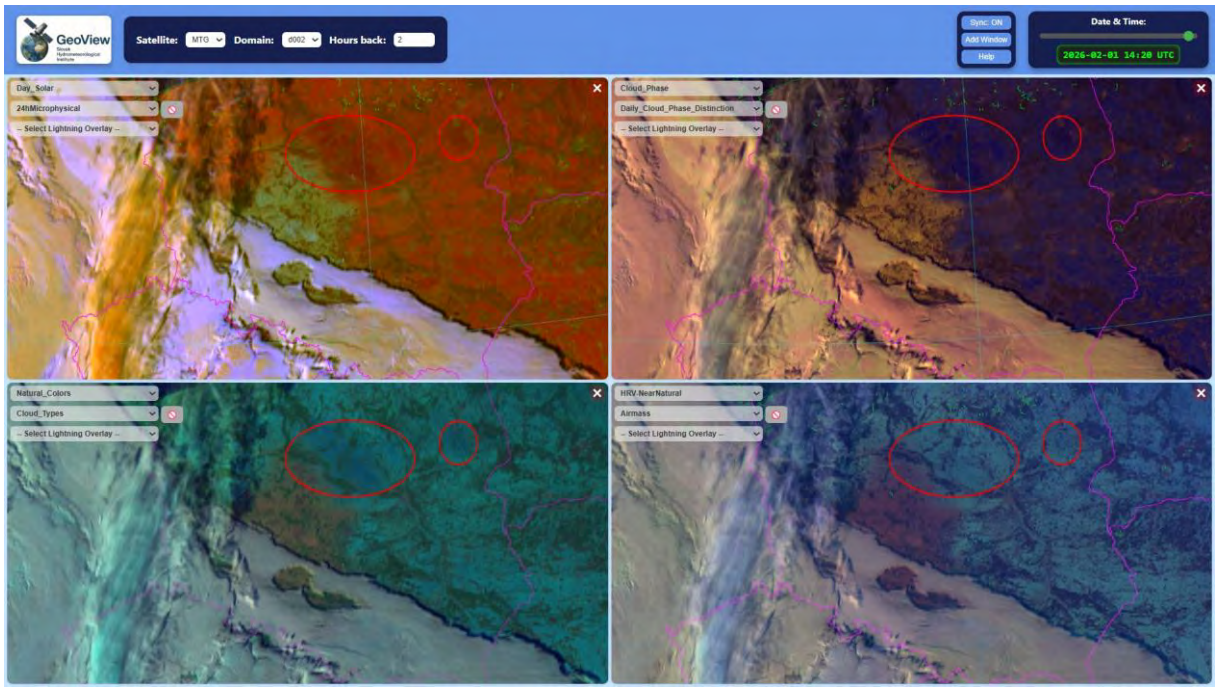

Figure 6.1.3. *Comparison RGBs from MTG satellite. Left top – Day Solar, right top – Cloud Phase, left bottom – Natural Colors, right bottom – HRV Near Natural.*

all RGB images. Thanks to this tool, we find that the object is displayed using IR channels during night and during day, but it is almost not observable using solar channels. Our preliminary conclusions are that it is probably a partially glaciated snow cover and at the same time it occurs only in some places with a certain specific earth's surface type. In this article, we do not want to predict the exact cause of this phenomenon, we just want to point out what new possibilities new spectral channels and their combinations bring, in higher spatial resolution

and in higher sensitivity and accuracy of IR radiometers, especially for channels 8.7, 9.7, 10.5 and 12.3 μm, as we can identify this phenomenon thanks to the differences in radiative temperatures.

6.2. Severe storms monitoring at SHMÚ by MTG-I1 satellite supported by FCI (Flexible Combined Imager) and LI (lightning detection Instrument) data

Convection in the atmosphere and the associated strong convective storms are often the source of extreme meteorological situations, which can lead to dangerous phenomena such as hail, tornadoes, strong winds and floods on the earth surface. These phenomena can cause extensive damages to property and human lives wherever they occur in the world.

At the upper boundary of the clouds – so called cloud tops of such storms, various typical features can be observed on satellite images, which can be used to estimate the potential danger of storms. These features significantly correlate with the strength of storms. Therefore, scientific exploitations of these phenomena is essential for improving their forecasts and issuing warnings to people. At SHMÚ, we also focus on the study of overshooting tops of storm clouds (OT = Overshooting Tops), which are formed when a strong upward air flow penetrates all the way to the tropopause. Previous research on determining the heights of OTs has been conducted by several world space agencies like NOAA, NASA, JAXA, where developed several OT detection methodologies [1]. At the SHMÚ we developed a manual but very effective method for detecting OTs with the possibility of measuring the height of their penetration into the tropopause. The created database covers period of 5 years (2011-2015) and serves as a basis for further studies that seek to introduce learning sequences of neural networks [2].

Most existing approaches to OT detection rely on thermal infrared (IR) satellite channels, either by analysing temperature variations in a single channel or by using differences between multiple IR channels. However, without knowing the height of OT penetration above the tropopause level, it is not possible to judge the strength of the outflow air currents in a storm, because only thanks to this data can it be estimated the real value of the temperature gradient in these outflows.

Recently, when we have obtained additional supporting data by putting the MTG-I1 satellite with the lightning detection instrument (LI = Lightning Instrument) into operational usage, the study of severe storms is beginning to take on a new quality. Just as the output currents change their intensity over time (pulsate), the height of the OT penetration above the tropopause also fluctuates over time - the OT will increase, decrease, and increase again at the same place or a little further away. When studying these effects, shortening the satellite's scanning frequency is very important. The FCI instrument on the MTG-I1 satellite currently scans in 10-minutes intervals, but in 2026 the MTG-I2 satellite will be launched into orbit, which will scan a smaller area of Europe instead of the entire Earth disk, but with a high image rate of 2.5 minutes.

Storms over the Mediterranean Sea with distinct OTs observed at 10. 9. 2025 05:10 UTC is shown in Figure 6.2.1. We can measure penetrating height of OT over the storm anvil equal to tropopause level, as shown in Figure 6.2.2. Measured penetrating height in this case is 4144 meters above the tropopause, which indicates very strong updraft inside the storm and consequently very dangerous when reaching human lives and their properties. Figure 6.2.3 is showing a layer of lightning activity in the storm detected by LI instrument. Oldest flashes are displayed in red, newest in yellow colour. Data are coming from satellite continuously every 10 seconds so we can update trajectory and storm position in real-time, as it is indicated in Figure 6.2.4 with red arrows.

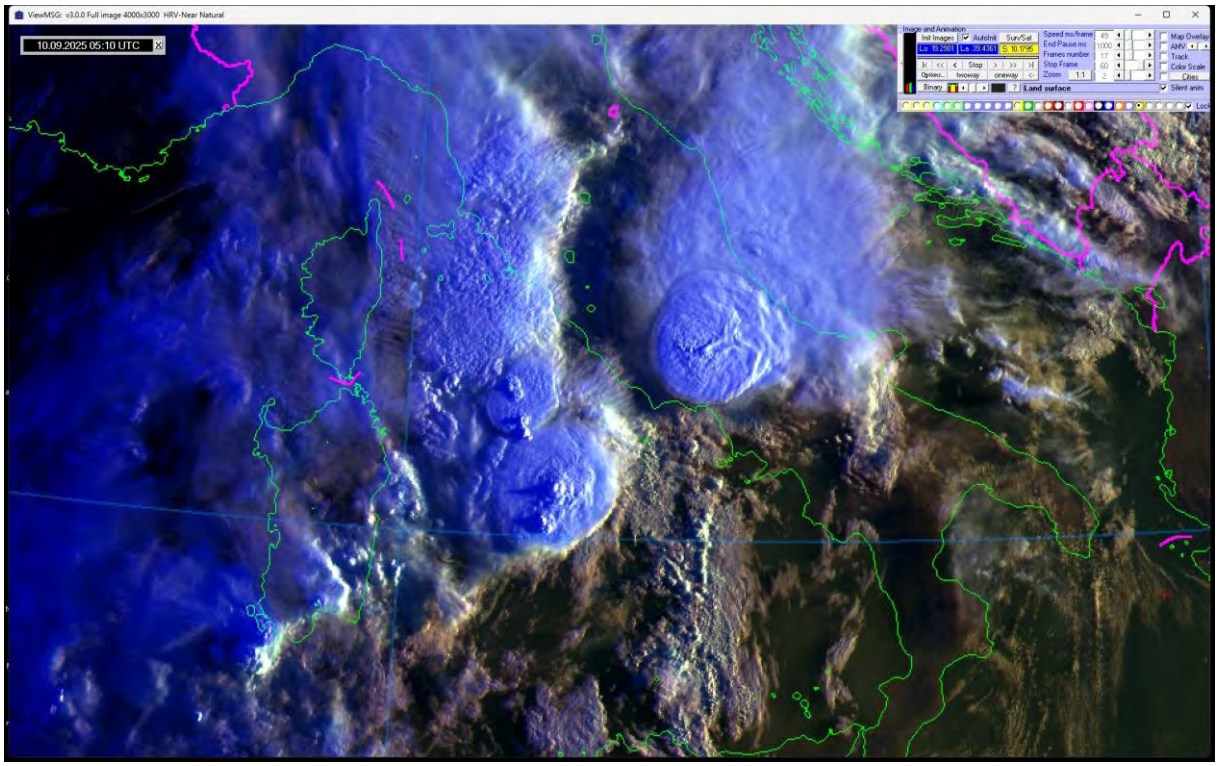

Figure 6.2.1. *Storm system over the Mediterranean Sea with distinct OTs observed at 10.9.2025 05:10 UTC.*

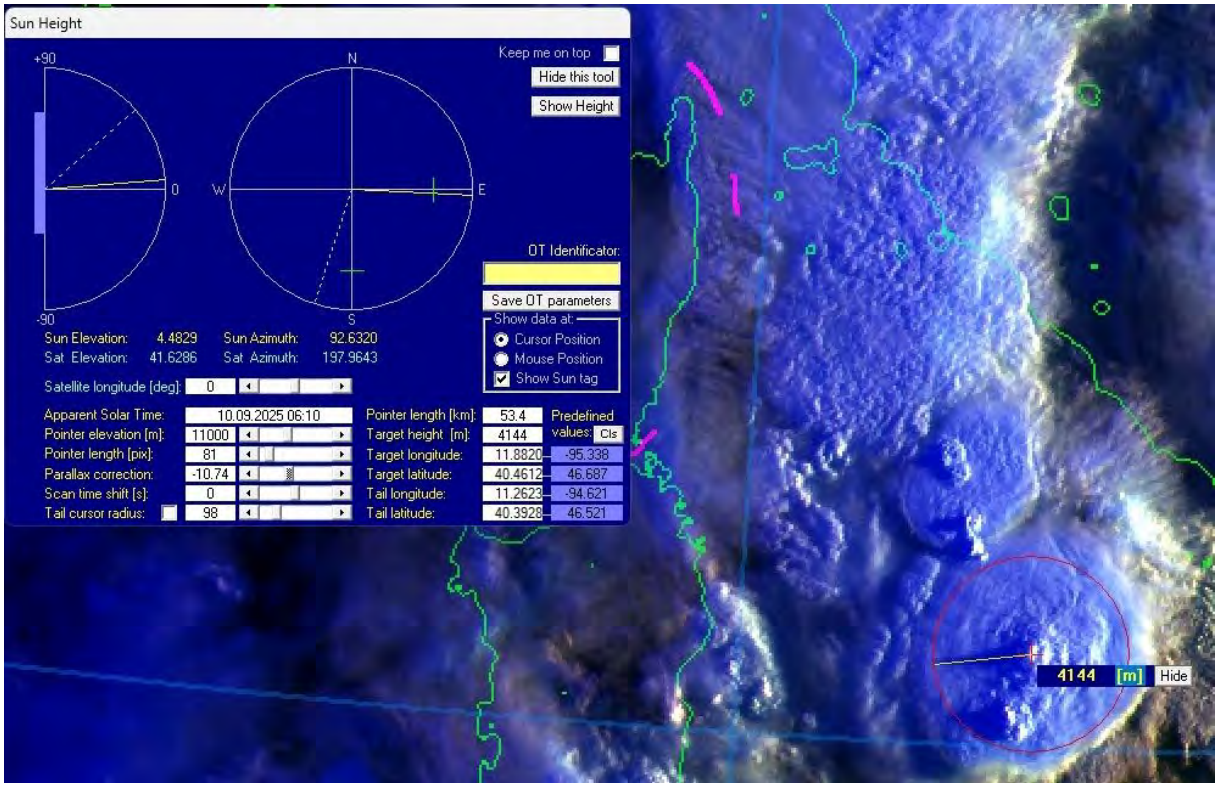

Figure 6.2.2. *The activated OT height measurement tool measured a value of 4,144 meters above the tropopause.*

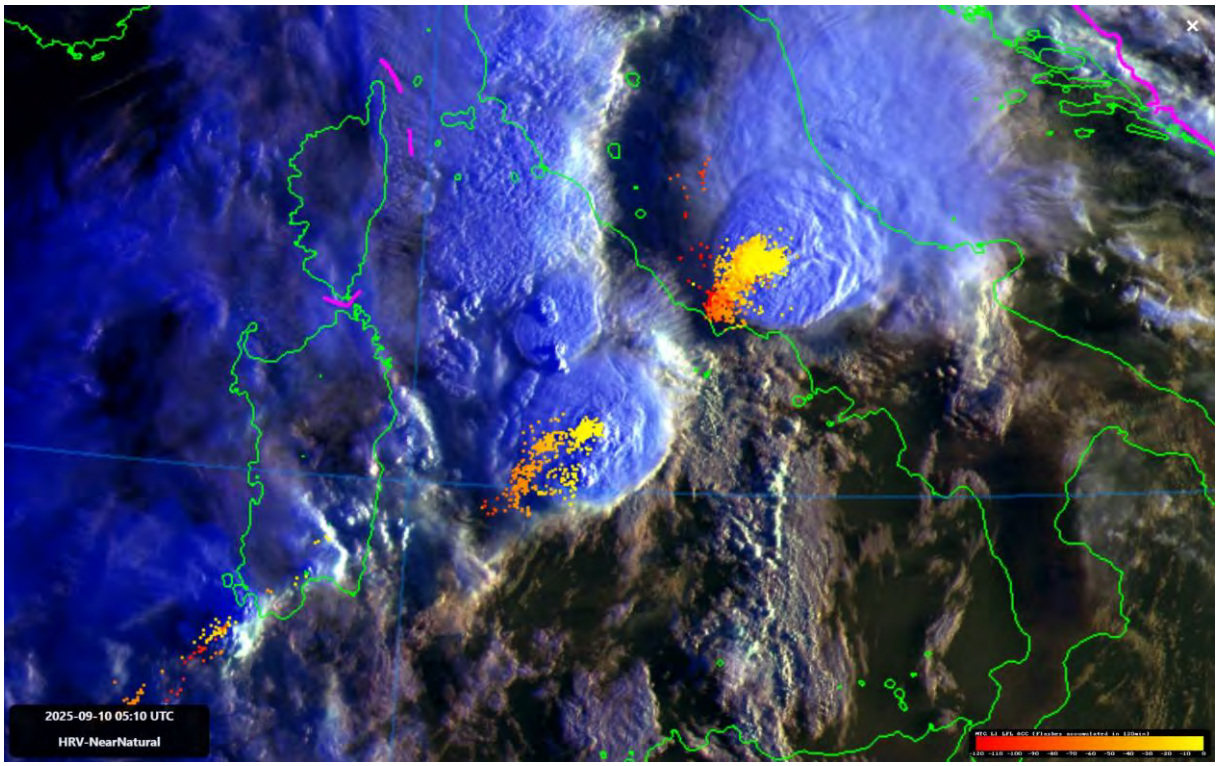

Figure 6.2.3. *A layer added over image showing the time evolution of lightning activity in the storm.*

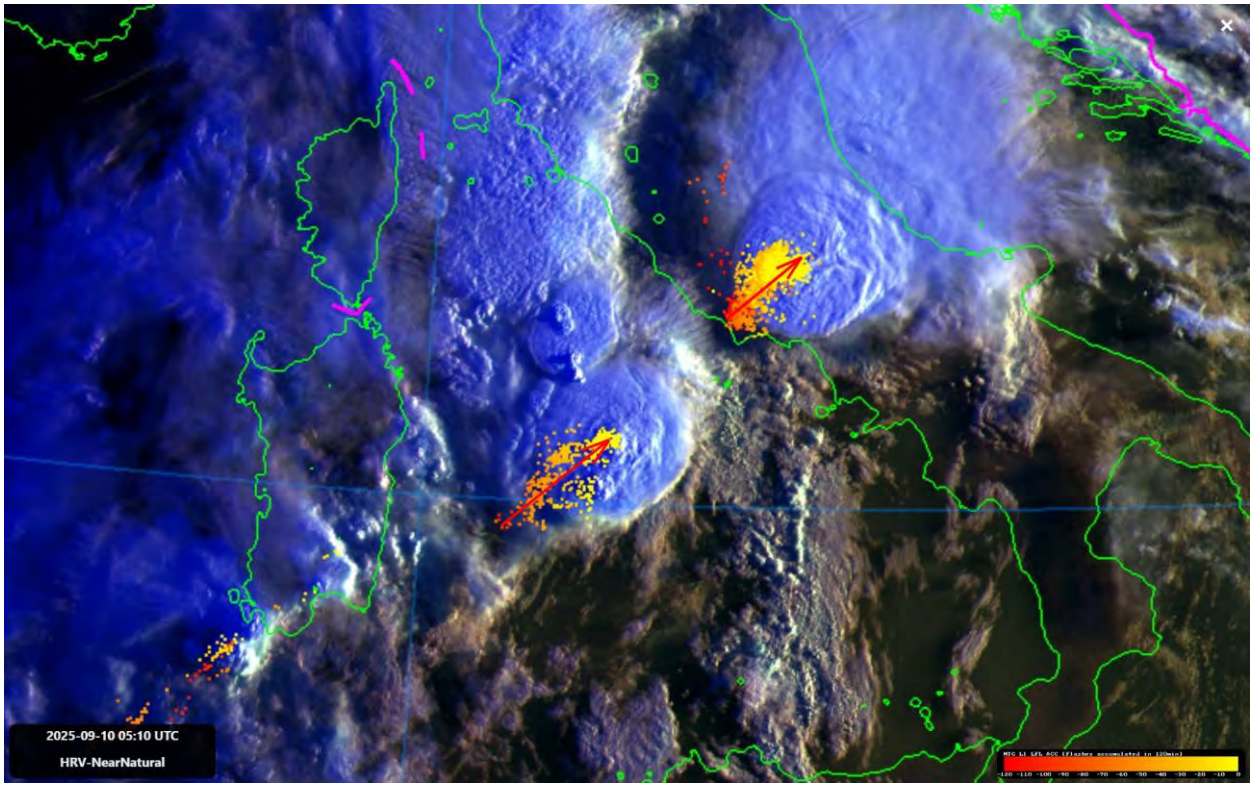

Figure 6.2.4. *Evolution of the storm position determined by the lightning density over the last 120 minutes.*

6.3. Universal Common Code (UCC) software solution for validation of satellite precipitation products now upgraded for new MTG based products

This chapter presents the history of development and latest new features of the UCC (Unified Common Code) software, which we elaborated as a part of the EUMETSAT H-SAF project consortium precipitation validation activities. We started developing validation methodology and procedures immediately when the first precipitation products were available in 2007. The first and physically essential products based on microwave cross-track and conical scanners on board of polar satellites, H01 and H02 were encoded in the BUFR format. Above them as reference data layer, a layer of target products H03, H15 and H18 was created in a regular time step of the Meteosat satellite (MSG) measurements, which provides instantaneous values of precipitation intensities every 15 minutes in GRIB format. By integrating these products over time, the H05 accumulated precipitation products useful for hydrologists are obtained, providing precipitation totals for 1 hour, 3, 6, 12 and 24 hours. Later, from July 2025 new changes were applied which introduced encoding precipitation data in the more general NetCDF format. This format is still used nowadays for the H60, H61, H63, H64, H68 and H90 products and for new H40 and H42 products based on new MTG-FCI data in higher space and time resolution in comparison to MSG-based products.

The validation methodology in the H-SAF project for precipitation products is based on statistical comparisons of data from these products pixel by pixel against ground-based reference data covering area of interest predefined for various countries (SK, PL, HU, IT, BE, TU). The reference data are either rain gauge or radar measurements. In both cases, pairs of data matrices are compared in a regular grid, or in a grid corresponding to the native resolution of satellite observations. Therefore, it is important to convert the reference data to the satellite grid, which we call upscaling.

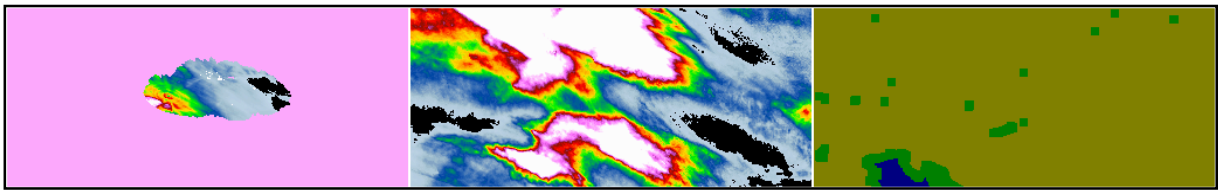

Figure 6.3.1. *MSG-based results: Ground reference – radar (left), validated satellite precipitation product (middle) and land/sea/coast mask (right) for product H61 created on the base of MSG satellite data. Valid for 13. 1. 2026 06:00 UTC rain from 24-hours accumulation period started at 12.1.2026 06:00 UTC. Lower satellite resolution results to coarser discrimination of coastal areas.*

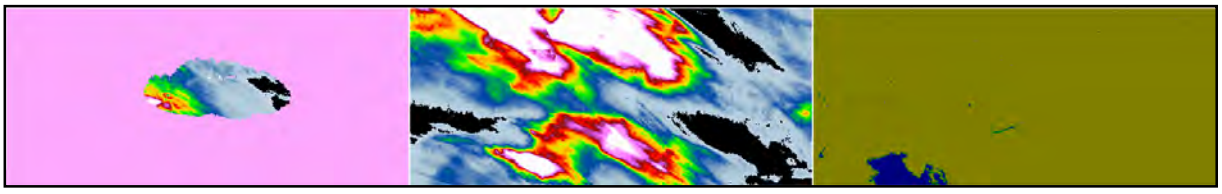

Figure 6.3.2. *MTG-based results: Ground reference – radar (left), validated satellite precipitation product (middle) and land/sea/coast mask (right) for product H42 created on the base of MTG satellite data. Valid for 13. 1. 2026 06:00 UTC rain from 24-hours accumulation period started at 12.1.2026 06:00 UTC. Higher satellite resolution enables better discrimination between land, sea and coastal areas and better statistical filtering of validated data.*

The latest version of the UCC software v.2.1 is user-friendly in the way that user sets up a set of parameters that define the type of satellite product, the reference ground data, the region of interest and the time period of validated event through a single command line. Auxiliary information about satellite product and reference data is stored in configuration file modifiable by user. The software automatically prepares a look-up table for upscaling the reference data, creates data pairs pixel by pixel and time slot by time slot. Finally, the resulting data set is evaluated by providing a set of standard statistical parameters, such as POD, FAR, CSI, RMSE, Bias, Correlation coefficients, etc.

Using the UCC validation software, we are able to perform mutual comparison of the validation results of the older version of precipitation products, generated on the base of data from the MSG satellite, and the validation results of the new precipitation products, generated on the base of data from the MTG satellite. The differences in these two sets of products mainly result from two factors - the first is the change in the time frequency of measurements from 15 to 10 minutes, the second is the change in the spatial resolution from 3 to 2 km. Both of these parameters play a significant role in the accuracy of detecting the spatial distribution of precipitation fields and in the temporal variability of precipitation intensities, especially in convective meteorological events.

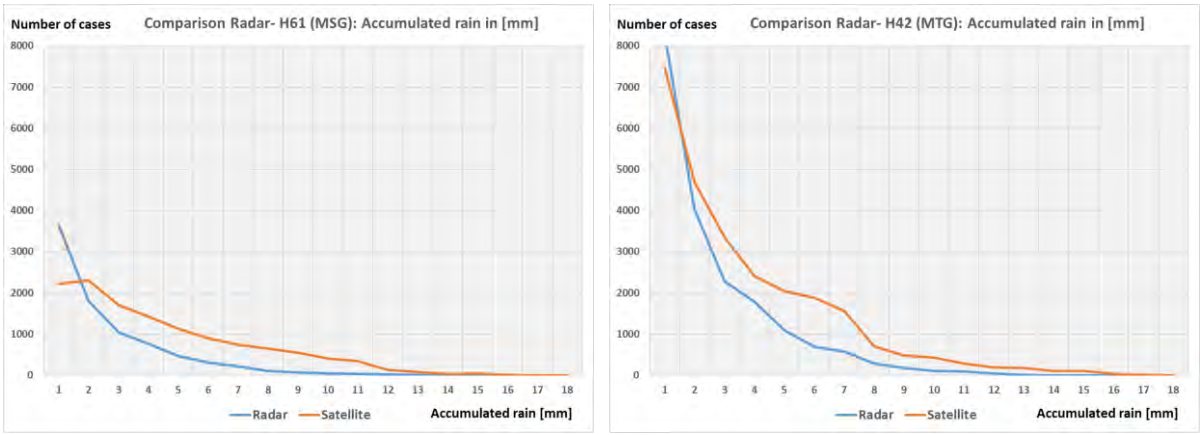

Figure 6.3.3. *Results of statistical comparison between MSG-based (H61 on left) and MTG-based (H42 oh right) precipitation products: Probability density function which describes the relative likelihood of a continuous random values of coupled radar and satellite precipitation estimations. It is evident that sensitivity of new MTG-based products is much better for low accumulated precipitation values.*

Offline statistics in the presented experiment, which we ran after upgrading the UCC software, show promising results for precipitation products prepared based on data from the latest MTG-I1 satellite (Figure 6.3.4). Since we have radar measurements as a ground reference every 5 minutes and satellite data are in a step of 10 minutes instead of 15 minutes for the older MSG satellite, the probability of detection (POD) has improved, the number of false alarms (FAR) has not changed and consequently the critical success index (CSI) has also improved. This experiment has so far been carried out only on a small part of data set from the date 13.1.2026, when precipitation over the region of interest (Slovakia) was in the form of snow. We expect that the improvement in precipitation detection by the H42 product during summer meteorological situations will be even higher. It turns out that the improvement in temporal and spatial resolution of the satellite scanner FCI (Flexible Combined Imager) compared to the SEVIRI (Spinning Enhanced Visible and Infra-Red Imager) is of significant importance.

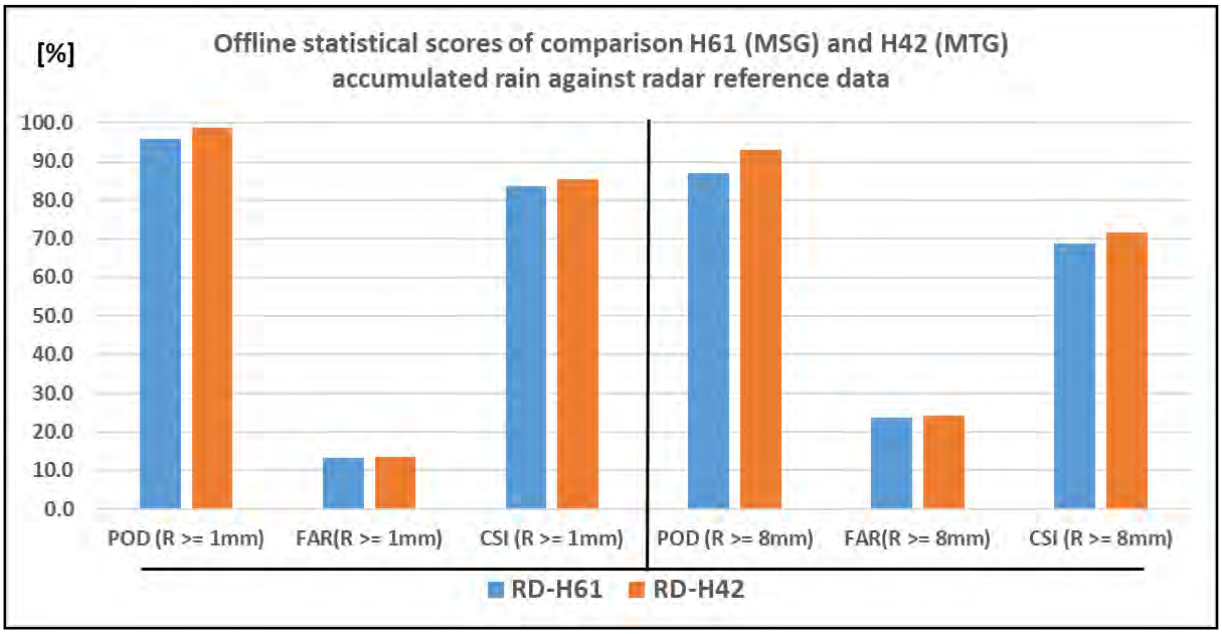

Figure 6.3.4. *Results of statistical comparison between MSG-based (H61 in blue) and MTG-based (H42 in orange) precipitation products: Offline statistical scores relates to POD (probability of detection), FAR (false alarms) and CSI (critical success index) calculated for two precipitation classes Rain ≥ 1 mm and Rain ≥ 8 mm.*

Next example is the comparison of precipitation fields from H SAF products H42, H61 and SHMÚ radar product calibrated using rain gauge data – called QPREC. All the data is in its native product resolution displayed on the same domain centered above Slovakia. Visualizing all the products in their native resolution allows us to notice the progress made with the transition from MSG based H61 to MTG based product H42 (Figure 6.3.5).

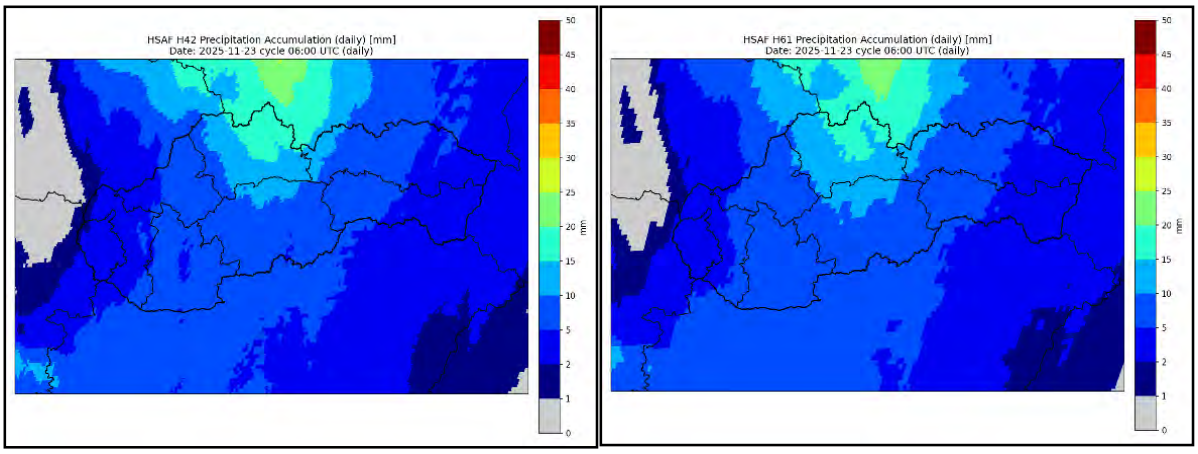

Figure 6.3.5. *H42 product from 23rd November 2025, 06:00 UTC (left), H61 product from 23rd November 2025, 06:00 UTC (right).*

There is a relatively good match of the precipitated area from both radar and satellite products. This is supported by the fact that probability of detection of precipitation above 0.1

mm by H42 product is 99.3% when we take QPREC values as a reference. The false alarm ratio is only at the 0.6%.

Visual comparison of the precipitation fields shows a shift of precipitation maximum to the north, above Poland compared to the maximum from radar product, which is located in the mid-east Slovakia in the mountainous region.

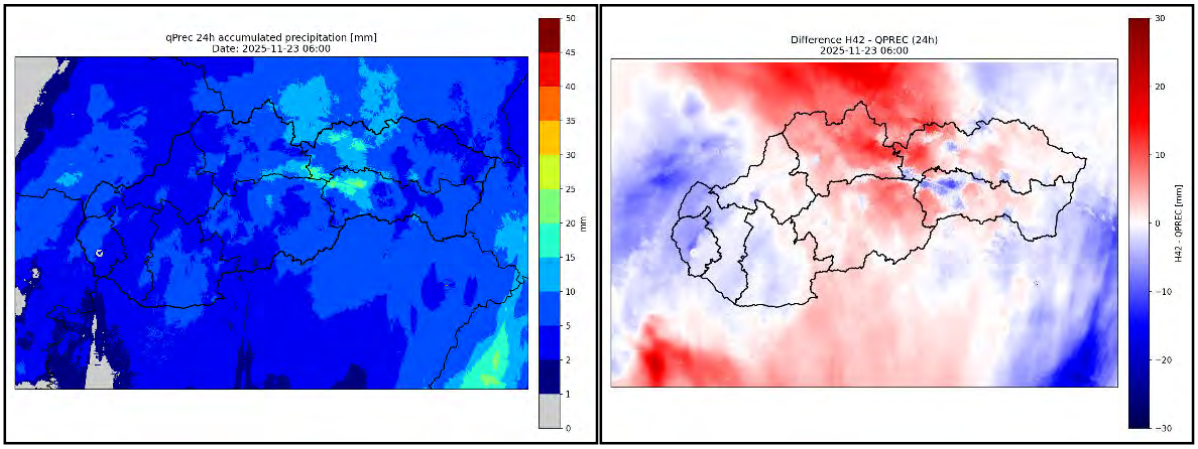

Figure 6.3.6. *Left: radar product qPrec from 23rd November 2025, 06:00 UTC, Right: Difference map of H42 accumulated precipitation subtracted by QPREC accumulated precipitation.*

On the right panel of Figure 6.3.6 we see the difference map of H42 subtracted by qPrec precipitation values. Red color means over-estimation of precipitation by H42 and blue color means under-estimation. The biggest difference is above the north of Slovakia and Poland where H SAF products report the maximum, while radar product does not state such high amounts of precipitation and rather detects the maximum a little more to the south. On the Figure 8 we can observe also some artefacts caused by radar ray blockages especially one southern from Slovakia extending over Hungary.

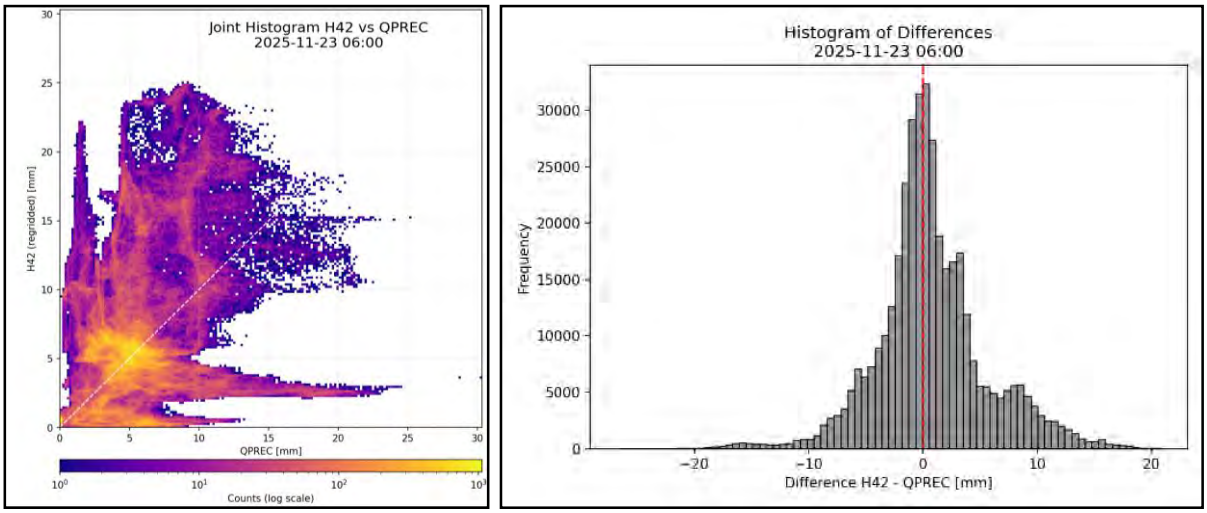

Figure 6.3.7. *Left: Density scatterplot of H42 and qPrec radar data. Right: Histogram of differences between H42 and qPrec values.*

Figure 6.3.7 provides a complementary statistical view of the H42–QPREC comparison. The density scatterplot (left panel) illustrates the relationship between H42 and radar-derived precipitation values. While a general positive relationship is evident, the scatter is wide, particularly at higher precipitation amounts, reflecting the low correlation coefficient obtained in the statistical analysis (correlation = 0.26). The spread of points above the y=x relationship indicates a tendency of H42 to overestimate precipitation, especially for moderate and high rainfall totals.

The histogram of differences (right panel) further confirms this behavior. The distribution is skewed towards positive values, demonstrating that H42 more frequently produces higher precipitation amounts than QPREC. At the same time, the broad shape of the distribution highlights substantial variability between the two datasets, which is consistent with the moderate MAE (3.5 mm) and RMSE (4.1 mm) values. Together, both panels of Figure 6.3.7 underline the good detection capability of H42 combined with limited quantitative agreement in precipitation intensity, particularly during heavier precipitation episodes.

The statistical scores for this show-case where calculated using ad hoc python code, which downscaled the H42 data into the radar data grid. The results of selected scores of continuous and dichotomous statistics are listed in Table 6.3.1 and Table 6.3.2 respectively.

Table 6.3.1. Continuous statistics

Number of pixels with precipitation	380 044
Mean QPREC	5.636 mm
Mean H42	6.314 mm
Bias	0.678 mm
Mean absolute error	3.492 mm
RMSE	4.095 mm
Correlation coefficient	0.26

After re-gridding H42 to the QPREC grid (388 500 pixels), H42 exhibits a systematic positive bias, with a mean precipitation of 6.314 mm compared to 5.636 mm for QPREC (bias: +0.678 mm). The overall error magnitude is moderate (MAE ≈ 3.5 mm, RMSE ≈ 4.1 mm), while the correlation is low (≈ 0.26), indicating limited agreement in spatial variability. This indicates over-estimation of overall precipitation by H42 product.

Table 6.3.2. Dichotomous statistics

Precipitation class	**≥ 0.1 mm**	**≥ 1 mm**	**≥ 5 mm**	**≥ 10 mm**
Correctly detected events	383 386	345 910	113 461	15 944
Falsely detected events	2 675	34 134	84 611	16 821
POD	99.3%	91.0%	57.3%	48.7%
FAR	0.6%	1.1%	47.4%	75.4%
CSI	98.7%	90.1%	37.8%	19.5%

Contingency analysis shows excellent detection of light precipitation. For the 0.1 mm threshold, the probability of detection is 99.3%, the false alarm ratio is 0.6%, and the critical success index reaches 98.7%, reflecting near-perfect identification of precipitation occurrence. Performance remains strong at the 1.0 mm threshold, with POD ≈ 91%, FAR ≈ 1.1%, and CSI ≈ 90.1%. Skill decreases markedly for higher precipitation thresholds. At 5.0 mm, the detection

rate drops to 57%, while the false alarm ratio increases to 47%, resulting in a CSI of 37.8%. The degradation is even more pronounced at 10.0 mm, where POD falls below 50%, FAR exceeds 75%, and CSI decreases to about 20%, indicating poor discrimination of heavy precipitation events. The results for the highest precipitation class (≥ 10 mm) can however be affected by small number of compared data. Overall, H42 performs well in detecting light precipitation, but shows increasing overestimation and reduced skill for moderate to heavy rainfall.

In this article, we have presented two approaches to comparing and evaluating precipitation detected by satellite observations. Both approaches are scientifically equivalent, but the goal of the presented new version of the UCC software is to automate and bulk process long data series, for example on a monthly basis. For users who have been working with HSAF precipitation data for years, it is clear that the fineness of the structure of precipitation fields has improved, especially because the resolution of IR images on the third generation Meteosat has increased. The spatial and temporal resolution of microwave data from polar satellites remains a problem. These are key for calibrating IR images to precipitation intensity. When better microwave data from polar satellites become available, precipitation detection from geostationary orbit will also be better. Perhaps the EPS-Sterna satellites, new program recently approved by the EUMETSAT Council, will bring more accurate data to improve precipitation products in the future.

6.4. Tuning of FCI instrument solar channels calibration for conditions of extremely low Sun elevation angles

The processing of solar channels has become the focus of attention with the arrival of the new FCI (Flexible Combined Imager) scanner, which, compared to the previous generation of Meteosat satellites, has new channels for blue and near-infrared light, as it brings new possibilities of true colors for imaging the clouds and surfaces of our planet. The paradox is that, due to the small bandwidth, a simple combination of RGB by means of VIS wavelengths

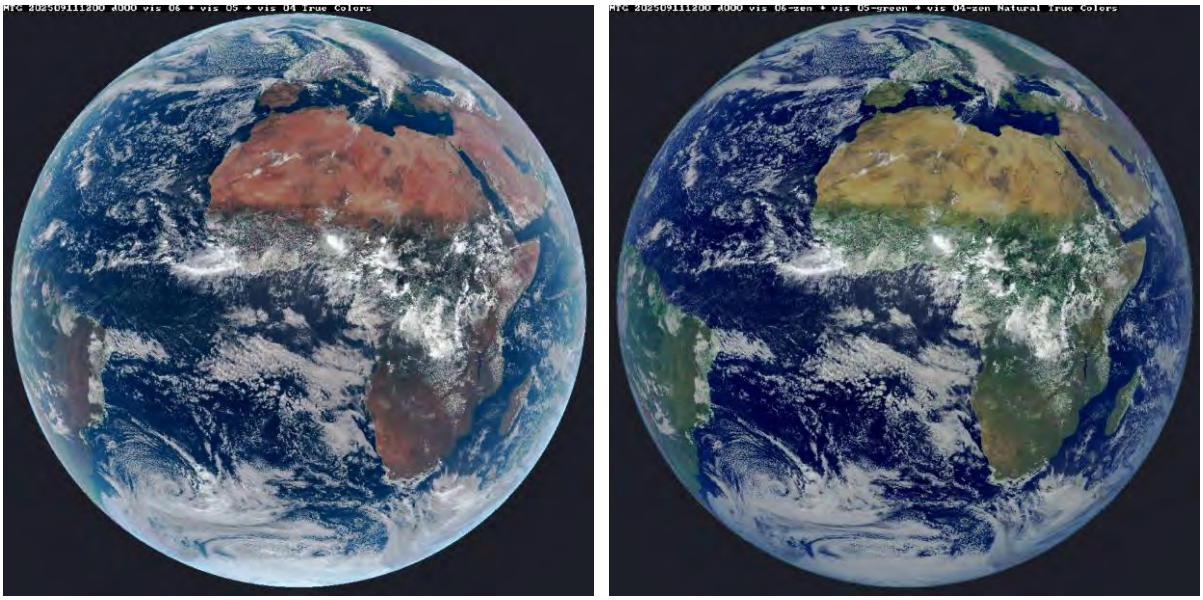

Figure 6.4.1. *True color RGB composite from the FCI instrument on board of the MTG-I1 satellite captured at 11. 9. 2025 12:00 UTC. A simple composite of VIS channels without correction (on the left) and a composite with corrections for the position of the Sun and satellite and with extended sensitivity to vegetation using the 0.8μm NIR channel.*

of 0.4, 0.5 and 0.6 μm does not provide natural colours as they would be perceived by the human eye from space. For this reason, several corrections are applied to the elevation angle of the Sun, to the zenith angle of the satellite and to the mutual azimuth angle of the Sun-Earth and Earth-satellite flow lines, as well as combining the green channel of 0.5 μm with the NIR channel of 0.8 μm. This NIR channel is much more sensitive to vegetation and thus helps to highlight the green shades in the image. The original simple RGB composite is shown in Figure 6.4.1 on the left, after applying the above corrections we obtain the result in Figure 6.4.1 on the right.

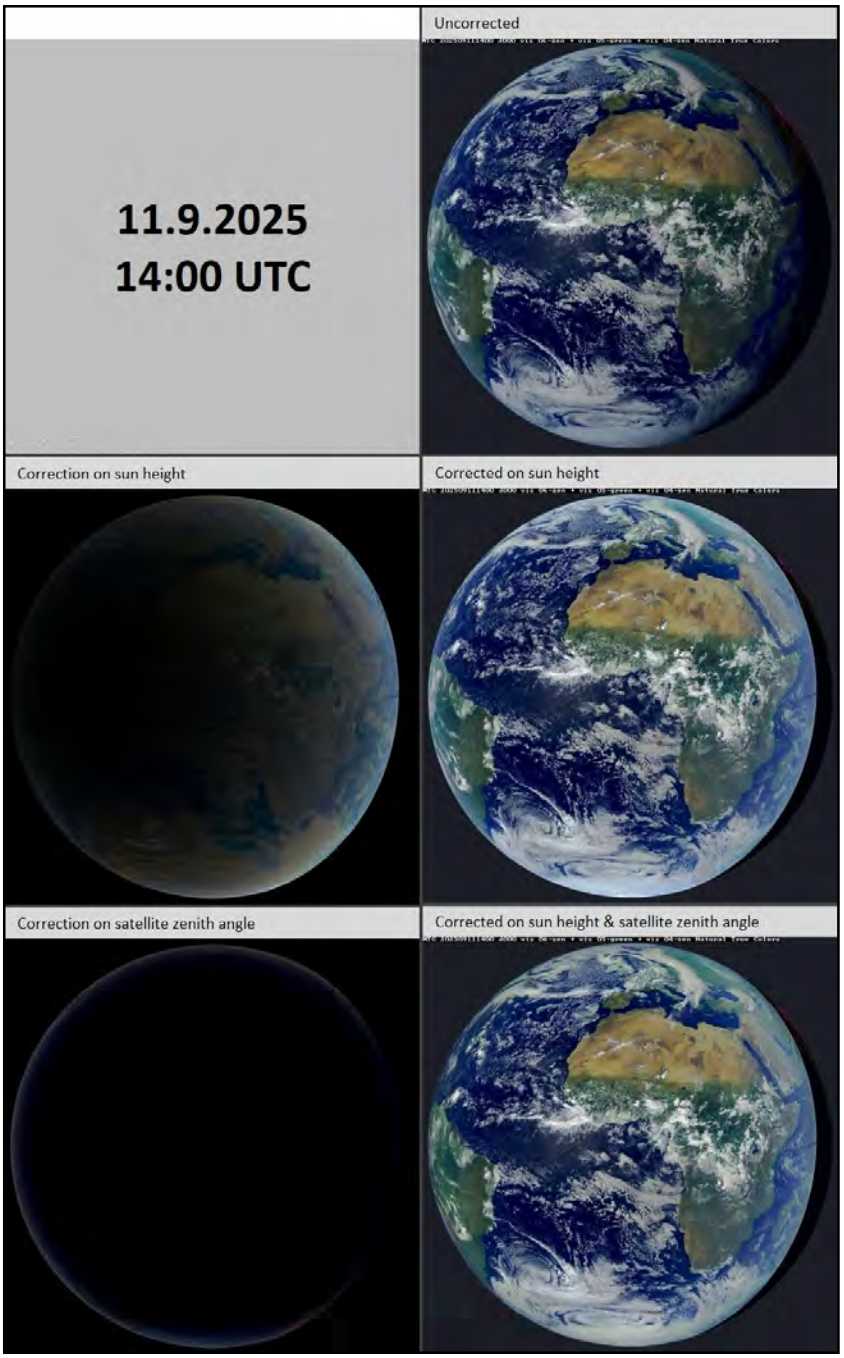

Figure 6.4.2. *Procedure for applying corrections when preparing a True Colours RGB product. Top right: uncorrected image; middle left: correction for the height of the Sun, right: resulting image with correction for the height of the Sun; bottom left: correction for the satellite zenith angle, right: resulting product with all corrections.*

There are several methods for applying the above-mentioned corrections, from highly sophisticated ones using models of radiation transfer through the atmosphere to simpler empirical corrections of brightness characteristics in different parts of the image. At SHMÚ, we have chosen our own procedure, which uses experience with empirical corrections of VIS images of previous generations of Meteosat satellites. While on the first generation Meteosat satellites there was only one VIS channel with a very wide bandwidth, on the MSG satellites we have already applied corrections to both VIS and NIR spectral channels, but we used wavelength-independent corrections. On the MTG satellite, however, the new channels for green and blue light show an increased dependence on the scattering of light in the atmosphere, especially Rayleigh scattering at very low elevations of the Sun. Processing steps and final corrected output is shown in Figure 6.4.2.

The next step to improve the display of True Colours RGB products is to change the linear luminance characteristic to a nonlinear one in order to increase the contrast of certain parts of the image, for example the land surface, sea level, cloud cover. The example in Figure 6.4.3 shows an image of Central Europe in the Albers equal-area projection. The left part of the image is an image with a linear luminance characteristic, the right part is an adjusted image with increased contrast. The curves for the individual colour components R (red), G (green) and B (Blue) used in our example are shown in Figure 6.4.4. The bottom part of the image shows the resulting luminance characteristics, which appear here as black and white. However, when applied to real data of the VIS spectral channels, we get a colour image, because in general each of the three R, G, B values has a different value depending on the objects being imaged (sea, land surface, vegetation, cloud cover).

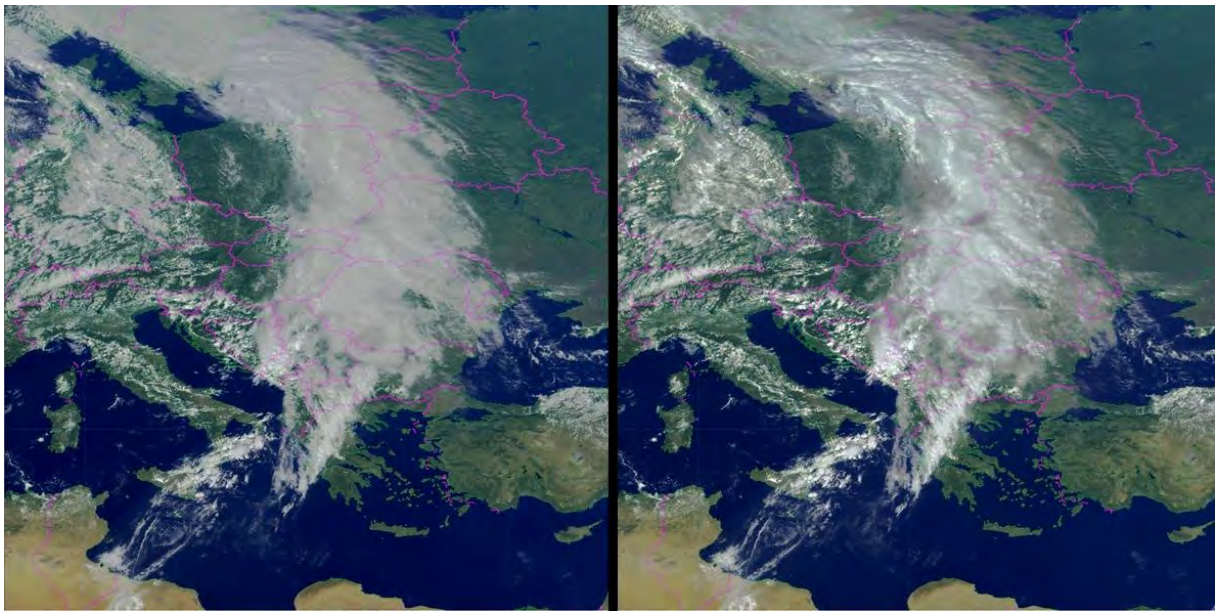

Figure 6.4.3. *True Colours RGB over European region with linear (left) and with non-linear (right) enhancement to highlight the cloud structures.*

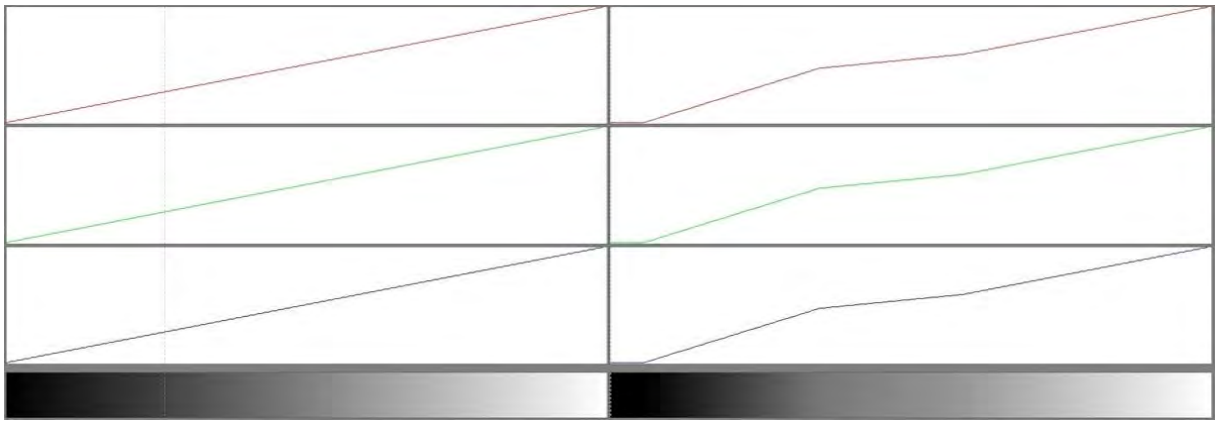

Figure 6.4.4. *Linear (left) and non-linear (right) look up tables for enhancements of True Colours RGB products.*

Curves for corrections of solar channels on the Sun elevation (Figure 6.4.5) are calculated by method originally used for all previous Meteosat satellites, but in case of MTG satellite for each solar channel individual calibration coefficients are setup according table 6.4.1, where coefficients ax and bx are specified. Correction on Sun height is performed for Sun elevation angles:

$-1{,}9° \leq \alpha \leq 90°$

For shifting hyperbolic correction curve to positive values we calculate shift of α value:
$\alpha' = (90 * \alpha + 180) / 92$

Correction is then calculated as:
Correction (α) = 1 / (ax * sin (α') + bx * sqrt (sin (α'))

Table 6.4.1. Table of calibration coefficients for solar channels.

Channel [μm]	ax	bx
VIS 0.4	0.50	0.50
VIS 0.5	0.55	0.45
VIS 0.6	0.60	0.40
NIR 0.8	0.63	0.37

For Sun elevation from interval $-1.9° < \alpha < -1.2°$
Correction (α) = Correction (–1.2°) + 0.333 * (Correction(α) – Correction(–1.2°))

For very low elevations of the Sun (from – 1.2° to – 1.9°, i.e. practically below the horizon), less steep curves are used as a substitute for the curves defined for elevations of the Sun greater than –1.2°. These are also hyperbolas calculated from the original hyperbolic curves, such that the difference in correction between the value at a point with elevation $x < -1.2°$ and the value at elevation $x = -1.2°$ is divided by 3. In other words, the correction curve for elevations less than –1.2° will rise towards lower elevations 3x slower.

The last step in preparing the True Colours RGB product is to increase the sensitivity of the VIS 0.5 channel to vegetation. For this purpose, we use the generally known procedure for calculating the normalized vegetation index NDVI, which we convert to a weighting factor F,

by which we add together the albedo of the VIS 0.5 and NIR 0.8 channels. The calculation is as follows:

$$a = vis08 - vis06;\ b = vis08 + vis06;\ NDVI = a / b;$$
$$NDVI' = NDVI^s / (NDVI^s + (1 - NDVI)^s);$$
$$F = (NDVI' - NDVI\_min) / (NDVI' - NDVI\_max) * (F\_min - F\_max) + F\_max;$$

Where we select the parameter values as follows:
s = 4 is the strengthening factor; NDVI_min = 0; NDVI_max = 1; F_min = 0.05; F_max = 0.35;

Of course, the overall result depends on the selection of parameters and we often encounter different values in the works of other authors. It is always on user's decision to add a note that the settings are subjective and this type of product, which is intended for visual use, not for quantitative analysis. However, the main advantage of our method is the greater usability of satellite images near the terminator (Figure 6.4.6). While, for example, the publicly available viewer EUMETView displays data (https://view.eumetsat.int/productviewer?v=default) only for the elevation of the Sun above the horizon, the images prepared according our settings provide useful information about cloud cover much further behind Sun terminator. We can see the difference in the figure area marked with a yellow frame.

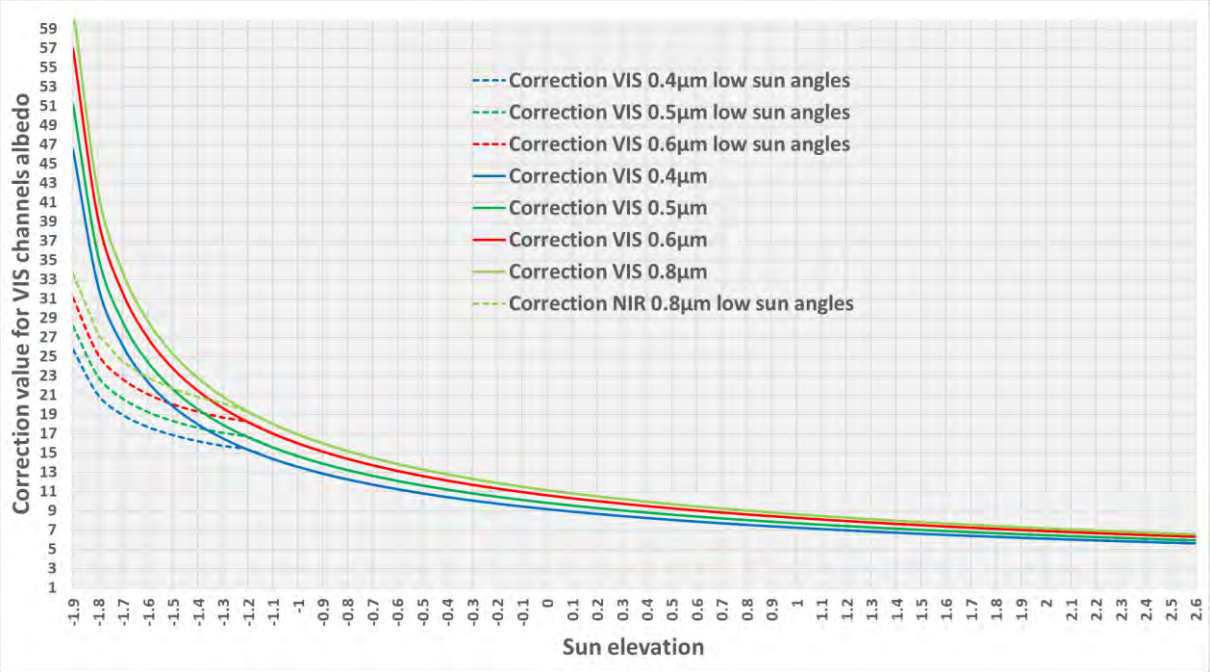

Figure 6.4.5. *Curves for corrections of solar channels on the Sun elevation for MTG FCI spectral channels split to two intervals: for Sun elevations above –1.2° and elevation in interval (–1.9°; –1.2°).*

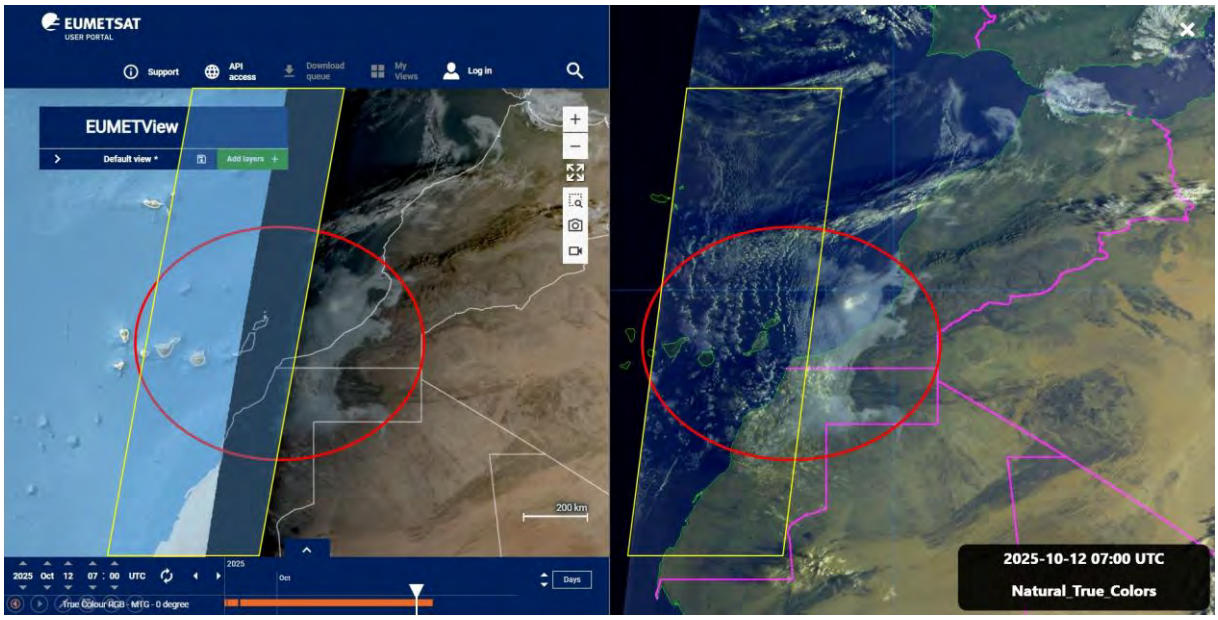

***Figure 6.4.6**. Comparison of True Colors RGB publically available on EUMETSAT web site called EUMETView (left) and similar product prepared at SHMÚ by software MTGProc (right). Enhanced possibilities of cloud monitoring near terminator are highlighted by yellow frame.*

6.5. Soil moisture satellite products for monitoring extreme flooding events

Between 13th and 15th September 2024, Central Europe was affected by a low-pressure system named Boris. This low-pressure system brought record-breaking rainfall and severe flooding in parts of Austria, Czechia, Hungary, Poland and Slovakia.

Storm Boris, originated as an Atlantic frontal system that formed and intensified over the exceptionally warm waters of the Mediterranean. It moved rapidly northeastward, producing very intense precipitation, with rainfall totals of 200 – 300 mm over vast areas and locally exceeding 400 mm.

From Slovak hydrological point of view significant floods occurred throughout Central Europe in the Danube and Morava river basins. In the Czech Republic, Poland and Austria, they were accompanied by high material damage and, unfortunately, loss of human life. In Slovakia, the basins in its western part were mainly affected, namely the Morava river basin and its tributaries, the Danube river basin, Kysuca and part of the Little Carpathian tributaries of the Little Danube.

This study takes a closer look on the development of soil moisture using HSAF H26 product and analyzes how well it performed during these extreme weather conditions in comparison to in situ AWS observations of soil moisture made by Slovak Hydrometeorological Institute (SHMÚ).

For our analysis we used product H26 from H-SAF. H26 product is near-real-time root zone soil moisture profile index with **10 km resolution** in 4 different depth layers (**0 – 7 cm, 7 – 28 cm, 28 –100 cm, 100 – 289 cm**). H26 product is calculated each 24 hours with timeliness of 12 ours.

The H26 product assimilates ASCAT-B/C satellite-derived surface soil moisture into the H-TESSEL land surface model. This assimilation propagates the surface signal through the soil column to derive a four-layer root-zone soil wetness index at 10 km resolution, expressed on a

0–1 scale, which we transformed into percentage. The model accounts for three key factors: soil texture (e.g., clay, sand, and loam), land cover and vegetation, and meteorological conditions (precipitation, temperature, etc.).

We compared the satellite-derived soil moisture data with ground-based observations from automatic weather stations (AWS) in Slovakia. AWS data, originally reported as ***Volumetric Water Content*** (VWC), were converted to the ***Soil Water Index*** (SWI) used by H26. This conversion required knowledge of two soil parameters:

- **Wilting point**: the minimum soil moisture level below which plants cannot extract water from soil
- **Field capacity**: the maximum amount of water soil can hold after excess water has drained

Because exact soil parameter values for each AWS site were unavailable, we used generalized values representative of each station's surrounding area.

H26 product reflected well the high precipitation in central Europe during storm Boris. We can observe the development of SWI on the sequence of images provided here as two examples on Figure 6.5.1 from 7. 9. 2024 and Figure 6.5.2 from 15. 9. 2024. The upper soil level (0 – 7 cm) SWI value started rising on the 13th of September, which was the first day of heavy rainfall from storm Boris in between these two examples).

On the other hand, it can be observed that deeper soil level (28 – 100 cm) has a delay of approximately 3 days, as we see the SWI rising in the west part of Slovakia in the Little Carpathians region on the 16th of September.

When we look at the deepest level (100 – 289 cm), there are barely measurable changes in H26 derived SWI and we cannot compare these to our in-situ measurements, as in situ data are only available up to 50 cm depth.

Looking at full sequence of map visualizations of H26 product over Slovakia and neighbouring countries which we had in disposal, displays the development of soil moisture

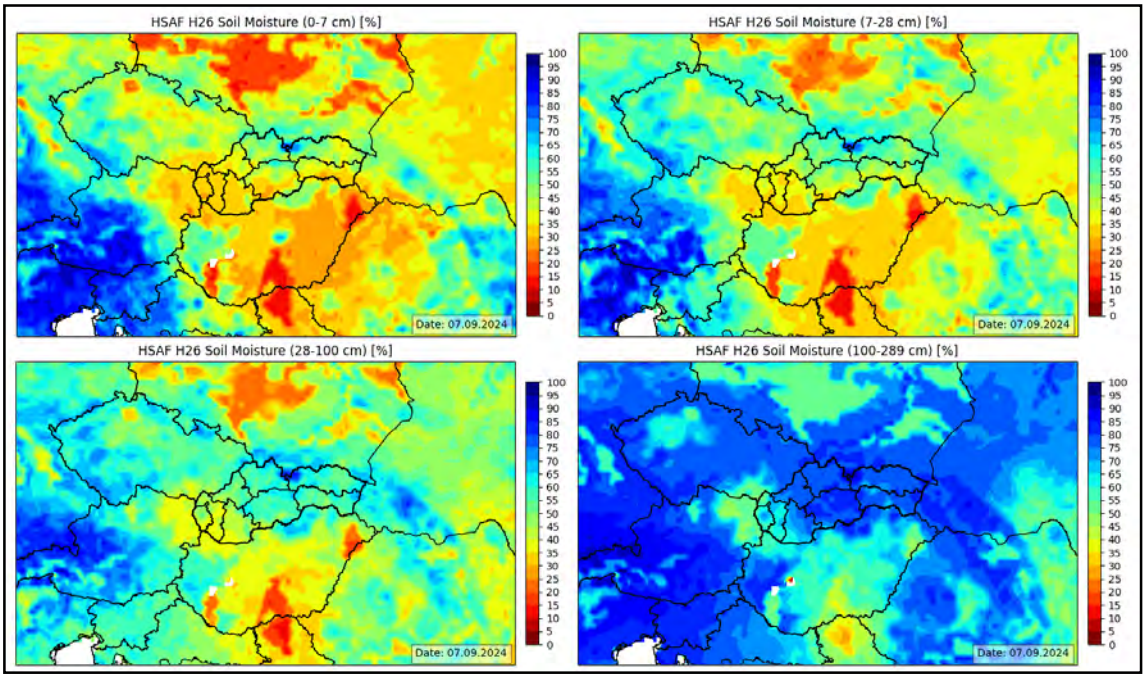

Figure 6.5.1. *Soil moisture product HSAF H26 valid for region of central Europe on 7.9.2024. Relative soil saturation [%] in four different soil layers (0/7/28/100/289cm). At this time mainly upper layers were dry after the period of the hot summer weather.*

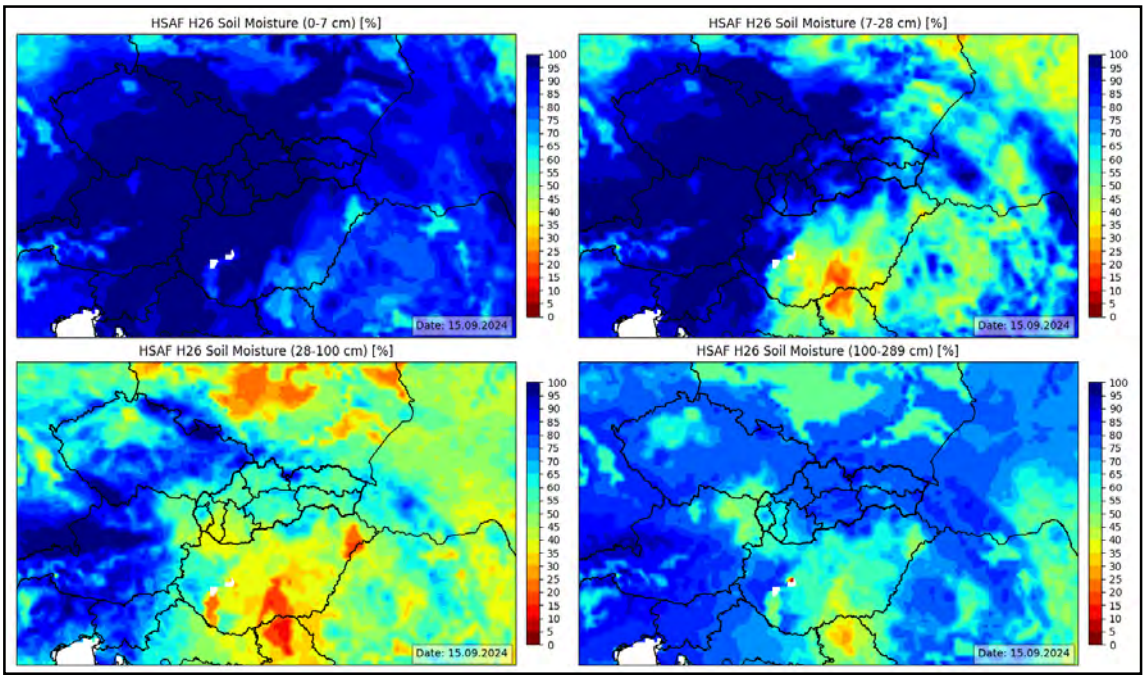

Figure 6.5.2. *Soil moisture product HSAF H26 valid for region of central Europe on 15.9.2024. Relative soil saturation [%] in four different soil layers (0/7/28/100/289cm). After 7 days of intensive rain event related to the The "Boris storm" upper soil layers became very wet, practically reached 100% saturation.*

10th of September 2024 until 21st of September 2024. For each day we had 4 images showing soil moisture from different depth level: Top-left –> 0 – 7 cm; top-right –> 7 – 28 cm; bottom-left –> 28 – 100 cm; bottom-right –> 100 – 289 cm. The color scale is in percentage of SWI and you can see it on the right-hand side.

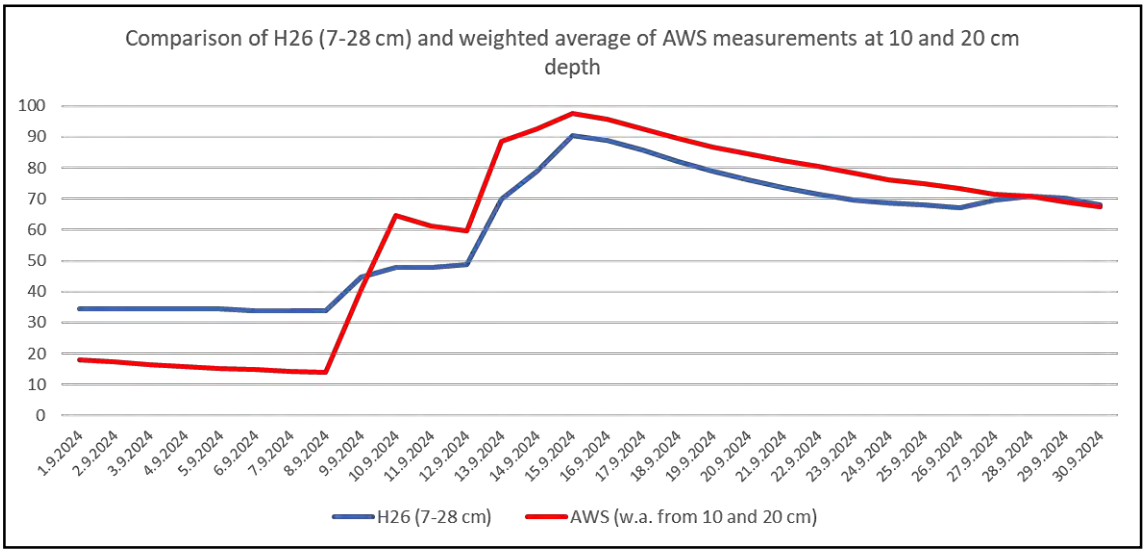

Figure 6.5.3. *Comparison of H26 soil moisture estimates (7 – 28 cm) with the weighted average of in situ measurements obtained from automated weather stations (AWS) at 10 cm and 20 cm depths. The graph illustrates a systematic overestimation of soil moisture by the H26 method during dry conditions, while a slight underestimation is observed during wetter periods.*

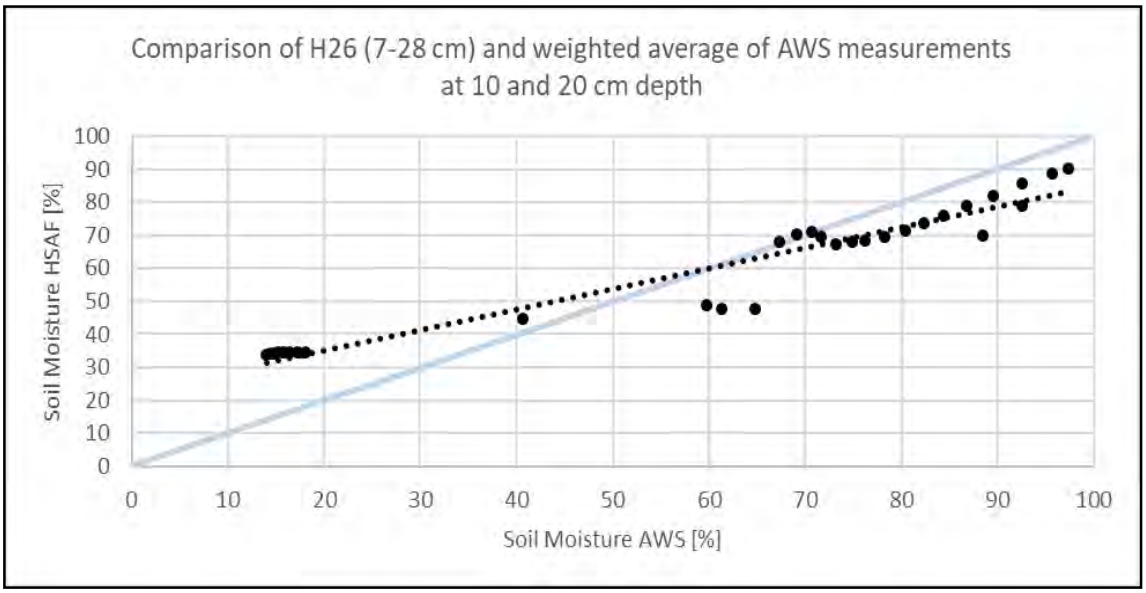

Figure 6.5.4. *Comparison of H26 (7 – 28 cm) and weighted average from in situ measurements from depths 10 and 20 cm. Points from H26 product connected with linear trend line, should be a little bit steeper to fit the in situ measured data.*

Figures from 6.5.3 to 6.5.6 show graphical comparison of SWI derived from satellite measurements and from AWS. Specifically in Figure 6.5.3 and Figure 6.5.4 we used **weighted average** of 10 and 20 cm in-situ measurements by AWS so we could compare these values with H26 (depth 7 – 28 cm). The values of SWI from H26 were overestimated for dry period at the beginning of the month and slightly underestimated during the heavy rainfall period. Pearson correlation coefficient for this comparison method is **0.90.**

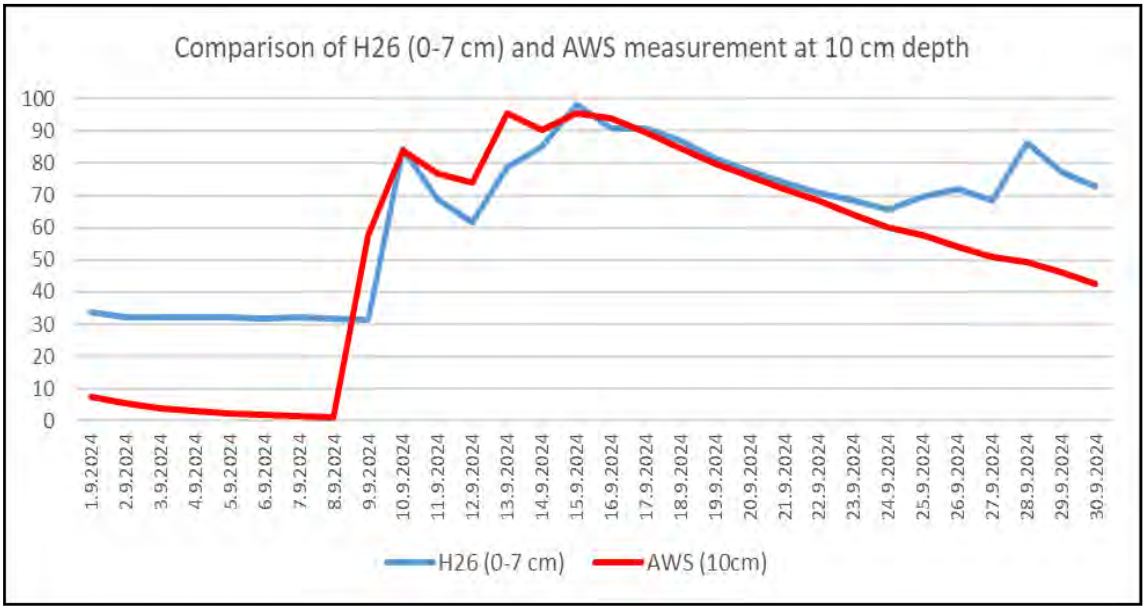

Figure 6.5.5. *Comparison of H26 (0 – 7 cm) with in situ measurement at 10 cm depth. 0 – 7 cm depth H26 product fits better in situ measurements in wet conditions than 7 – 28 cm product, but overestimates soil moisture even more during dry periods.*

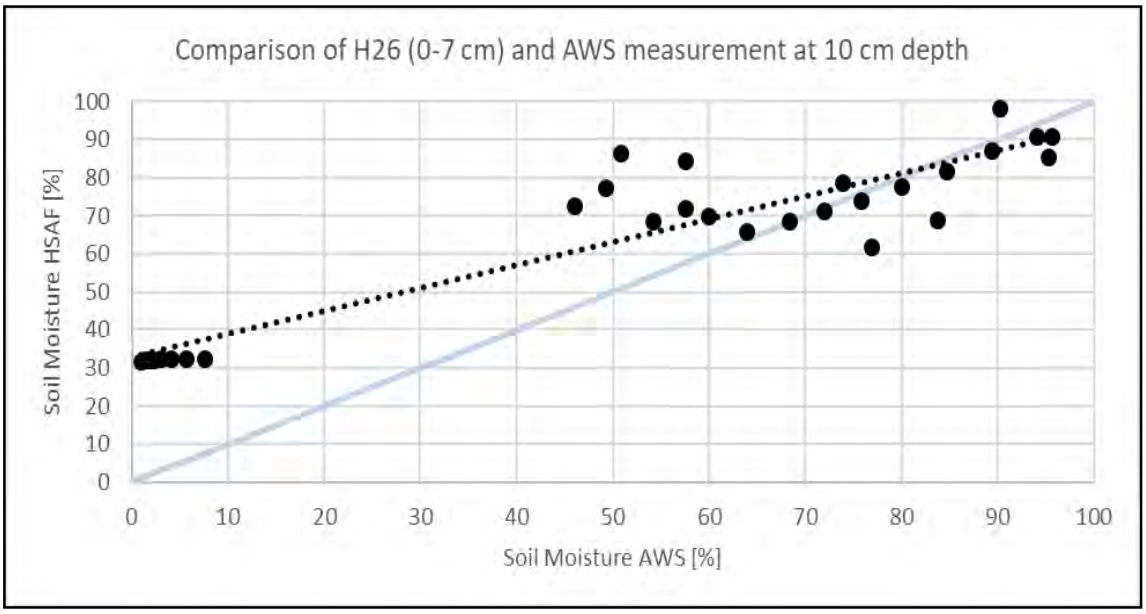

Figure 6.5.6. *Comparison of H26 (0 – 7 cm) with in situ measurement at 10 cm depth. Visualization of better fit of H26 data to in situ measurements during wet periods in this depth, but strong overestimation during dry periods.*

Specifically on Figure 6.5.5 and Figure 6.5.6, where we directly compared H26 (0 – 7 cm) with our 10 cm AWS observations, we observe even bigger overestimation of SWI by H26, however during wet period of the month, with SWI above 60%, H26 fits very well values from AWS, with Pearson correlation coefficient **0.89**.

Finally on Figure 6.5.7 we observe temporal evolution of spatial distribution of soil moisture classes across Slovakia. Value 100% on vertical axis corresponds to the entire territory of Slovakia

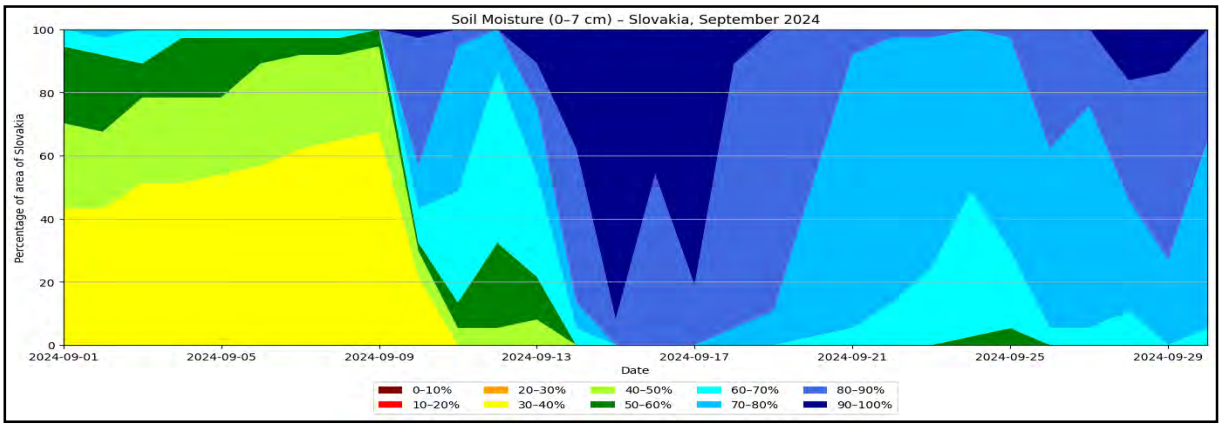

Figure 6.5.7. *Temporal evolution of the spatial distribution of soil moisture classes in the surface layer (0 – 7 cm) across Slovakia*

This study investigates the temporal and spatial variability of soil moisture across Slovakia during September 2024, focusing on the impact of storm Boris, using the newest EUMETSAT H-SAF H26 soil moisture product and in situ measurements from automated weather stations

(AWS). The H26 product assimilates ASCAT-B/C satellite-derived surface soil moisture into the H-TESSEL land surface model.

The analysis captures a sharp transition from dry conditions dominating early September to widespread saturation of soil moisture levels in Slovakia following storm Boris around 9 September.

Comparative analysis with AWS measurements (10 and 20 cm depths) indicates systematic overestimation of soil moisture by H26 during dry conditions and closer agreement during wet periods. The surface layer (0–7 cm) of the H26 product showed the best correlation with in situ data under wet conditions, while still overestimating in dry scenarios.

These findings confirm the utility of the H26 product for high-resolution, near-real-time monitoring of soil moisture (timeliness of 12 hours), and highlight its potential for operational hydrology and landslide potential detection, particularly under wet conditions, while also pointing to the need for adjustments or bias corrections in drier regimes over Central Europe.

References:

[1] BEDKA, K. – BRUNNER, J. – DWORAK, R. – FELTZ, W. – OTKIN, J., GREENWALD, T.: 2010. Objective satellite-based detection of overshooting tops using infrared window channel brightness temperature gradients. J. Appl. Meteorology and Climatology (49, 2), 181 – 202, URL: https://doi.org/10.1175/2009JAMC2286.1.

[2] DOLEŽALOVÁ, A. – SEIDL, J. – ŠŤÁSTKA, J. – KAŇÁK, J.: Automatic detection of overshooting tops and their properties from visible satellite channels. Atmospheric Research, January 2026.
https://doi.org/10.1016/j.atmosres.2025.108488

[3] KAŇÁK, J. – OKON, Ľ.: Nowcasting satellite tools at SHMÚ and their adaptation for MTG data in our operational chain. Integrated Nowcasting Tools Workshop: status, collaboration, use of MTG data. EUMETSAT, Darmstadt, 21.-23.1.2024.

[4] KAŇÁK, J. – OKON, Ľ. – MÉRI, L. – JURAŠEK, M. – PETRACCA, M.: Usage OPERA radar data for validation of H60 and H61 HSAF products. HSAF PT Meeting, 22-23 February 2024, Vienna, Technical University.

[5] KAŇÁK, J. – OKON, Ľ.: Status of development the GEOProc/MTGProc Training Environment at European Weather Cloud - Application demonstration. CWG meeting & MTG 3T WS, 8-12 April 2024, Prague, Czech Republic.
https://cwg.eumetsat.int/2023/09/convection-working-group-and-mtg-3t-forum-meetings-8-12-april-2024-in-prague-czech-republic/

[6] IPWG-11, 15-18 July 2024, Tokyo Institute of Technology: H SAF Precipitation Products Quality Assessment: methodology and results. Oral presentation M. Petracca[1] , J. Kanak[2] , B. Lapeta[3] , A. Toniazzo[4] , N. Roberto[4] and S. Puca[4] 1) Institute of Atmospheric Sciences and Climate, National Research Council (CNR-ISAC), Rome 2) Slovak Hydrometeorological Institute, Bratislava, Slovakia 3) Satellite Remote Sensing Department, Institute of Meteorology and Water Management - National Research Institute, Krakow, Poland 4) Civil Protection Department (DPC), Rome, Italy H SAF Precipitation Products Quality Assessment: methodology and results.
https://www.eorc.jaxa.jp/IPWG/meetings/tokyo2024/pdf/Session04/4.6_HSAFPrecipitationProductsQAMethodologyAndResults_MarcoPetracca%20Marco%20Petracca.pdf

[7] KAŇÁK, J. – OKON, Ľ. – HRUŠKOVÁ, K. – ZVOLENSKÝ, M.: Poster EUMETSAT Conference 2024: Usage of HSAF PCP products in SHMÚ. Session 05. Assessing climate variability and change using satellite observations .Würzburg, Germany, 30 September - 4 October 2024. https://k-program.kuoni-congress.info/pdf/eumetsat-2024/presentation/usage-of-hsaf-products-in-slovak-hydrometeorological-institute

[8] KAŇÁK, J. – OKON, Ľ.: Poster EUMETSAT Conference 2024: Latest experience with the GEOProc/MTGProc environment at EWC, focusing on the quality of RGB products in high resolution. Session 02. Meteosat Third Generation: from products evaluation to operational value. Würzburg, Germany, 30 September - 4 October 2024. https://k-program.kuoni-congress.info/pdf/eumetsat-2024/presentation/latest-experience-with-the-geoprocmtgproc-environment-at-ewc-focusing-on-the-quality-of-rgb-products-in-high-resolution

[9] KAŇÁK, J. – OKON, Ľ.: Poster EUMETSAT Conference 2024: Satellite measurements of insolation and their use in the evaluation of photovoltaic power plant efficiency. Session 05. Assessing climate variability and change using satellite observations. Würzburg, Germany, 30 September - 4 October 2024. https://k-program.kuoni-congress.info/pdf/eumetsat-2024/presentation/satellite-measurements-of-insolation-and-their-use-in-the-evaluation-of-photovoltaic-power-plant-efficiency

[10] KAŇÁK, P. – OKON, Ľ. – JURAŠEK, M. – MÉRI, L. – KAŇÁK, J. – HRUŠKOVÁ, K. – ZVOLENSKÝ, M.: Poster Climate Monitoring Satellite Application Workshop: Evaluating long term surface solar irradiation and precipitation over Slovakia using SAF products. Bonn, Germany, 28 – 30 January 2025. https://www.cmsaf.eu/EN/Outreach/Workshops/past_workshops/CMSAF_User_Workshop_2025/Pdfs_Poster/Poster_Bonn_Peter_Kanak.pdf?__blob=publicationFile&v=2

[11] KAŇÁK, J. – KAŇÁK, P. – OKON, Ľ. – JURAŠEK, M.: Meteosat geostationary satellites – transition from 2nd to 3rd generation and monitoring of selected climatological parameters by satellite measurements. 2nd Poster Day Slovak Meteorological Society. February 13, 2025, Bratislava, Slovakia, FMFI UK.

[12] KAŇÁK, J. – OKON, Ľ. – ZVOLENSKÝ, M. – HRUŠKOVÁ, K.: Case study Boris 12-18/09/2024 by SHMU - precipitation products validation. Contact author: Jan.kanak@shmu.sk. Slovak Hydrometeorological Institute, Jeséniova 17, Bratislava. Quality Assessment, Hydrovalidation and Product Usage workshop Budapest, 2-4 April 2025.

7. INSTITUTIONS INVOLVED IN SPACE RESEARCH

The website of NC is http://nccospar.saske.sk.

Astronomical Institute (AI)
Slovak Academy of Sciences (SAS)
Stará Lesná
059 60 Tatranská Lomnica
contact: J. Rybák (choc@ta3.sk, NC member)

Faculty of Mathematics, Physics and Informatics (FMPI)
Comenius University
Mlynská dolina
842 15 Bratislava
contact: J. Masarik (Jozef.Masarik@fmph.uniba.sk, NC member)

National Forest Centre
T.G. Masaryka 22
960 92 Zvolen
contact: † T. Bucha (died 14 November 2024)

Earth Science Institute (ESI)
Slovak Academy of Sciences (SAS)
Dúbravská cesta 9
841 04 Bratislava
contact: M. Revallo (milos.revallo@savba.sk, Secretary of NC)

Institute of Animal Biochemistry and Genetics CBs
Slovak Academy of Sciences (SAS)
Dúbravská cesta 9
840 05 Bratislava

Biomedical Research Center of the Slovak Academy of Sciences (SAS)
Institute of Experimental Endocrinology (IEE)
Dúbravská cesta 9
845 05 Bratislava

Institute of Experimental Physics (IEP)
Slovak Academy of Sciences (SAS)
Watsonova 47
040 01 Košice
contact: P. Bobík (bobik@saske.sk, NC member)

Institute of Geography (IG)
Slovak Academy of Sciences (SAS)
Štefánikova 49
814 73 Bratislava
contact: J. Feranec (feranec@savba.sk, Vice-Chair of NC)

Institute of Materials and Machine Mechanics
Slovak Academy of Sciences (SAS)
Dúbravská cesta 9/6319
840 05 Bratislava
contact: M. Gebura (ummsgebu@savba.sk, NC member)

Institute of Measurement Science (IMS)
Slovak Academy of Sciences (SAS)
Dúbravská 9
842 19 Bratislava
contact: I. Frollo (frollo@savba.sk)

Institute of Normal and Pathological Physiology (INPP)
Slovak Academy of Sciences (SAS)
Sienkiewiczova 1
813 71 Bratislava

Slovak Central Observatory (SCO)
Komárňanská 137
947 01 Hurbanovo
I. Dorotovič (ivan.dorotovic@suh.sk, Chair of NC, Representative of Slovak NC to COSPAR)

Ministry of Environment of the Slovak Republic
Tajovského 28
975 90 Banská Bystrica
contact: J. Nováček (jozef.novacek@enviro.gov.sk)

Slovak Hydrometeorological Institute
Jeséniova 17
833 15 Bratislava
contact: J. Kaňák (jan.kanak@shmu.sk, NC member)

Michaela Musilová, o. z.
Hroboňova 7
811 04 Bratislava
contact: M. Musilová (michaela@michaelamusilova.com, NC member)

National Agricultural and Food Centre
Soil Science and Conservation Research Institute
Trenčianska 55
821 09 Bratislava
contact: † M. Sviček (died 30 March 2026)

Space Research in Slovakia 2024 – 2025
National Committee of COSPAR in Slovak Republic
Slovak Academy of Sciences

Editors: Ivan Dorotovič and Ján Feranec

Published by the Slovak Central Observatory, Hurbanovo, April 2026
Responsible representative: Marián Vidovenec, Director General

ISBN: 978-80-89998-49-4